UNIVERSITÉ DE LORRAINE | BIBLIOTHÈQUES UNIVERSITAIRES

AVERTISSEMENT

Ce document est le fruit d'un long travail approuvé par le jury de soutenance et mis à disposition de l'ensemble de la communauté universitaire élargie.

Il est soumis à la propriété intellectuelle de l'auteur. Ceci implique une obligation de citation et de référencement lors de l'utilisation de ce document.

D'autre part, toute contrefaçon, plagiat, reproduction illicite encourt une poursuite pénale.

Contact bibliothèque : ddoc-theses-contact@univ-lorraine.fr
(Cette adresse ne permet pas de contacter les auteurs)

LIENS

Code de la Propriété Intellectuelle. articles L 122. 4
Code de la Propriété Intellectuelle. articles L 335.2- L 335.10
http://www.cfcopies.com/V2/leg/leg_droi.php
http://www.culture.gouv.fr/culture/infos-pratiques/droits/protection.htm

UNIVERSITÉ DE LORRAINE

Aalto University
School of Science

École doctorale C2MP

All-optical helicity-dependent switching in magnetoplasmonic structures

THÈSE

présentée et soutenue publiquement le 23 octobre 2025

pour l'obtention du

Doctorat de l'Université de Lorraine

(en Physique)

par

Yann Le Guen

Composition du jury

Président :	Stefania Pizzini	Institut Néel - Grenoble
Rapporteurs :	Liliana Buda-Prejbeanu	Spintec - Grenoble
	Paolo Vavassori	CIC nanoGUNE - San Sebastian
Examinateur :	Bert Koopmans	Eindhoven University of Technology
Invité :	Michel Hehn	Université de Lorraine - Nancy
Directeurs de thèse :	Stéphane Mangin	Université de Lorraine - Nancy
	Sebastiaan van Dijken	Aalto University - Espoo
Encadrant de thèse :	Julius Hohlfeld	Université de Lorraine - Nancy

Institut Jean Lamour - UMR 7019 - Université de Lorraine
Département de Physique de la Matière et des Matériaux
Nanomagnétisme et Electronique de spin

INSTITUT JEAN LAMOUR

Mis en page avec la classe thesul.

Résumé

Alors que la demande en stockage de données haute performance ne cesse d'augmenter, la consommation énergétique qui y est associée devient une préoccupation mondiale. Les dispositifs spintroniques constituent une alternative au system stockage de données traditionnel basé sur la charge des électrons. En stockant les informations de manière non-volatile à travers l'utilisation du moment magnétique des électrons, ces dispositifs réduisent l'énergie nécessaire à la conservation des données. Une nouvelle solution technologique, permettant le contrôle ultra-rapide de l'aimantation par la lumière, a le potentiel d'augmenter davantage la vitesse de stockage et son efficacité énergétique.

Les recherches menées dans ce domaine émergent ont permis la mise au point une méthode de contrôle local de l'aimantation par le biais de multiples impulsions laser femtosecondes polarisés circulairement. Cette méthode est nommée retournement tout optique hélicité dépendant de l'aimantation. Le mécanisme à l'origine de ce phénomène est encore à l'étude. Deux effets ayant des impacts similaires sont considérés : le dichroïsme circulaire magnétique et l'effet Faraday inverse.

À travers leurs capacités à confiner la lumière à des particules de dimensions inférieure à la longueur d'onde, les systèmes plasmoniques peuvent accroître de manière résonante les interactions entre la lumière et la matière. La position spectrale de ces résonances peut être configurée en ajustant la forme et la disposition des particules. L'impact des résonances plasmoniques sur le dichroïsme circulaire magnétique et l'effet Faraday inverse étant différent, elles peuvent être utilisées pour séparer le rôle de ces mécanismes dans le retournement tout optique hélicité dépendant de l'aimantation.

Cette thèse étudie l'origine du retournement tout optique hélicité dépendant de l'aimantation dans les multicouches de Co/Pt à travers la conception, la fabrication et la caractérisation de dispositifs magnéto-plasmoniques. Des réseaux périodiques ainsi que des agencement aléatoires de nanodisques de Co/Pt ont été fabriqués avec succès. Des méthodes de caractérisation adaptées ont été développées ou améliorées pour mener à bien cette étude. Les mesures des spectres optiques et magnéto-optiques présentent les résonances attendues et confirment l'impact ces résonances sur le dichroïsme circulaire magnétique et l'effet Faraday inverse. Les expériences de retournement tout optique hélicité dépendant de l'aimantation en fonction de la longueur d'onde ont montré une inversion du comportement du retournement de l'aimantation à une longueur d'onde spécifique pour les systèmes de disques agencés aléatoirement. Ce changement de signe est caractéristique du dichroïsme circulaire magnétique, soulignant son rôle dans le retournement tout optique hélicité dépendant de l'aimantation. Cependant, un décalage en longueur d'onde du passage à zéro entre les spectres du retournement de l'aimantation et du dichroïsme circulaire suggère la contribution d'un effet supplémentaire.

Mots-clés: Magnétisme, Ferromagnétique, Magnéto-optique, Plasmonique, Nanoparticule, Magnéto-plasmonique, Spintronique ultrarapide, Retournement tout optique hélicité dépendant de l'aimantation

Abstract

As the demand for high-speed storage keeps increasing, its associated energy consumption becomes a global concern. An alternative to traditional charge-based high-speed storage comes in the form of spintronic devices. By storing the information in a non-volatile manner using magnetisation, these devices cut down on the energy needed to maintain data. A new technological solution in the form of ultra-fast light-induced magnetisation control has the potential to further increase storage speed and energy efficiency.

The research in this emerging field has presented a method for local control of magnetisation using multiple circular polarised femtosecond laser pulses, known as all-optical helicity-dependent switching. The mechanism behind this phenomenon is still under investigation. Two effects with similar observable impacts are considered: the magnetic circular dichroism and the inverse Faraday effect.

Through their ability to confine light to sub-wavelength-scale particles, plasmonic systems can resonantly enhance light-matter interactions. The position of these resonances can be tuned by modifying the particle's shape and configuration. The impact of plasmonic resonances on the magnetic circular dichroism and the inverse Faraday effect being different, they can be used to disentangle the role of these mechanisms in all optical helicity-dependent switching.

This thesis investigates the origin of all-optical helicity-dependent switching in Co/Pt multilayers through the design, fabrication and characterisation of magneto-plasmonic devices. Periodic arrays and randomly distributed configurations of Co/Pt nano-disks were successfully fabricated. Specific characterisation methods were developed or improved to carry out this study. The measurements of the optical and magneto-optical spectra showed the expected features and confirmed the impact of resonances on the magnetic circular dichroism and the inverse Faraday effect. Wavelength-dependent switching experiments showed an inversion of the switching behaviour at a specific wavelength for randomly distributed disk systems. This change of sign is characteristic of the magnetic circular dichroism spectrum, highlighting its role in all-optical helicity-dependent switching. However, a shift in the zero crossing between the switching and circular dichroism spectra suggests a contribution of an additional effect.

Keywords: Magnetism, Ferromagnet, Magneto-optics, Plasmonics, Nanoparticles, Magneto-plasmonic, Ultra-fast spintronics, All-optical helicity-dependent switching

Remerciements

This thesis concludes a four-year journey during which I was fortunate to work on interesting challenges and meet incredible people. I had the opportunity to carry out my PhD as a double degree between Aalto University in Finland and Université de Lorraine in France. This came with its fair share of complications but also meant being in contact with individuals with diverse personalities, experiences and knowledge.

As I started my first year of work as part of the NanoSpin team in Aalto, I quickly managed to find my place thanks to the help and company of my fellow students and colleagues. In particular, I would like to thank Nikolai Kuznetsov, Sreeveni Das, Abhishek Talapatra, Weijia Zhu and Maria Ameziane for their warm welcome. We were later joined by Anton Lutsenko, Lars Peeters and Junyoung Hyun. I was able to explore the fascinating domain of nanomagnetism and plasmonics and tackle my first research project, benefiting from the guidance and expertise of Rhodri Mansell, Lukas Flajsman and Huajun Qin. Each and every one contributed to make this place enjoyable to work at and to foster an atmosphere of curiosity and exchange.

As my first year reached an end, I moved back to France and continued my PhD in the SpinNano team at Institut Jean Lamour. There, I encountered some familiar faces, as well as some new ones. In particular, Maxime Vergès, with whom I previously worked during my Master's internship. These years would not have been the same without this amazing team composed of experts in a wide range of topics, ready to discuss and help out whenever they could. For this reason, I wish to thank Michel Hehn, Daniel Lacour, Sébastien Petit-Watelot, Gregory Malinowski and Jon Gorchon. During these years, I had the freedom to develop and improve a laser setup, exploring an aspect of science that I enjoy a lot. This led to collaboration with many colleagues on exciting projects. In the context of these collaborations, I want to acknowledge the incredible work of Junta Igarashi, Kazuaki Ishibashi, Alberto Anadón, Jun-Xiao Lin, Quentin Remy and Wei Zhang.

Of course, I would like to give a special shout-out to my office mates Héloïse Damas, Yi Peng, and Wei Yang. As time passed, I had the pleasure of sharing an office with Harjinder Singh, Hyacinthe Cabrel Tadaha, and Adrian Benedit-Cardenas. I wish to express my appreciation to the MiNaLor competence centre team, in particular Demba Ba and Laurent Badie, who trained me and helped me solve issues related to the nanofabrication of my samples. Breaks were the opportunity to gather and enjoy a nice and relaxing time, spending moments with colleagues I didn't actively work with. In honour of the lunch and coffee breaks, I would like to do some extra shout-outs to Valentin Desbuis, Jude Compton-Stewart, Sandrine Lopes, Anna-Maria Friedel, Victor Huet and Pierre Chailloleau.

Naturally, I would like to thank my friends and family who believed in me and supported me through all these years. In particular, William and Guillaume, who, despite being sometimes thousands of kilometres away, were there to help me relax and unwind after work. But also Pierre, whom I have known for most of my life, I will always be there for you as you were there for me.

During my PhD, I had the wonderful surprise of meeting Eva. You've become an important, if not the most important, person in my life, and I believe it is just the beginning of a long journey together. Your love and support pulled me through these difficult times. I wouldn't have made it without you.

I spent most of my measuring time in the company of Julius Hohlfeld. I am very grateful for your advice and help. While working with you, I learnt a lot and I hope we will have the opportunity to work together again in the future.

I was lucky to have not one but two great supervisors, Sebastiaan van Dijken and Stéphane Mangin, who, through their knowledge and wisdom, directed me towards a successful PhD. I can not thank them enough for this chance.

To my late cat Salem,
who was with me
for most of my life.

Contents

Introduction **1**

Chapter 1 All-optical switching of magnetisation **7**

1.1 Magnetic systems . . . 8

1.1.1 Magnetic moment . . . 8

1.1.2 Magnetic interactions . . . 9

1.1.3 Micromagnetic equation . . . 9

1.1.4 Magnetic anisotropy . . . 10

1.1.5 Magnetic domains . . . 11

1.1.6 Field control of magnetisation . . . 12

1.2 Magnetic materials . . . 13

1.2.1 Ferromagnetic materials . . . 13

1.2.2 Ferrimagnetic materials . . . 14

1.3 Ultrafast spin dynamics . . . 15

1.3.1 Ultrafast demagnetisation . . . 15

1.3.2 All-optical helicity-independent switching . . . 16

1.3.3 All-optical helicity-dependent switching . . . 18

Chapter 2 Plasmonics and magneto-plasmonics **25**

2.1 Plasmonics . . . 26

2.1.1 Electromagnetic waves in solids . . . 26

2.1.2 Plasmons . . . 27

2.1.3 Localised surface plasmon resonance . . . 29

2.1.4 Surface lattice resonance . . . 31

2.2 Magneto-optics . . . 32

2.2.1 Magneto-optical effects in thin films . . . 32

2.2.2 Magneto-optical effects in plasmonic systems . . . 36

2.2.3 Magnetisation control with plasmonics . . . 38

Chapter 3 Methodology **41**
3.1 Sample fabrication . . . 42
3.2 Sample characterisation . . . 44
3.2.1 Magneto-optical Kerr effect magnetometer . . . 44
3.2.2 Optical spectrometer . . . 46
3.2.3 Magneto-optical spectrometer . . . 47
3.2.4 Magnetic circular dichroism spectrometer . . . 48
3.3 Simulations . . . 49
3.3.1 Transfer Matrix method . . . 49
3.3.2 Comsol simulations . . . 49
3.4 All optical switching experiments . . . 51
3.4.1 Femtosecond laser setup . . . 51
3.4.2 State diagram . . . 52

Chapter 4 AO-HDS in Co/Pt multilayer thin films **55**
4.1 Magnetic properties of Co/Pt multilayer thin films . . . 56
4.2 Magneto-optical characterisation . . . 57
4.3 Simulation and Voigt parameter fitting . . . 61
4.4 All-optical helicity-dependent switching . . . 63
4.4.1 State Diagrams . . . 63
4.4.2 Spectral behaviour . . . 66

Chapter 5 AO-HDS in Co/Pt nanodisks **69**
5.1 Motivation . . . 70
5.2 Sample preparation . . . 70
5.3 Optical and magneto-optical characterisation . . . 71
5.4 All-optical switching experiments . . . 74
5.4.1 Measurements . . . 74
5.4.2 Post-processing . . . 75
5.5 Results . . . 76
5.5.1 All-optical helicity-dependent switching spectra . . . 76
5.5.2 Pulse duration dependence . . . 78
5.5.3 Power dependence . . . 79
5.6 Discussion . . . 81

Chapter 6 Arbitrarily shaped laser spot characterisation technique **83**
6.1 Theoretical principles . . . 84
6.2 Practical implementation . . . 84

6.3 Examples 86
6.3.1 Gaussian beam 86
6.3.2 Laguerre-Gauss beam 88
6.3.3 Bessel-Gauss beam 90
6.4 Discussion 91

Conclusion **93**

Annexe A AFM measurements **97**

Annexe B Magneto-optical calculations **101**

Annexe C Transfer matrix method implementation **107**

Annexe D Magnetic force microscopy measurements **113**

Résumé de la thèse **117**

List of Figures

1.1 Illustration of the different geometries of domain walls. 11
1.2 Example of a hysteresis loop M(H). 13
1.3 Example of the temperature dependence of magnetisation in a ferromagnet and ferrimagnet. 14
1.4 Normalised TR-MOKE measurements of the demagnetisation of Ni. 15
1.5 Electronic and spin temperature dynamics measurement and calculation from the 3TM. 16
1.6 Normalised Fe and Gd elements specific time-resolved XMCD measurements. . . 17
1.7 All-optical helicity-independent switching behaviour of a $Gd_{24}(FeCo)_{76}$ thin film. 18
1.8 All-optical helicity-dependent switching experiment in a $Gd_{22}Fe_{74.6}Co_{3.4}$ thin film 19
1.9 State diagram of AO-HDS in Co/Pt multilayers. 19
1.10 Normalised time resolved Hall resistance measurements of all-optical helicity-dependent switching of Co/Pt Hall crosses. 20

2.1 Dispersion relation of light in metal and of SPPs at at the interface between a metal and a dielectric material. 28
2.2 Comparison between a calculated LSPR and SLR. 30
2.3 Extinction spectra, cross section and shape factor of an periodic square array. . . 32
2.4 Illustration of the different MOKE configurations. 33
2.5 Illustration of Kerr and Faraday rotation and ellipticity. 35
2.6 Illustration of the rotation and ellipticity at resonances. 36
2.7 P-MOKE rotation and ellipticity spectra for randomly distributed Ni nano-disks. 37
2.8 Comparison of AO-HIS in Co/Gd/Pt multilayer film and nanodisk array. 39
2.9 Monte Carlo simulation results of AO-HDS in a Co/Pt film coupled with a plasmonic systems. 40

3.1 Schematic of the nanofabrication process. 43
3.2 Schematic of the MOKE magnetometer setup. 45
3.3 Schematic of the optical spectrometer. 46
3.4 Schematic of the magneto-optical spectrometer. 47
3.5 Schematic of the MCD spectrometer. 48
3.6 Illustration of the COMSOL geometry used to simulate the different spectra. . . 50
3.7 Schematic of the femtosecond laser setup. 51

4.1 Illustration and hysteresis loop of the studied Co/Pt multilayers thin films. . . . 56
4.2 Measured optical and magneto-optical spectra for Co/Pt multilayer thin films. . . 58
4.3 MCD spectra from sample 951_3 (2 Co/Pt repetitions) using different formulas for the calculation of MCD. 59

4.4 MCD spectra for Co/Pt multilayer thin films. 60
4.5 Spectra of optical indices n and κ for Co/Pt multilayers. 61
4.6 Voigt parameter spectra for Co/Pt multilayers. 62
4.7 AO-HDS state diagrams of Co/Pt multilayers films. 63
4.8 Normalised MOKE images depicting AO-HDS in sample 951_1. 64
4.9 Normalised MOKE images depicting AO-HDS in sample 951_3. 65
4.10 Normalised AO-HDS switching and multidomain fluence threshold spectra of sample 951_1. 66

5.1 Illustration and hysteresis loop of the studied Co/Pt nanodisk structures. 70
5.2 Comparison of the simulated $i(E \times E^*).e_z$, absorption and Faraday rotation spectra. 71
5.3 Measured and simulated optical and magneto-optical spectra for 10 Co/Pt repetitions nanodisk arrays. 72
5.4 Measured and simulated optical and magneto-optical spectra for a 10 Co/Pt repetitions nanodisk aperiodic array. 73
5.5 Illustration of the post processing of the AO-HDS experiment MOKE images. . . 75
5.6 Illustration of the grouping of data based on the symmetry of initial magnetisation state and light polarisation combinations. 76
5.7 AO-HDS spectra for sample 1026_2 ($[Co/Pt]_{10}$). 77
5.8 Compilation of results for sample 1236 ($[Co/Pt]_{10}$) with randomly distributed nanodisks. 78
5.9 Dependence of partial AO-HDS on laser pulse duration. 79
5.10 Laser fluence dependant switching measurements. 80

6.1 Sketch of the laser spots characterisation setup. 85
6.2 Beam reconstruction results for Gaussian beam. 87
6.3 $1/E_p(r_{eq})$ fit for the Gaussian beam. 88
6.4 Vortex wave plate alignment mismatch. 88
6.5 Results for the Laguerre-Gauss beam. 89
6.6 $1/E_p(r_{eq})$ fit for the Laguerre-Gauss beam. 90
6.7 Results for the Bessel-Gauss beam. 91

A.1 AFM image of periodic and randomly distributed nano-disks structures. 99

C.1 Reproduction of Atkinson results in Co/Pt multilayers using the 4x4 TMM. . . . 111

D.1 MFM images of Co/Pt nano-disk array. 114
D.2 MFM images of the final magnetic state of Co/Pt nano-disk array after being exposed to different laser polarisation. 115

Introduction

English version

Data storage and processing have become an international issue as the demand for high-speed storage has grown exponentially in the past decades, in particular with the recent rapid development of artificial intelligence. All this data storage and processing comes with a very high energy cost as the energy consumption of data centres in the U.S. is projected to reach up to 12 % of the U.S. electricity production by 2028 [1]. The environmental impact cannot be neglected with information communication technologies representing nearly 3 % of the total greenhouse gas emission in 2018 and projected to reach up to 14 % in 2040, with nearly half of the emission associated with data centres [2].

Spintronic devices, which utilise the spin of electrons instead of their charge to store and move information, offer appealing strengths to address part of this issue. By relying on magnetisation to store information in a non-volatile manner, it does not require any energy to refresh and keep the stored data, as is the case for CMOS-based RAM. This approach is not new, as magnetic storage media have been developed since the early 20th century and are still commonly used to this date in hard disk drives. Hard drives are still being developed with the recent integration of heat-assisted magnetic recording [3], allowing the manufacturing of cheap, high-density bulk storage solutions. The main issue with these previous devices is the writing and reading speed, which is incompatible with their integration with increasingly faster data processing. The discovery of giant magneto-resistance in 1988 [4], followed by tunnel magneto-resistance, has led to the development of magneto-resistive RAM or MRAM, which tightly integrates magnetic storage with traditional charge-based computing. Nevertheless, due to the resistive nature of the underlying mechanism, the read and write operations still require a significant amount of energy and write operations are limited, in practical applications, to speeds of around tens of nanoseconds [5]. Much research is done to alleviate these issues, in particular with the development of spin orbit torque MRAM or SOT-MRAM reaching higher speeds and record low writing energy consumption [6].

The observation of ultra-fast demagnetisation of Ni by Beaurepaire et al. in 1996 [7] marked the beginning of the field of ultra-fast magnetisation control. The use of femtosecond laser pulses to locally manipulate magnetisation was further studied and led to the observation of two phenomena: all-optical helicity-independent switching [8] and all-optical helicity-dependent switching [9] of magnetisation. The first effect is now understood to be thermal in origin, while the second, which seems to come from a more complex interaction between light and magnetisation, is still not fully understood. Two mechanisms have been put forward to explain this switching effect: magnetic circular dichroism and the inverse Faraday effect. Both effects have similar observable impacts and, consequently, the separation of their contribution to the magnetic switching is complicated. In combination with magneto-optical effects for magnetisation reading, these switching methods have the potential to initiate the development of ultra-fast all-optical storage devices.

Plasmonics, which investigates the coupling of electron oscillations at metal surfaces to electromagnetic fields, has been actively studied in the past century for the ability to confine light at sub-wavelength scales and to enhance light-matter interactions. Plasmonic systems consisting of metallic nanoparticles can be tuned through their size, shape and distribution to exhibit resonances at specific wavelengths. These compelling properties have led to the integration of plasmonic devices in sensing, light absorption and emission enhancement applications [10].

The combination of all-optical switching and plasmonic systems offers a promising path for their integration into novel storage devices. The use of magneto-plasmonic systems to enhance the efficiency of all-optical helicity-independent switching has been shown [11] [12]. In contrast, all-optical helicity-dependent switching in magneto-plasmonic systems has barely been studied. A better understanding of helicity-dependent switching is needed to allow the design and optimisation of switchable and energy-efficient magneto-plasmonic structures. The impact of plasmonics on the magneto-optical responses has previously been demonstrated and can yield considerable readout sensitivity enhancement [11] [13] [14].

The work presented in this thesis aims to study all-optical helicity-dependent switching in magneto-plasmonic systems. Using the difference in behaviour at the plasmonic resonance between magnetic circular dichroism and the inverse Faraday effect, these two effects can be separated. All-optical helicity-dependent switching experiments in these plasmonic systems will thus highlight the contribution of both effects to switching. This thesis is organised as follows:

- Chapter 1 is split into three parts, the first of which provides the fundamentals of magnetism needed to understand this work. In the second part, the magnetic materials studied in this project are described. Finally, a state-of-the-art overview of various types of all-optical switching is presented.
- Chapter 2 covers the basics of plasmonics, followed by the description of magneto-optical effects in films. The chapter is concluded by a state-of-the-art on the impact of plasmonic systems on the magneto-optical response and the use of plasmonics in all-optical switching.
- Chapter 3 details the different fabrication and characterisation techniques used in this work. It also outlines the simulation methods applied during this project.
- Chapter 4 reports on magneto-optical measurements and all-optical helicity-dependent switching experiments in Co/Pt multilayer thin films.
- Chapter 5 reports on the measurements of optical and magneto-optical spectra in periodic and aperiodic arrays of Co/Pt nano-disk. In particular, the difference in behaviour at the plasmonic resonance between magnetic circular dichroism and the inverse Faraday effect is demonstrated. In wavelength-dependent all-optical helicity-dependent switching experiments, a correlation between the switching efficiency and magnetic circular dichroism is established, highlighting its role in all-optical magnetic switching.
- Chapter 6 presents a newly developed beam shape characterisation technique that is used to precisely describe the all-optical switching behaviour in magnetic films.

Version française

Le stockage et le traitement de données sont devenus un enjeu international. La demande en stockage haute performance a connu une croissance exponentielle au cours des dernières décennies, en particulier avec le récent et rapide développement de l'intelligence artificielle. Tout ce stockage et traitement de données s'accompagnent d'un coût énergétique très élevé. La consommation d'énergie des centres de données aux États-Unis devrait atteindre jusqu'à 12 % de la production d'électricité américaine d'ici 2028 [1]. L'impact environnemental ne peut aussi pas être négligé. Les technologies liées à information et de la communication représentent près de 3 % des émissions totales de gaz à effet de serre en 2018 et devrait atteindre jusqu'à 14 % en 2040. Près de la moitié de ces émissions étant associées aux centres de données[2].

Les dispositifs spintroniques, qui utilisent le spin des électrons plutôt que leur charge pour stocker et transférer des informations, offrent des avantages intéressants pour résoudre en partie ce problème. En s'appuyant sur l'aimantation pour stocker des informations de manière non-volatile, ils ne nécessitent aucune énergie pour rafraîchir et conserver les données stockées, contrairement aux mémoires RAM basées sur la technologie CMOS. Cette approche n'est pas nouvelle, les supports de stockage magnétiques ont été développés dès le début du XXe siècle et sont encore couramment utilisés à ce jour sous la forme de disque dur. Les disques durs continuent d'être développés avec l'intégration récente de l'enregistrement magnétique assisté par chaleur [3], qui permet la fabrication de solutions de stockage de masse bon marché et de haute densité. Le principal problème de ces anciens dispositifs est leur vitesse d'écriture et de lecture, qui est incompatible avec leur intégration avec des systèmes de traitement de données de plus en plus rapide. La découverte de la magnétorésistance géante en 1988 [4], suivie de la magnétorésistance à effet tunnel, a conduit au développement de la mémoire RAM magnétorésistive ou MRAM, qui intègre étroitement le stockage magnétique au système informatique traditionnel basé sur la charge d'électrons. Néanmoins, en raison de la nature résistive du mécanisme sous-jacent, les opérations de lecture et d'écriture nécessitent encore une quantité d'énergie non-négligeable et les opérations d'écriture sont limitées, en pratique, à des vitesses de l'ordre de quelques dizaines de nanosecondes [5]. De nombreuses recherches sont menées pour remédier à ces problèmes, notamment avec le développement de la mémoire MRAM à couplage spin-orbite ou SOT-MRAM, qui atteint des vitesses plus élevées et une efficacité énergétique d'écriture record [6].

L'observation de la démagnétisation ultra-rapide du nickel induite par impulsion laser par Beaurepaire et al. en 1996 [7] a marqué le début du domaine de recherche consacré au contrôle ultra-rapide de l'aimantation. L'utilisation d'impulsions laser femtosecondes pour localement manipuler l'aimantation a fait l'objet d'études plus approfondies et a conduit à l'observation de deux phénomènes : le retournement tout optique hélicité indépendant de l'aimantation [8] et le retournement tout optique hélicité dépendant de l'aimantation [9]. Le premier effet est désormais considéré comme étant d'origine thermique, tandis que le second, qui semble provenir d'une interaction plus complexe entre la lumière et l'aimantation, n'est pas encore entièrement compris. Deux mécanismes ont été mis en avant pour expliquer cet effet de retournement : le dichroïsme circulaire magnétique et l'effet Faraday inverse. Ces deux effets ont des impacts mesurables similaires et, par conséquent, il est difficile de distinguer leur contribution respective au retournement de l'aimantation. Combinées aux effets magnéto-optiques pour la lecture de l'état magnétique, ces méthodes de contrôle de l'aimantation pourraient permettre le développement de dispositifs de stockage de données entièrement optiques ultra-rapides.

La plasmonique, qui étudie le couplage des oscillations électroniques à la surface des métaux avec les champs électromagnétiques, a fait l'objet de recherches intensives au cours du siècle dernier en raison de la capacité des système plasmonique à confiner la lumière à des échelles

inférieures à la longueur d'onde et à améliorer les interactions entre la lumière et la matière. Les systèmes plasmoniques, constitués de nanoparticules métalliques, peuvent être ajustés en modifiant leur taille, leur forme et leur agencement afin de présenter des résonances à des longueurs d'onde spécifiques. Ces propriétés intéressantes ont conduit à l'intégration de dispositifs plasmoniques dans des applications de détection et d'amplification de l'absorption et de l'émission de la lumière [10].

L'intégration du retournement tout optique de l'aimantation dans des systèmes plasmoniques ouvre une voie prometteuse pour leur intégration dans de nouveaux dispositifs de stockage de données. L'utilisation de systèmes magnéto-plasmoniques pour améliorer l'efficacité du retournement tout optique hélicité indépendant de l'aimantation a été démontrée [11] [12]. En revanche, le retournement tout optique hélicité dépendant de l'aimantation dans les systèmes magnéto-plasmoniques a été très peu étudiée. Une meilleure compréhension du retournement tout optique hélicité dépendant de l'aimantation est nécessaire pour permettre la conception et l'optimisation de structures magnéto-plasmoniques fonctionnel et pour améliorer leur consommation énergétique. L'impact des effet plasmonique sur les réponses magnéto-optiques a déjà été démontré et permet une amplification considérable de la sensibilité de lecture de l'état magnétique [11] [13] [14].

Le travail présenté dans cette thèse vise à étudier le retournement tout optique hélicité dépendant de l'aimantation dans les systèmes magnéto-plasmoniques. En utilisant la différence de comportement spectral à la résonance plasmonique entre le dichroïsme circulaire magnétique et l'effet Faraday inverse, ces deux effets peuvent être séparés. Les expériences de retournement tout optique hélicité dépendant de l'aimantation dans ces systèmes plasmoniques mettront ainsi en évidence la contribution des deux effets au phénomène de retournement. Cette thèse est organisée comme suit :

- Le Chapitre 1 est divisé en trois parties, la première partie présentant les principes fondamentaux du magnétisme nécessaires à la compréhension de ce travail. La deuxième partie décrit les matériaux magnétiques étudiés dans le cadre de ce projet. Enfin, un état de l'art des différents types de retournement tout optique de l'aimantation est présenté.

- Le Chapitre 2 couvre les bases de la plasmonique, suivies d'une description des effets magnéto-optiques dans les films. Le chapitre se termine par un état de l'art sur l'impact des systèmes plasmoniques sur la réponse magnéto-optique et l'utilisation de système plasmonique pour le retournement tout optique de l'aimantation.

- Le Chapitre 3 détaille les différentes techniques de fabrication et de caractérisation utilisées durant cette thèse. Il décrit également les méthodes de simulation employées au cours de ce projet.

- Le Chapitre 4 détaille les résultats des mesures magnéto-optiques et des expériences de retournement tout optique de l'aimantation dans des multicouches de Co/Pt.

- Le Chapitre 5 communique les résultats des mesures des spectres optiques et magnéto-optiques de réseaux périodiques et apériodiques de nanodisques de Co/Pt. En particulier, la différence de comportement spectral à la résonance plasmonique entre le dichroïsme circulaire magnétique et l'effet Faraday inverse est démontrée. Les expériences de retournement tout optique hélicité dépendant de l'aimantation en fonction de la longueur d'onde, montre une corrélation entre l'efficacité de retournement de l'aimantation et le spectre du dichroïsme circulaire magnétique, soulignant son rôle dans le retournement tout optique hélicité dépendant de l'aimantation.

- Le Chapitre 6 présente une nouvelle technique de caractérisation de la forme de faisceaux laser. Cette technique est employée pour décrire avec précision le comportement retournement tout optique de l'aimantation dans les films magnétiques.

Chapter 1

All-optical switching of magnetisation

In this chapter, the different concepts linked to magnetisation and its control by light are introduced. The main characteristics of a magnetic system are described and the magnetic materials studied are presented. The second part of this chapter focuses on the state-of-the-art of all-optical switching of magnetisation.

1.1 Magnetic systems

1.1.1 Magnetic moment

Some atoms carry a magnetic moment which is at the origin of magnetism. The magnetic moment $\mathbf{m}$ comes from the orbital angular momentum $\mathbf{L}$ and the spin angular momentum $\mathbf{S}$ of charged particles. The first contribution is linked to the amount of rotation of electric charge around a certain axis and the second is linked to the intrinsic spin of the charged particle. In atoms, both protons and electrons carry a magnetic moment but the contribution of the nuclear moment can be neglected [15]. Therefore, only electrons are considered for the magnetisation of solids.

For an electron, the magnetic moment induced by its orbital angular momentum $\mathbf{l}$ is:

$$\mathbf{m} = -\frac{e}{2m_e}\mathbf{l} = \gamma\mathbf{l} \tag{1.1}$$

With e the charge of the electron, m_e the mass of the electron and γ the gyromagnetic ratio defined as the ratio between the magnetic moment and the angular momentum. For a given azimuthal quantum number l, this contribution to the magnetisation is quantised through the orbital magnetic quantum number $m_l \in [-l, l] \cap \mathbb{Z}$ in such a way that in a given (z) direction:

$$m_z = -\mu_B m_l \tag{1.2}$$

With μ_B the Bohr magneton defined as:

$$\mu_B = \frac{e\hbar}{2m_e} = 9.274 \cdot 10^{-24}\mathrm{JT}^{-1} \tag{1.3}$$

Similarly, the magnetic moment induced by the spin angular momentum $\mathbf{s}$ of an electron is :

$$\mathbf{m} = -\frac{e}{m_e}\mathbf{s} = 2\gamma\mathbf{s} \tag{1.4}$$

This contribution is also quantised through the spin magnetic quantum number $m_s = \pm\frac{1}{2}$ such that:

$$m_z = -2\mu_B m_s \tag{1.5}$$

The total magnetic moment of an electron is therefore the vector sum of both contributions:

$$\mathbf{m} = -\frac{\mu_B}{\hbar}(\mathbf{l} + 2\mathbf{s}) \tag{1.6}$$

In atoms, the contribution of all electrons is added up $\mathbf{L} = \sum_i \mathbf{l}_i$ and $\mathbf{S} = \sum_s \mathbf{s}_i$. The electrons of atoms are organised in shells and the filling of these shells to constitute the ground state is dictated by Hund rules [16]:

1. $|\mathbf{S}|$ is maximised while respecting the exclusion principle.
2. $|\mathbf{L}|$ is maximised while respecting the configuration dictated by the first criteria.
3. The total angular momentum $\mathbf{J} = \mathbf{L} + \mathbf{S}$ amplitude is equal to $|\mathbf{L}| - |\mathbf{S}|$ if the shell is less than half full, equal to $|\mathbf{L}| + |\mathbf{S}|$ if the shell is more than half full and equal to $|\mathbf{S}|$ when the shell is half full.

The previous rules imply that only partly filled shells will provide a magnetic moment.

1.1.2 Magnetic interactions

The magnetic moments will respond to its environment through different interactions. These interactions will contribute to the energy landscape and determine the lowest energy configuration of the magnetisation:

The Zeeman interaction is the interaction occurring between the magnetic moment and an externally applied field $\mathbf{B}$. It is characterised by its Hamiltonian:

$$\mathcal{H}_{Zee} = -\mathbf{m} \cdot \mathbf{B} = \frac{\mu_B}{\hbar}(\mathbf{L} + 2\mathbf{S}) \cdot \mathbf{B} \tag{1.7}$$

This relation shows that it is energetically favourable for the magnetic moments to align with the external field.

The exchange interaction is the interaction between the spins of two neighbouring atoms and is associated to an energy:

$$\epsilon_{ex} = -2J_{ex}\mathbf{S}_i \cdot \mathbf{S}_j \tag{1.8}$$

With $i \neq j$ indicating two neighbouring atoms and J_{ex} the exchange constant. Note that the sign of the exchange constant determines if the spins tend to align parallel ($J_{ex} > 0$) or anti-parallel ($J_{ex} < 0$). This interaction has a short range only occurring between the first neighbour of a given atom. Nevertheless, this interaction introduces some ordering on large scale as it is energetically favourable for all the spins of a system to align.

The magnetic dipolar interaction consists in the interaction between magnetic moments mediated by the dipolar field they generate. A magnetic moment $\mathbf{m}$ will produce a field $\mathbf{B}$ given for any point $\mathbf{r}$ by[15]:

$$\mathbf{B}(\mathbf{r}) = \frac{\mu_0}{4\pi}\left(3\frac{(\mathbf{m} \cdot \mathbf{r})\mathbf{r}}{r^5} - \frac{\mathbf{m}}{r^3}\right) \tag{1.9}$$

With μ_0 the magnetic permeability and $r = |\mathbf{r}|$. This field will interact with other magnetic moments and is characterised by the dipolar interaction energy [16]:

$$\epsilon_d = \frac{\mu_0}{4\pi}\left(\frac{\mathbf{m}_i \cdot \mathbf{m}_j}{r_{ij}^3} - 3\frac{(\mathbf{m}_i \cdot \mathbf{r}_{ij})(\mathbf{m}_j \cdot \mathbf{r}_{ij})}{r_{ij}^5}\right) \tag{1.10}$$

With $i \neq j$ indicating any two distinct magnetic moments.

1.1.3 Micromagnetic equation

The micromagnetic approach consists in defining a magnetic system for any point by a magnetisation distribution $\mathbf{M}$ representing the magnetic moment density $\mathbf{M} = d\mathbf{m}/dV$ with dV an infinitesimal small volume around the considered point. In this context the interactions previously presented will dictate the behaviour of the magnetisation on a microscopic scale through the minimisation of the total free energy of the system [15] [17]:

$$\epsilon_{tot} = E_{ex} + E_{an} + E_s + E_{Zee} + E_d + E_{ms} \tag{1.11}$$

With E_{ex} the energy associated to the exchange interaction, E_{an} the energy coming from the magnetocrystalline anisotropy of the system, E_s the energy coming from the surface anisotropy,

E_{Zee} the energy due to external field interaction with the magnetisation, E_d the energy from induced demagnetisation field also called shape anisotropy and E_{ms} the energy associated to the magnetostriction contributions. This last term is not further developed as it can be neglected in the context of this thesis.

The first term of the free energy equation is the exchange energy contribution. The resulting energy from exchange interaction in the whole system can be expressed as [15]:

$$E_{ex} = \int_V A(\nabla \mathbf{u_M})^2 d^3r \tag{1.12}$$

with $A \propto J_{ex}|\mathbf{S}|^2$ The exchange stiffness and $\mathbf{u_M} = \mathbf{M}/|\mathbf{M}|$ the unit vector of the direction of the magnetisation.

1.1.4 Magnetic anisotropy

In the absence of external fields, the magnetic anisotropy describes the tendency of magnetisation to orient itself along specific directions, called easy axes. The most common types of anisotropies are uniaxial and cubic, depending on the number and symmetry of the easy axes. Anisotropy has different origins that add up to give the total anisotropy.

The **shape anisotropy** comes from demagnetisation field $\mathbf{H}_d$, also called *stray field* outside of the magnetic system. It is the magnetic field generated by all the magnetic moments of the system. In the absence of any other external filed, the total energy associated to the demagnetisation field is defined as [16]:

$$E_d = -\frac{\mu_0}{2} \int_V \mathbf{M} \cdot \mathbf{H}_d d^3r \tag{1.13}$$

With $\mathbf{M}$ the magnetisation at any point of the system and V the volume of the magnetic system. For uniformly magnetised systems, the demagnetisation field can be linked to the magnetisation through the demagnetising tensor N such that:

$$\mathbf{H}_d = -N\mathbf{M} \tag{1.14}$$

N is a tensor characterised by $Tr(N) = 1$ for the case of an ellipsoid. N can be determined for specific geometries such as for the ones studied in this thesis [15]. $N_{\parallel} = 0$ for infinite thin films with magnetisation in-plane, $N_{\perp} = 1$ for films with magnetisation out-of-plane and $N_z \simeq 1$ for short cylinders with magnetisation oriented along its axis. Inserting equation (1.14) into equation (1.13) shows that the demagnetisation energy only depends on the system shape and on the magnetisation direction. This dependency is at the origin of the shape anisotropy as for a given shape the magnetisation will orient itself to minimise the energy.

The **magnetocrystalline anisotropy** describes the impact of the electrical potential created by the crystalline lattice on the orbital angular momentum of the electrons providing magnetic moments. Depending on the crystallographic geometry, the symmetry of the induced fields will energetically favour certain orbital orientations. This will in turn affect the total magnetic moment through spin-orbit coupling. One of the most common kinds of magnetocrystalline anisotropy is uniaxial anisotropy and the associated energy can be expressed as:

$$E_{an} = \int_V K_1 \sin^2\theta d^3r \tag{1.15}$$

With K_1 the uniaxial anisotropy constant and θ is the angle between the magnetisation direction and the associated easy axis.

For very thin films, the **surface anisotropy**, also called interface anisotropy, can dominate over other, previous described, contributions [18]. First put forward by Louis Néel [19], this anisotropy originates from the breaking of symmetry of some of the magnetocrystalline terms at the interface. Each interface, of surface S, is therefore associated with an surface energy[20]:

$$E_s = \int_S \frac{K_s}{d} \cos^2\theta d^2r \tag{1.16}$$

With K_s the surface anisotropy constant, d the thickness of the thin film and θ the angle between the magnetisation direction and the direction normal to the interface. For $K_s < 0$ this anisotropy favours out-of-plane magnetisation. Equation (1.16) imply that there exists a critical thickness d_c bellow which this component will dominate other anisotropies.

1.1.5 Magnetic domains

Large ordered systems can divide themselves into multiple magnetic domains to lower the overall energy. The energy associated with the stray field is the primary source of the domain formation. It results in a competition between the exchange and dipolar interactions.

Magnetic domains are separated by domains walls which act as a transition zone where magnetisation progressively rotates from one direction to the other. For domains of opposite direction, there exist two types of walls depending on the rotation direction. The Bloch wall type is described by a rotation of magnetisation in the plane parallel to the wall. The second type, the Néel wall, is described by a rotation of magnetisation in the plane perpendicular to the wall. The two types of domain walls are illustrated in Figure 1.1.

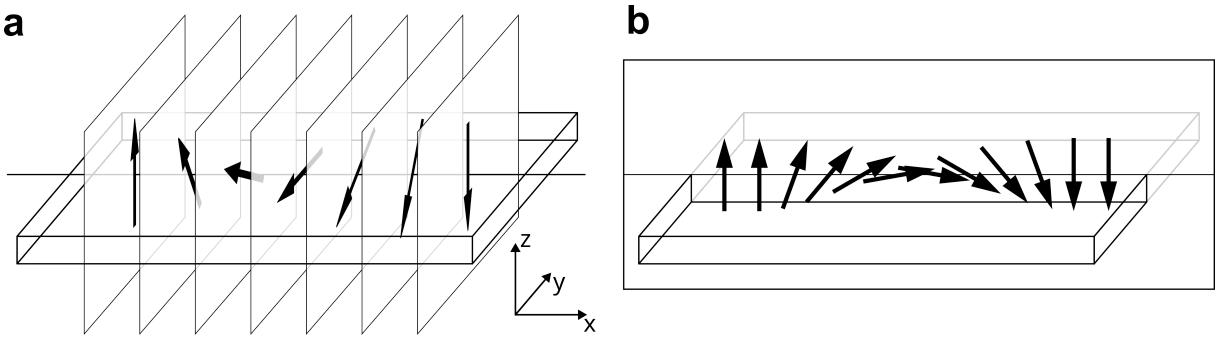

Figure 1.1: Illustration of the different geometries of domain walls. (a) A Bloch domain wall. (b) A Néel domain wall.

Domain walls have an associated energy cost that mainly comes from the exchange interaction which favours aligned neighbour spins but also from the magnetic anisotropy that favours certain magnetisation directions.

For example for a Bloch wall in the (Oyz) plane, in the presence of exchange interaction of stiffness A and for a dominant uniaxial anisotropy of constant K, the energy cost of the wall of surface S is[17]:

$$E_w = E_{ex} + E_{an} = S \int (A \left(\frac{\partial \theta}{\partial x} \right)^2 + K \sin^2 \theta) dx \tag{1.17}$$

With $\theta(x)$ the distribution of the angle between the magnetisation and the anisotropic easy axis. This energy can be minimised for a specific distribution of $\theta(x)$ characterised by the wall width δ_w and minimum total energy $\epsilon_{w,min}$:

$$\delta_w \sim \sqrt{\frac{A}{K}} \tag{1.18}$$

$$\epsilon_{w,min} = 4S\sqrt{AK} \tag{1.19}$$

1.1.6 Field control of magnetisation

The main way to control the magnetisation of a sample is by applying a external magnetic field. Indeed, due to the Zeeman interaction, a torque will be exerted onto the magnetisation to align it with the field direction. Note in the case where the field is applied antiparallel to the magnetisation, the Zeeman interaction yields no torque but in most cases the thermal fluctuations will provide a small perpendicular magnetisation component which will induce a torque.

Magnetic switching by a field can occur in two ways: coherently or through nucleation and domain wall motion. In the first case the magnetisation has a uniform orientation throughout the sample. The field will act on all magnetic moments in the same way and the magnetisation will precess around the effective field $\mathbf{H}_{eff}$ and relax by progressively aligning itself with the effective field. This dynamic is described by the Landau–Lifshitz–Gilbert (LLG) equation [15]:

$$\frac{d\mathbf{M}}{dt} = -\gamma\mu_0 \mathbf{M} \times \mathbf{H}_{eff} + \frac{\alpha}{M_s} \mathbf{M} \times \frac{d\mathbf{M}}{dt} \tag{1.20}$$

With γ the gyromagnetic ratio, μ_0 the magnetic permeability, α the Gilbert damping factor associated to the relaxation and M_s the saturation magnetisation of the system.

For a field to reverse the magnetisation, it has to overcome the anisotropic field of the sample. This can be very costly to achieve in a coherent manner, specially in large samples, therefore, in most magnetic systems the nucleation and domain wall motion process is the main mode of reversal. Most large systems are inhomogeneous and have some defects. These defects locally induce some demagnetisation field that can partially compensate other anisotropies, leading to region with a lower switching field. When this threshold is reached a small domain is formed. The applied field will then induce some domain wall motion to grow the domain with magnetisation aligned with its direction. Sample defects can also hinder movement by locally pining the domain wall. In this case, a higher field is required to unpin the wall. The domain wall speed goes through different regimes depending on the applied field strength: the creep, depining and flow regime[21]. Nucleation and domain wall propagation is slower than coherent switching but require smaller applied fields.

1.2 Magnetic materials

1.2.1 Ferromagnetic materials

Hund's rules imply that most atoms carry a magnetic moment. Still, only a few materials exhibit a net magnetic moment in the absence of a magnetic field. This comes from the fact that materials are, most of the time, paramagnetic, meaning that in a solid, the orientation of the magnetic moments is randomly distributed. This happens when the thermal agitation is stronger than the exchange interaction, which tends to align the magnetic moments.

In contrast, a ferromagnetic material is defined as a material in which all magnetic moments mostly align parallel and therefore presents a net magnetisation. Ferromagnetic materials are characterised by their Curie temperature T_C above which the thermal fluctuation overcomes the exchange interaction strength and the material becomes paramagnetic as illustrated in 1.3 (a). In general, below the Curie temperature, the net magnetisation will increase as the temperature decreases due to smaller thermal fluctuations. This happens until the magnetisation reaches the saturation magnetisation $M_{s,0}$ at 0 K, where all the moments are perfectly aligned.

A ferromagnetic system can be characterised through hysteresis loop measurements, which involve recording the magnetisation M as a function of the applied external magnetic field H. Due to the hysteretic nature of the magnetisation switching process, the field needs to be swept up and down as different magnetic states can occur depending on the applied magnetic field history. By performing these measurements along a few directions, some properties can be extracted, such as the coercive field H_C, which is the field needed for the magnetisation to cross zero. Another value of interest that can be extracted is the remanent magnetisation M_r, which corresponds to the remaining net magnetisation after the field is switched off. Figure 1.2 provides an illustration of a magnetic hysteresis loop. These measurements also provide some information on the anisotropy of the system, such as the easy axis direction and, provided other parameters are known, the anisotropy constants.

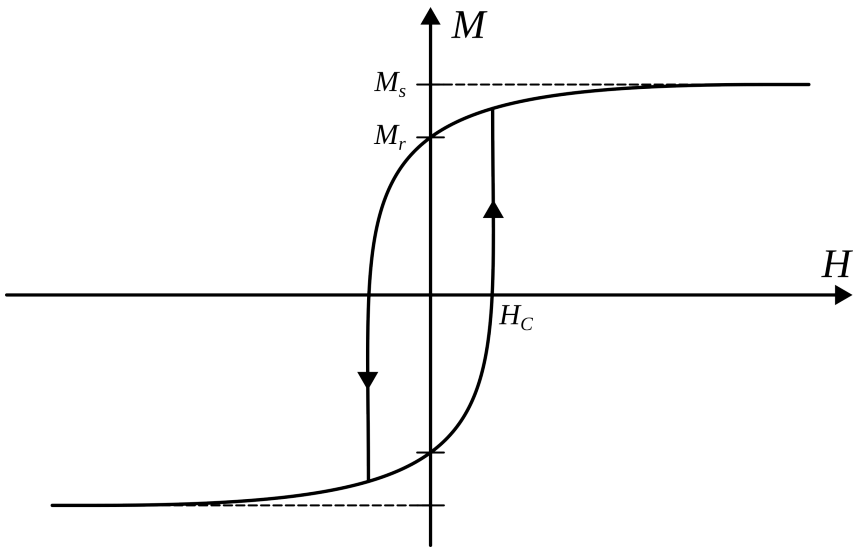

Figure 1.2: Example of a magnetisation versus applied magnetic field curve (hysteresis loop) used to define the saturation magnetisation (M_s), the remanent magnetisation (M_r) and the coercive field (H_c).

The most common ferromagnets are composed of the transition metals Fe, Co and Ni, which have partially filled 3d orbitals, or rare-earth metals, which have partially filled 4f orbitals. These elements can be alloyed or grown as multilayers to give them specific properties.

This thesis focuses on Co/Pt multilayers, a ferromagnetic system with well-studied properties [22] and promising applications. Multilayers composed of thin magnetic layers are interesting as they possess strong perpendicular magnetic anisotropy (PMA) due to the contribution of interface anisotropy[22]. Indeed, the interface contribution described by equation (1.16) adds up for every interface in a multilayer stack and is inversely proportional to the magnetic layer thickness. This means that by repeating alternating thin layers of Co and Pt, the total magnetic moment will increase due to the increasing thickness of magnetic material while conserving strong PMA. The strong coupling between individual layers is mainly due to dipolar coupling introduced through surface roughness or magnetic stray fields in patterned structures.

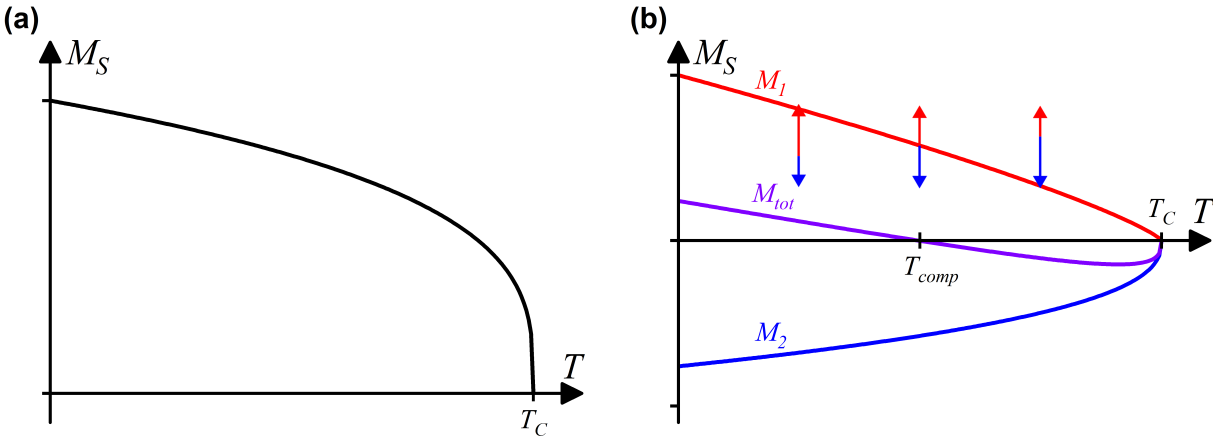

Figure 1.3: Example of the temperature dependence of magnetisation in a (a) ferromagnet and (b) ferrimagnet. In (b), the blue and red curves correspond to the magnetisation of both sublattices (M_1 and M_2), and the purple curve refers to the total magnetisation of the ferrimagnet (M_{tot}).

1.2.2 Ferrimagnetic materials

A ferrimagnet is a material composed of two ferromagnetic sublattices which are coupled anti-ferromagnetically, meaning that the exchange constant between the two sublattice is negative ($J_{12} < 0$), while the exchange constants within the individual sublattice are positive ($J_{11} > 0$ and $J_{22} > 0$). The total magnetic moment is the sum of all magnetic moments in both sublattices. Due to the anti-ferromagnetic coupling, the resulting moment is smaller than the individual sublattices and can be, under certain conditions, equal to zero. In that case, the material can be considered an antiferromagnet. Both sublattices have different dependencies of their magnetisation with respect to temperature. This difference leads to some temperature and composition conditions where the magnetisations of both sublattices compensate each other. The temperature at which the moments compensate is called compensation temperature T_{comp}, as illustrated in Figure 1.3 (b). This temperature depends on the composition of the ferrimagnet [23]. On each side of the compensation temperature, different sublattices dominate and dictate the orientation of the net magnetisation. As net magnetisation approaches zero at the compensation temperature, the coercive field increases and diverges.

The ferrimagnet studied in this thesis is an amorphous GdFeCo alloy with the Gd atoms acting as one sublattice and the FeCo compound being the second sublattice. The composition

of this rare earth (RE) - transition metal (TM) alloy can be modified to tune their relative contribution to the total magnetisation. In these types of alloys, an additional anisotropy component, called pair-order anisotropy (POA), contributes to the PMA. This component originates from short-range ordering and preferential orientation of the different pairs of atoms in the alloy [24]. The origin of PMA is still under debate, as the interface and adjacent material both seem to play significant roles [25].

1.3 Ultrafast spin dynamics

The development of amplified femtosecond laser sources opened the path to the probing of phenomena at a time scale similar to that of light-matter interactions. This led to the study of out-of-equilibrium processes that occur when femtosecond laser pulses irradiate a metal. One such phenomenon is the thermalisation of hot electrons induced by femtosecond pulses with phonons, studied in Cu [26] and Au [27]. It also allowed the study of hot electrons transport in metallic thin films [28]. At that time, the common conception was that the spin response time was of the same order of magnitude as the spin-lattice relaxation time, upwards from tens of picoseconds.

1.3.1 Ultrafast demagnetisation

The first ultra-fast magnetisation dynamics was reported by Beaurepaire et al. in 1996 [7]. By using femtosecond laser pulses, they were able to probe the magnetisation of a Ni sample through the magneto-optical Kerr effect (MOKE) while pumping it with high-fluence 60-fs laser pulses. This magneto-optical pump-probe technique allowed them to reconstruct the magnetisation dynamics at a sub-picosecond time scale. The observed magnetisation dynamics (Figure 1.4) show a sharp drop in magnetisation occurring in less than a picosecond, caused by the pump pulse, followed by a recovery after several picoseconds.

To simulate this ultrafast dynamics, the two-temperature model used to describe electron

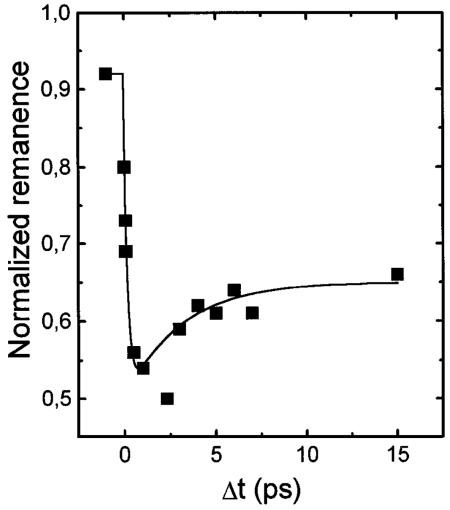

Figure 1.4: Normalised TR-MOKE measurements of the demagnetisation of Ni(20 nm)/MgF2(100 nm) films by a 60 fs laser pulse. Figure taken from [7].

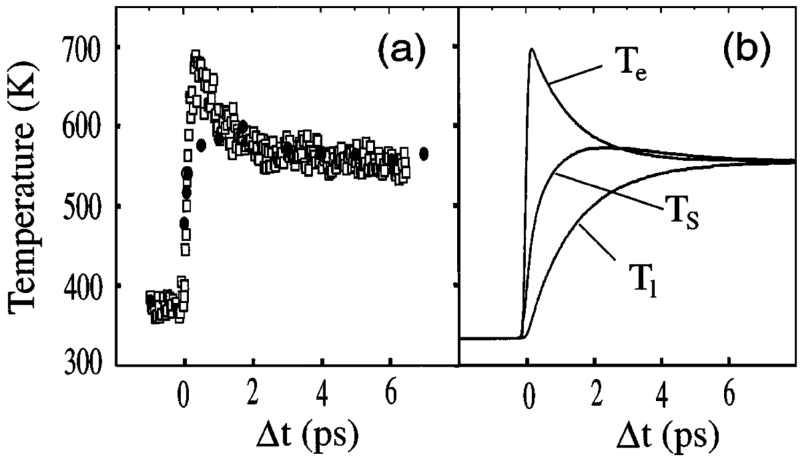

Figure 1.5: (a) Experimental measurements of the electronic temperature (open square) and spin temperature (filled dots). (b) Electrons (T_e), lattice (T_l) and spin (T_S) temperature derived from the 3TM. Figure taken from [7].

thermalisation with the lattice [29] was extended to include a third thermal bath representing the spin system. This three-temperature model (3TM) phenomenologically links the temperatures associated with electrons T_e, phonons T_l, and spins T_s through the following coupled equations [7]:

$$C_e(T_e)\frac{dT_e}{dt} = -G_{el}(T_e - T_l) - G_{es}(T_e - T_s) + P(t) \tag{1.21}$$

$$C_s(T_s)\frac{dT_s}{dt} = -G_{es}(T_s - T_e) - G_{sl}(T_s - T_l) \tag{1.22}$$

$$C_l(T_l)\frac{dT_l}{dt} = -G_{el}(T_l - T_e) - G_{sl}(T_l - T_s) \tag{1.23}$$

With C_i the specific heat capacity of the corresponding sub-system and G_{ij} the interaction constants describing the energy transfer between baths. $P(t)$ represents the time-dependent laser excitation source, which is only applied to the electrons. This basic model adequately captures the measured electron temperature and magnetisation dynamics as shown in Figure 1.5. Nevertheless, the model has some shortcomings as it doesn't consider angular momentum transfer nor other microscopic mechanisms, and it considers a homogeneous population of electrons and phonons without any internal interactions. The model has been extended to integrate other effects in particular systems [30].

The work by Beaurepaire et al. established the field of ultrafast spintronics, focusing on the study and control of magnetisation on sub-picosecond time scales.

1.3.2 All-optical helicity-independent switching

The first observation of all-optical helicity independent switching (AO-HIS) was reported in 2011 by Radu et al. [8]. Using a 60 fs linearly polarised laser pulse with a wavelength of 800 nm, they showed that the magnetisation of a GdFeCo thin film with PMA can locally be reversed on a time scale of picoseconds. By using elements-specific time-resolved XMCD measurements with a resolution of 100 fs, they extracted the dynamics of the Fe and Gd sublattices. The results showed that the demagnetisation times of those two lattices are different, with the Fe lattice fully

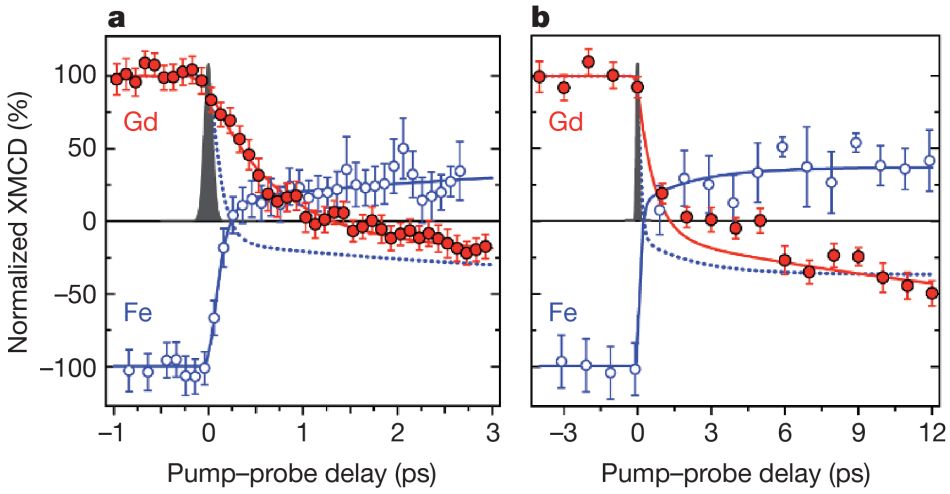

Figure 1.6: Normalised Fe (open blue circles) and Gd (filled red circles) elements specific time-resolved XMCD measurements. (a) Dynamics of the first 3 ps with a 100 fs time resolution, (b) Dynamics of the first 12 ps with a 1 ps time step. The blue dashed line is a guide for the eye of the mirrored dynamics of the Fe sublattice. Figure taken from [8].

demagnetising and crossing zero in about 300 fs. In contrast, the Gd lattice takes around 1.5 ps to cross zero magnetisation, as shown in Figure 1.6. After reaching zero, the magnetisation of both sublattices changes sign and seems to recover on a longer time scale.

The ultrafast magnetisation dynamics of this system is explained in the following way: the Fe lattice demagnetises, as the demagnetisation of the Gd takes more time, some of the Gd's lost angular momentum is transferred to the Fe, causing its magnetisation to grow parallel to the Gd magnetisation. The Gd sublattice magnetisation reaches zero; at that point, the Fe is recovering and transfers some angular momentum of opposite direction back to the Gd magnetisation, causing it to cross zero. Finally, the magnetisation amplitude of both sublattices recovers on a longer time scale as they cool down. The transient ferromagnetic state was later further investigated as a criterion for AO-HIS[31].

Following these results, Ostler et al. further studied this mechanism and put forward its behaviour [32]. From static MOKE imaging after a certain number of 100-fs-long linearly polarised laser pulses, they highlighted the deterministic toggle switching nature of AO-HIS, which means that above a threshold fluence, the magnetisation switches from its initial state to the opposite one. If a second pulse is then sent, the magnetisation switches back to the initial state. Furthermore, since the laser pulses were linearly polarised, they carry no angular momentum and thus only transfer energy to the system in the form of heat. The ultra-fast heating-driven mechanism behind AO-HIS is therefore more general, as it was later demonstrated by Yang et al. that the heat carried by a single 9 ps electric pulse can similarly reverse the magnetisation of GdFeCo [33].

AO-HIS is not exclusive to the GdFeCo alloy as it has been observed in other RE-TM ferrimagnetic amorphous alloys such as GdCo [35], GdTbCo[35][36] and TbCo [37]. It has also been seen in synthetic ferrimagnetic systems such as Gd/Co [38] and Tb/Co [39] multilayer thin films. All these systems have different compositions, fluence and pulse duration criteria to exhibit AO-HIS. To characterise their behaviour and compare them, state diagrams are produced that put forward the range of parameters where the system switches or breaks down into a stochastic

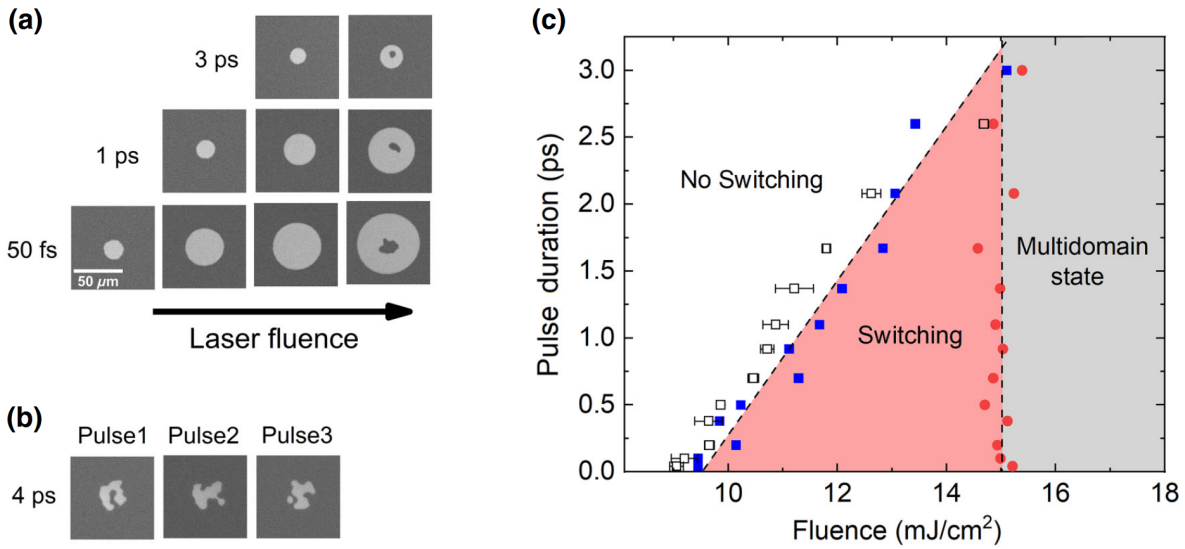

Figure 1.7: All-optical helicity-independent switching behaviour of a $Gd_{24}(FeCo)_{76}$ thin film. (a) MOKE images of the final states after irradiation by a single laser pulse of specified pulse duration and increasing laser fluence. (b) MOKE images of the final states after 1, 2 and 3 pulses of 4 ps. (c) State diagram illustrating the switching and multi-domain ranges as a function of pulse duration and laser fluence. Figure taken from [34].

multi-domain state. In this way, the study of Wei et al.[34] put forward the pulse duration dependence of the threshold fluence above which a given system will switch through irradiation by a single laser pulse, as shown in Figure 1.7.The switching threshold fluence increases with the pulse duration. The maximum pulse duration for which switching is observed is limited by the thermally induced multi-domain state threshold fluence, above which the sample locally breaks down into multiple domains. In the multi-domain regime, the system loses its deterministic toggle switching as shown in Figure 1.7(b).

Vergès et al. showed that the multi-domain state threshold is highly impacted by the thermal state of the system after the electron-phonon equilibration time [40]. Increasing the thermal dissipation of the system, by adding some Cu heat-sink next to the magnetic layer, will increase the multi-domain threshold fluence without affecting the switching threshold. This results in a broader switching fluence range and higher maximum pulse durations, up to tens of picoseconds.

1.3.3 All-optical helicity-dependent switching

Another type of laser-induced switching, named all-optical helicity-dependent switching (AO-HDS) of magnetisation, was first reported in 2007 by Stanciu et al.[9]. They showed that circularly polarised femtosecond laser pulses can selectively manipulate the magnetisation of a GdFeCo thin film. By sweeping a pulsed beam with a repetition rate of 1 kHz and with a wavelength of 800 nm over domains with opposite perpendicular magnetisation, they could dictate the final magnetisation state of the irradiated region through the helicity of light, as shown in Figure 1.8.

Although both types of all-optical switching can be observed in GdFeCo, AO-HDS is the more common phenomenon occurring in a broader range of materials such as RE-TM ferrimagnetic alloys[41] [42] and RE-TM synthetic multilayer ferrimagnet[41], but also in ferromagnetic

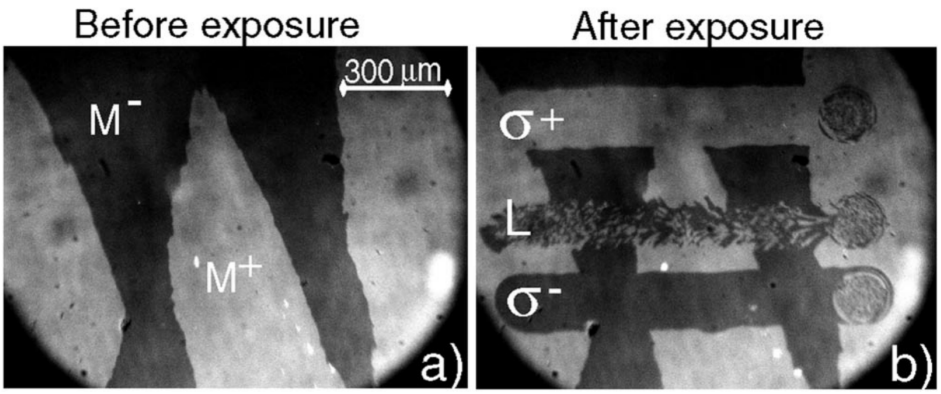

Figure 1.8: All-optical helicity-dependent switching experiment in a $Gd_{22}Fe_{74.6}Co_{3.4}$ thin films. (a) MOKE image of the initial magnetisation state before the laser sweep. (b) MOKE image of the final magnetisation state after the laser sweep. M^- (in black) and M^+ (in white) correspond to the two opposite magnetisation directions. σ^-, σ^+ and L correspond to circular left, circular right and linear light polarisation, respectively. Figure taken from [9].

multilayer films [43] and granular media[44].

Kichin et al. studied the static AO-HDS in Co/Pt ferromagnetic multilayers [45]. They produced a state diagram that compiles the switching and multi-domain threshold for different pulse durations and spot sizes as shown in Figure 1.9. This state diagram has a different shape than the one for AO-HIS. The difference is mainly in the behaviour of the multidomain threshold that is linear with the pulse duration. This leads to a bigger switching fluence window for longer pulses. This study demonstrated full switching of Co/Pt multilayers with as little as 50, 1 ps long pulses.

Medapalli et al. further studied the AO-HDS behaviour in Co/Pt ferromagnetic multilayers

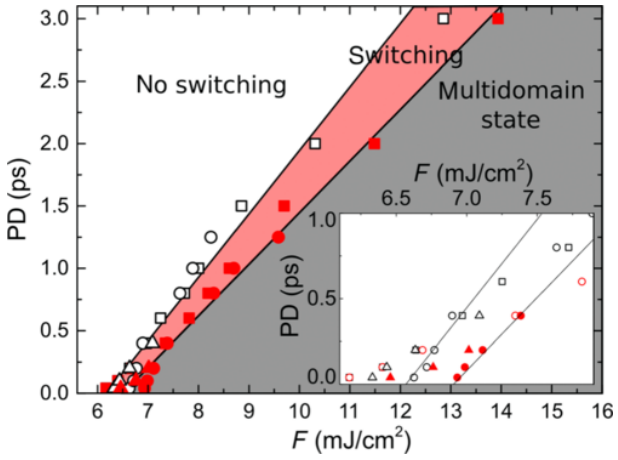

Figure 1.9: State diagram of AO-HDS in Co/Pt multilayers. The different symbols correspond to a laser spot size of 84 µm (triangles), 104 µm (squares) and 168 µm (circles). The open symbols denotes the switching threshold while the filled symbols correspond to the multi-domain threshold. The insert is a zoom-in of the diagram for short pulses. Figure taken from [45].

[46]. They showed that multiple laser pulses are needed to achieve complete reversal of the magnetisation and that the pulse duration has an impact on the switching efficiency. They provided a two-step description of magnetisation switching, consisting of partial demagnetisation of the film by the first few laser pulses, resulting in the nucleation of magnetic domains, followed by helicity-dependent expansion or collapse of these domains through domain wall motion induced by subsequent laser pulses.

This two step process inspired Yamada et al. to employ pairs of pump pulses to drive AO-HDS [47]. They showed that the combination of an intense linear polarised femtosecond pulse that demagnetises the sample followed by a circularly polarised 3 ps long laser pulse of much weaker intensity could lead to complete magnetisation reversal with only five pulse pairs.

The presence of two distinct steps was further corroborated by Huang et al.[48], who measured the magnetisation dynamics after each laser pulse with microsecond time resolution via the anomalous Hall effect. They showed that for each pulse there are two dynamic regimes: first, in less than a microsecond after the pulse, the magnetisation experiences a sharp jump associated with the nucleation of opposite domains, followed by a relaxation on a much longer times scale related to domain wall motion, as shown in Figure 1.10. The magnitude and sign of both, jumps and relaxation strongly depend on the helicity and fluence of the light and on the net magnetisation of the sample. Based on those measured dependencies, the authors could identify fast helicity-dependent domain nucleation as the main driving force for magnetisation reversal from the saturated state $m = -1$, to an unsaturated reversed state with $m \simeq 0.2$, while the subsequent evolution to a fully reversed state is driven by helicity-dependent domain wall dynamics.

The physics of magnetisation reversal by helicity-dependent nucleation of opposite domains can be understood by the model of Gorchon et al.[49] and Ellis et al. [50]. The authors explained AO-HIS in granular FePt-based media in terms of an Arrhenius Neel Brown law [51] [52] describing the rates $r^{\pm}$ at which the magnetisation of individual grains switches from $\pm$ to $\mp$ by

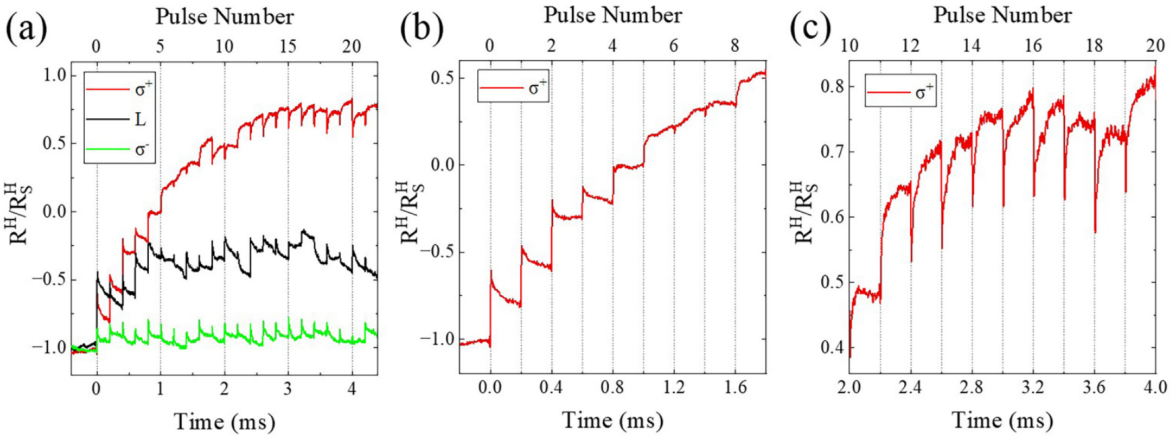

Figure 1.10: Normalised time-resolved Hall resistance measurements of all-optical helicity-dependent switching of Co/Pt Hall crosses for a laser repetition rate of 5 kHz. (a) Dynamics induced by circular left (σ^-), circular right (σ^+) and linear (L) polarised laser pulses. (b) Detail view of the first 1.6 ps. (c) Detail view from 2 ps to 4 ps. Figure taken from [48].

thermal activation:

$$r^{\pm} = f_0 \cdot e^{-E_{\mathrm{B}}(T^{\pm})/(k_B T^{\pm})} \tag{1.24}$$

with f_0 the material specific attempt frequency, E_B the energy barrier, $k_B = 1.380{\cdot}10^{-23}\mathrm{JK}^{-}1$ the Boltzmann constant and $T^{\pm}$ the temperature of opposite magnetisation directions. The net magnetisation change is $r^{+}N^{+} - r^{-}N^{-}$, where $N^{\pm}$ are the total number of grains with magnetisation $\pm$. Imbalanced transition rates lead, after a large number of attempts, to the final, normalised equilibrium magnetisation:

$$m_{\mathrm{eq}} = \frac{r^{+} - r^{-}}{r^{+} + r^{-}} \tag{1.25}$$

The mechanism behind AO-HDS is still highly debated as two prominent explanations are put forward: magnetic circular dichroism (MCD) and the inverse Faraday effect (IFE).

Magnetic circular dichroism refers to the difference in light absorption between opposite circular polarisation states for a given magnetisation, or equivalently, the difference in light absorption between opposite magnetisation directions for a given circular polarisation.

In the context of the previously presented model, the MCD would lead to a difference in temperature between opposite magnetisation directions for a given circular polarisation $T^{\pm}$ and thus different switching rates, $r^{+} \neq r^{-}$.

Using this model, Gorchon et al. [49] showed that it should be possible to achieve full magnetisation reversal of granular FePt with only ten laser pulses as long as MCD $\geq 0.5\%$. This is due to the extreme sensitivity of $r^{\pm}$ to slight differences of $T^{\pm}$ resulting from the divergence of dE_{B}/dT in the vicinity of the Curie temperature and the exponential relation between E_{B}/kT and r. Note that experiments in FePt only showed a partial switching of 10-20% [43][53].

The second proposed mechanism for AO-HDS is the **inverse Faraday effect**. This effect was first derived by Pitaevskii in 1961 [54] and later further developed and checked by van der Ziel et al. in 1965[55] and by Pershan et al. in 1966 [56]. The IFE describes the induction of magnetisation by the circular polarisation of light. The induced magnetisation can be expressed as

$$\mathbf{M}_{IFE} = \chi[\mathbf{E} \times \mathbf{E}^{*}] \tag{1.26}$$

With $\mathbf{E}$ the electric field of the light in the material. In a non-magnetic and non-absorbing material, χ is identical to the magneto-optical susceptibility of the material, which also comes into play in the Faraday effect. This mechanism does not rely on absorption, as it is observed also in non-absorbing materials. Indeed, the first recent demonstration of of IFE by Kimel at al, showed helicity-dependent induced precession in almost non-absorbing $DyFeO_3$ [57]. They associated this observation with the generation of an effective magnetic field by the circular polarised light.

Hertel et al. developed a classical description of the IFE based on macroscopic drift current induced by the electric field of light [58] [59]. Based on quantum theoretical calculations Battiato et al. showed that the description of the IFE via Equation 1.26 holds for absorbing media [60], but that χ differs from the susceptibility describing the ordinary Faraday effect. Using DFT calculations, Berritta et al. studied the IFE in both magnetic and non-magnetic materials [61]. They highlighted the presence of both spin and orbital induced magnetisation and showed that

in the case of magnetic materials, the antisymmetry of the response is broken, leading to an asymmetric response and even in some cases a response of the same sign for opposite helicities. Based on the microscopic three-temperature model (M3TM) proposed by Koopmans et al.[62], Cornelissen et al. showed that the inclusion of the IFE effective field can explain AO-HDS in ferromagnets such as Co/Pt [63].

When considering Equation 1.25, distinct rates for opposite magnetisation will always lead to (partial) AO-HDS, independently of the root cause for this difference. Thus, AO-HDS could also originate from a perpendicular magnetic field induced by IFE, $\mathbf{H}_{\mathrm{IFE}}$. This is best illustrated by describing the energy barrier in terms of the Stoner model for media with an effective perpendicular magnetocrystalline anisotropy K' and saturation magnetisation M_S

$$E_{\mathrm{B}}^{\pm} = \frac{K'(T)V}{k_B T}\left(1 \pm \frac{H_{\mathrm{IFE}}}{H'_K(T)}\right)^2 , \tag{1.27}$$

where

$$H'_K(T) = \frac{2K'(T)}{\mu_0 M_S(T)} . \tag{1.28}$$

Analogous to the MCD case, opposite magnetisation have to overcome distinct energy barriers for their reversal which leads to distinct transition rates $r^{\pm}$ and thus a final equilibrium magnetisation given by Equation 1.25. This similarity in observable consequences of MCD and IFE makes it difficult to disentangle them.

Attempts to separate contributions of MCD and IFE become even harder with regard to the second step of AO-HDS in continuous films, driven by domain wall motion or relaxation. Magnetic domains of opposite direction are heated differently due to MCD, causing a thermal gradient perpendicular to the domain wall. This thermal gradient generates domain wall motion due to the spin Seebeck effect [64] [65], favouring the expansion of the coldest domain. Alternatively, the transient magnetisation generated via IFE can favour the expansion of the domains parallel to the induced magnetisation. In addition, helicity independent dipolar interactions tend to favour straight domain walls which could help to complete the switching from a unsaturated reversed state [48]. The impact of domain formation on AO-HDS provides criteria for the typical domain size that media can sustain [66] and their domain wall dynamics [67]. Moreover, pinning will counteract domain wall motion so that the experimental results will be sensitive to the distribution and strength of pinning sites. The multitude of possible origins and mechanisms behind the observed domain wall motion results in ongoing debates in the literature.

Medapalli et al.[46] argued that their measured values of domain wall displacement per laser pulse strongly favour long lived MCD related temperature gradients as their driving force. In contrast, double pump experiments by Li et al [68] showed that the impact of the pulse ellipticity on domain wall motions is instantaneous and lasts only for times comparable to the pulse duration, as expected for the action of the IFE. A systematic study on domain wall displacements induced by elliptically polarised light pulses by Quessab et al. [69] led to the conclusion that the impact of the light ellipticity on domain wall motion could be explained by MCD and/or IFE and highlighted the critical role of pinning. The study of Huang highlighted the crucial role of dipolar field driven domain wall motion at times larger than a microsecond[48].

Another possible mechanism behind AO-HDS, put forward by Scheid et al. [70], is **magnetisation induced by light absorption** (MILA). This effect takes into account the direct

transfer of angular momentum from the incident light to the magnetic material. The induced magnetisation change is anti-collinear with the magnetisation and always causes demagnetisation, but the amount of demagnetisation is helicity-dependent. No experimental studies have demonstrated this effect.

The contributions of these different effects toward AO-HDS are complicated to disentangle. Nevertheless, Yamada et al. recently studied the AO-HDS efficiency in Co/Pt full films at different wavelengths and correlated it to the spectral behaviour of MCD and IFE [71]. They put forward that the monotonous increase of the efficiency of magnetisation switching coincides with the MCD spectrum but not with the IFE spectrum, which suggest a dominant contribution from MCD.

This thesis aims at distinguishing the roles of MCD and IFE in AO-HDS. To achieve this, characteristic features are imprinted into both the MCD and IFE spectra using magneto-plasmonic resonances. Plasmonic resonances and their impact on magneto-optical effects are discussed in the next chapter.

To conclude, the characteristics of different types of all-optical switching are summarised in the following table:

	All-optical helicity-independent switching (**AO-HIS**)	All-optical helicity-dependent switching (**AO-HDS**)
Magnetisation control	Toggles the magnetisation	Final magnetisation dictated by the helicity of light
Switching nature	Deterministic	Stochastic
Number of pulses	1	Multiple
Pulse duration	The shorter the less fluence is needed	Optimal pulse duration ~ 1 ps
Switching time	~ 1 ps	$> 1\ \mu s$
Materials	RE-TM ferrimagnet	Wide range of materials
Origin	Ultrafast thermally demagnetisation	Still debated (IFE, MCD)

Chapter 2

Plasmonics and magneto-plasmonics

This chapter covers plasmonics, specifically the plasmonic resonances occurring in the systems studied in this thesis. This will be followed by a description of the physics underlying the magneto-optical effects considered in this thesis, as well as the impact of plasmonic resonances on the magneto-optical response. The last section of this chapter is dedicated to the state-of-the-art in magneto-plasmonics and the control of magnetism in magneto-plasmonic structures.

2.1 Plasmonics

2.1.1 Electromagnetic waves in solids

The interaction between an electromagnetic wave and matter is dictated by the Maxwell equations. In the frequency domain and for oscillating fields following the convention $\mathbf{F}(\mathbf{r},t) = \mathbf{F}_0(\mathbf{r})e^{-i\omega t}$, the macroscopic Maxwell equations can be written as [72] [73]:

$$\nabla \cdot \mathbf{D}(\mathbf{r},\omega) = \rho_{ext}(\mathbf{r},\omega) \tag{2.1a}$$

$$\nabla \cdot \mathbf{B}(\mathbf{r},\omega) = 0 \tag{2.1b}$$

$$\nabla \times \mathbf{E}(\mathbf{r},\omega) = i\omega\mathbf{B}(\mathbf{r},\omega) \tag{2.1c}$$

$$\nabla \times \mathbf{H}(\mathbf{r},\omega) = -i\omega\mathbf{D}(\mathbf{r},\omega) + \mathbf{J}_{ext}(\mathbf{r},\omega) \tag{2.1d}$$

With $\mathbf{D}$, $\mathbf{B}$, $\mathbf{E}$ and $\mathbf{H}$, the electric displacement field, the magnetic flux density, the electric field and the magnetic field, respectively. ρ_{ext} denotes the external charge density and $\mathbf{J}_{ext}$ is the external current density.

In linear media and in the absence of any macroscopic charges or currents ($\rho_{ext} = 0$ and $\mathbf{J}_{ext} = 0$), an electromagnetic wave will cause an oscillatory response from media characterised by the induced polarisation vector $\mathbf{P}$ and the induced magnetisation vector $\mathbf{M}$:

$$\mathbf{P}(\mathbf{r},\omega) = \epsilon_0\chi_e(\mathbf{r},\omega)\mathbf{E}(\mathbf{r},\omega) \tag{2.2}$$

$$\mathbf{M}(\mathbf{r},\omega) = \mu_0\chi_m(\mathbf{r},\omega)\mathbf{H}(\mathbf{r},\omega) \tag{2.3}$$

With ϵ_0 and μ_0 the vacuum permittivity and permeability, and χ_e and χ_m the electric and magnetic susceptibility, respectively. These responses will add up to the free space contribution to give the total displacement field and the total magnetic flux density described by the constitutive equations [73]:

$$\mathbf{D} = \epsilon_0\mathbf{E} + \mathbf{P} = \epsilon_0(1+\chi_e)\mathbf{E} = \epsilon_0\epsilon_r\mathbf{E} \tag{2.4}$$

$$\mathbf{B} = \mu_0\mathbf{H} + \mathbf{M} = \mu_0(1+\chi_m)\mathbf{H} = \mu_0\mu_r\mathbf{H} \tag{2.5}$$

With $\epsilon_r = (1+\chi_e)$ and $\mu_r = (1+\chi_m)$ representing the material relative permittivity (sometimes called dielectric constant) and permeability. Note that all the variables in the two previous equations depend on the position vector $\mathbf{r}$ and on the angular frequency ω; the dependency notation was omitted for clarity purposes. At optical frequencies, the permeability of materials can be neglected as the induced magnetisation cannot follow the light's field oscillation frequency.

In the presence of an electromagnetic field, electrons are driven by the Lorentz force:

$$\mathbf{F}_L = -e(\mathbf{E} + v \times \mathbf{B}) \tag{2.6}$$

With $e \simeq 1.602 \cdot 10^{-19}$C the elementary charge and v the speed of the electrons. At optical frequency, the force of the oscillating magnetic field on the electrons, described through the second term of this equation, is neglected.

The motion of electrons $\mathbf{r}_e$ in a media with an oscillating electric field $\mathbf{E}$, can be derived from the classical motion equation:

$$m_e\frac{d^2\mathbf{r}_e}{dt^2} = e\mathbf{E} - m_e\gamma_e\frac{d\mathbf{r}_e}{dt} - k_e\mathbf{r}_e \tag{2.7}$$

With $m_e = 9.109 \cdot 10^{-31}$kg the mass of an electron, γ_e the damping coefficient of collision frequency and k_e the spring coefficient associated with the restoring force for bound electrons.

For an oscillating electric field following the convention $\mathbf{E}(\mathbf{r},t) = \mathbf{E}_0(\mathbf{r})e^{-\omega t}$, the electron's motion equation can be rewritten in the frequency domain as:

$$\mathbf{r}_{e,0}(\mathbf{r}) = \frac{e}{m_e}\frac{E_0(\mathbf{r})}{\omega_0^2 - \omega^2 - i\omega\gamma} \tag{2.8}$$

With $\omega_0 = \sqrt{k_e/m}$, the resonance frequency of the bound oscillator. This equation can be linked back to the polarisation vector in a medium through:

$$\mathbf{P} = N_e e\mathbf{r}_e = \epsilon_0 \frac{\omega_p^2}{\omega_0^2 - \omega^2 - i\omega\gamma}\mathbf{E_0}(\mathbf{r}) \tag{2.9}$$

With N_e the electron density and ω_p the plasma frequency:

$$\omega_p = \sqrt{\frac{Ne^2}{\epsilon_0 m_e}} \tag{2.10}$$

By association with Equation 2.2, the relative permittivity can be retrieved. The complex permittivity of a linear, isotropic material can be linked back to its complex refractive index $N = n + i\kappa$ through $N = \sqrt{\epsilon}$, which can be measured with ellipsometry. Two specific cases can be highlighted.

At photon energies below the interband transition threshold, a metallic material can be modelled as free electrons in a fixed ion lattice ($\omega_0 = 0$). In that case, the motion of the electrons induced by an oscillating electric field leads to a permittivity described by the Drude dielectric function [72]:

$$\epsilon_r(\omega) = 1 - \frac{\omega_p^2}{\omega^2 + i\omega\gamma_e} \tag{2.11}$$

In the case of an interband transition, the motion of the associated electrons can be described as a bound oscillator. This leads to the Lorentz dielectric formula [72]:

$$\epsilon_r(\omega) = 1 + \frac{\omega_{p,i}^2}{\omega_{0,i}^2 - \omega^2 - i\omega\gamma_{e,i}} \tag{2.12}$$

With $\omega_{p,i}$ the plasma frequency associated with these electrons, $\gamma_{e,i}$ the damping coefficient and $\omega_{0,i}$ the resonance frequency of the bound oscillator. This formula can also be used for dielectric materials.

The permittivity of metals can therefore be described as the sum of a Drude component (Equation 2.11) and multiple Lorentz components (Equation 2.12 excluding the first term 1) to take into account all interband transitions.

2.1.2 Plasmons

In the absence of external charges or currents, the wave equation in the media can be retrieved from Maxwell's equations (Equation 2.1) [74]:

$$\mathbf{k}(\mathbf{k}\cdot\mathbf{E}) - k^2\mathbf{E} = -\epsilon(\mathbf{k},\omega)\frac{\omega^2}{c^2}\mathbf{E} \tag{2.13}$$

With $\mathbf{k}$ the wave vector and c the speed of light in vacuum. This equation has two types of solutions depending on the relative directions of $\mathbf{k}$ and $\mathbf{E}$. For solutions with $\mathbf{E}$ orthogonal to $\mathbf{k}$

or transverse modes, the previous equation provides the following dispersion relation associated with a propagative mode:

$$k^2 = \epsilon(\mathbf{k}, \omega)\frac{\omega^2}{c^2} \tag{2.14}$$

For **E** along **k** or longitudinal modes, the wave equation is verified only when $\epsilon(\mathbf{k}, \omega) = 0$. If the Drude model is considered for the permittivity (Equation 2.11), then this condition is validated at the plasma frequency $\omega = \omega_p$ if the damping is neglected ($\omega_p \gg \gamma_e$). This corresponds to a non-propagating collective oscillation known as volume plasmon.

There is a third type of solution that corresponds to a mode that only exists at the interface between a metal of permittivity ϵ_m and a dielectric of permittivity ϵ_d of opposite sign. This mode is characterised by the following dispersion relation:

$$\mathbf{k}_{SPP} = \frac{\omega}{c}\sqrt{\frac{\epsilon_m \epsilon_d}{\epsilon_m + \epsilon_d}} \tag{2.15}$$

This surface mode, known as a surface plasmon polariton (SPP), is described by a coupled propagating oscillation between the electromagnetic field and the free electrons at the metal surface. It is a transverse magnetic mode that exhibits evanescent behaviour in the direction normal to the interface in both the metal and the dielectric, confining the wave's energy to the interface. This mode has an upper frequency limit ω_{SP} that can be analytically assessed for a metal described by Drude's model with negligible damping:

$$\omega_{SP} = \frac{\omega_p}{\sqrt{1 + \epsilon_d}} \tag{2.16}$$

Above this frequency and below the plasma frequency, the damping becomes non-negligible,

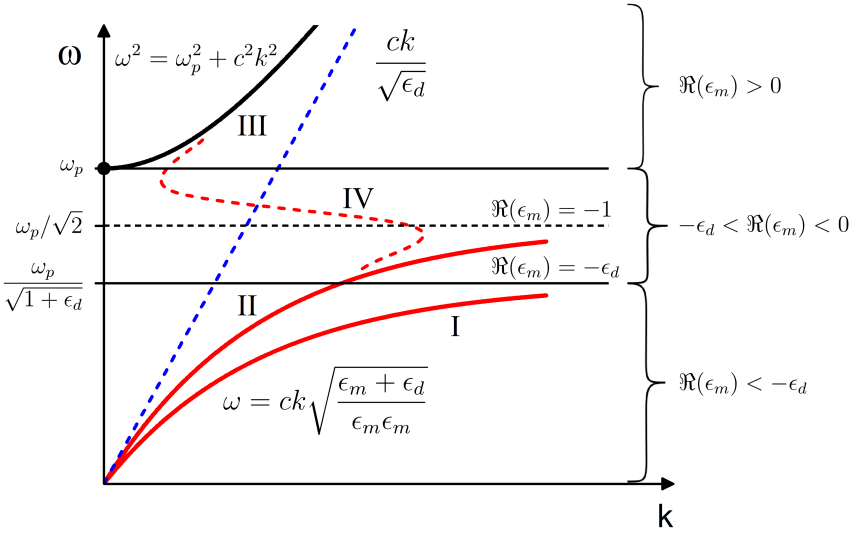

Figure 2.1: Dispersion relation of (I) an SPP at the interface between a metal and a dielectric material without damping, (II) an SPP at the interface between a metal and air without damping as representation of a limit case, (III) light propagating in the bulk metal described by Drude's model without damping and (IV) an SPP transition mode or quasi-bound mode where damping dominates. The blue dashed line corresponds to light propagation in the bulk dielectric material. Reproduced and adapted from [75].

which leads to a transition quasi-bound mode between the SPP and bulk propagating modes, as shown in (IV) in Figure 2.1.

Figure 2.1 highlights the wave vector mismatch between the SPP mode and the light propagating in the dielectric material. This makes the excitation of the SPP mode through direct illumination impossible. To couple to SPP modes, indirect excitation schemas are needed to compensate for the wave vector mismatch.

One technique involves using the evanescent wave produced during internal total reflection in a prism with a higher optical index than the dielectric material at the SPP interface. Two configurations exist: (i) a small gap can be left between the prism and the metal surface, and (ii) the metallic material can be deposited as a thin film directly onto the prism. The generated evanescent wave extends through the gap or the metal thickness to couple with the dielectric metal interface. By carefully choosing the optical index of the prism, the mismatch can be compensated by modifying the internal reflection angle to vary the in-plane wave vector to be equal to the SPP mode wave vector according to the following relation:

$$k_{SPP} = k_0 n_{prism} \sin(\theta_{inc}) \tag{2.17}$$

With k_0 the incident wave vector, n_{prism} the optical index of the prism and θ_{inc} the incident internal reflection angle.

Another way to couple to SPP modes is through the use of gratings. Periodic structures diffract the light in different directions depending on the frequency and angle of the incident light. When the light is diffracted into the plane of the grating, it can couple to a SPP mode if the wave vector mismatch is compensated by the grating periodicity, as conveyed by the following relation [76]:

$$\mathbf{k}_{SPP} = \mathbf{k}_{0,\parallel} \pm n\frac{2\pi}{P}\mathbf{e}_g \tag{2.18}$$

With $\mathbf{k}_{0,\parallel}$ the in-plane component of the incident wave vector, $n \in \mathbb{N}$ denoting the diffraction order, P the periodicity of the grating and $\mathbf{e}_g$ the grating unit vector.

2.1.3 Localised surface plasmon resonance

Localised surface plasmons (LSP) are non-propagating oscillations of the conduction electrons confined in a metallic nanostructure coupled to the electromagnetic field. For nanometric-sized particles, the charge displacement induced by the electric field is met by a restoring force. Thus, the particle acts as an oscillator that can resonate under specific conditions. This resonance, known as localised surface plasmon resonance (LSPR), can be directly excited in free space without the need for any coupling techniques. These oscillations can be described in different regimes by different theories and/or approximations.

The quasi-static approximation allows for the depiction of the interaction of light with a nanoparticle, provided a few assumptions. The electric field inside the particle needs to be considered constant and uniform. This reduces the problem to an electrostatic one. This assumption is reasonable for particle sizes that are small compared to the wavelength of the incident light. For a spherical metallic particle of radius $a \ll \lambda$ of permittivity ϵ_m surrounded by a dielectric material of permittivity ϵ_d, the electrostatic calculation provides a expression of the equivalent dipole moment $\mathbf{p} = \epsilon_d \alpha \mathbf{E}_0$ with $\mathbf{E}_0$ the incident static electric field and α the polarisability of the nanoparticle [75] [77]:

$$\alpha = 4\pi a^3 \frac{\epsilon_m - \epsilon_d}{\epsilon_m + 2\epsilon_d} \tag{2.19}$$

The scattering σ_{sca} and absorption σ_{abs} cross sections can be calculated from the polarisability using the following formula [78]:

$$\sigma_{sca} = \frac{k_0^4}{6\pi}|\alpha|^2 = \frac{8\pi}{3}k_0^4 a^6 \left|\frac{\epsilon_m - \epsilon_d}{\epsilon_m + 2\epsilon_d}\right|^2 \tag{2.20}$$

$$\sigma_{abs} = k_0 \Im(\alpha) = 4\pi k_0 a^3 \Im\left(\frac{\epsilon_m - \epsilon_d}{\epsilon_m + 2\epsilon_d}\right) \tag{2.21}$$

With k_0, the incident wave vector.

This analytical solution can be extended to ellipsoidal particles with half-axes a, b, and c. In this case, the diagonal terms of the polarisability matrix can be written as [77]:

$$\alpha_i = 4\pi abc \frac{\epsilon_m - \epsilon_d}{3\epsilon_d + 3L_i(\epsilon_m - \epsilon_d)} \tag{2.22}$$

With L_i the shape factor of the ellipsoid such that $\sum_i L_i = 1$. This polarisability formula highlights the LSPR condition that occurs when the denominator tends towards zero. This may occur because the permittivity of the particle and the surrounding dielectric material are wavelength-dependent, and the real parts have opposite signs. This resonance can be observed in the optical spectrum of such systems as an increase at the resonance wavelength of the extinction cross section, which is the sum of the absorbed and scattered cross sections.

Analytical solutions for particles that are too big with respect to the wavelength to satisfy the quasi-static approximation can be calculated through Mie theory. It provides a comprehensive electrodynamic description of the interaction of light with a spherical particle, from which the scattering and absorption cross sections can be derived. This model can be extended to describe spheroidal particles [79] and arbitrary shaped particles [80].

A more general approach is to solve Maxwell equations for a given geometry numerically. This can be done through the finite difference method (FDM) or the finite element method (FEM) in the frequency domain to obtain the spectral response of a system. This approach was used in

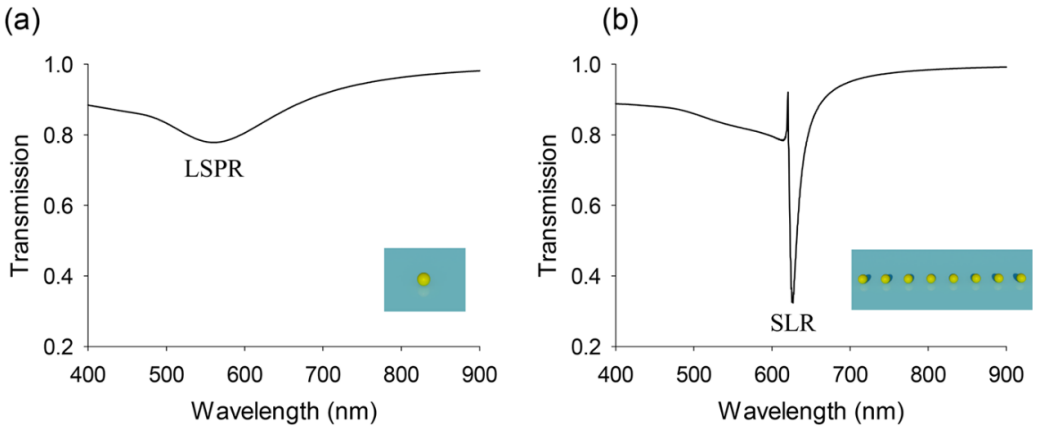

Figure 2.2: Comparison between a calculated LSPR and SLR. (a) Transmission spectrum of a single particle of radius equal to 80 nm. (b) Transmission spectrum of a 1D periodic chain of 1000 particles with a periodicity of 620 nm. Figure taken from [81].

this work and will be further detailed later.

All descriptions of LSPRs show that its spectral position depends on the particle size, shape and on the permittivity of the particle and the surrounding material, while the quality factor of the resonance mostly depends on the permittivity of the metallic particle [82]. In particular, the quality factor is inversely proportional to the imaginary part of the metallic particle. This explains why Au and Ag are good plasmonic materials in the visible and near-infrared range, where their imaginary permittivity is very small [83]. A calculated transmission spectrum of a system exhibiting a LSPR is shown in Figure 2.2(a).

2.1.4 Surface lattice resonance

When organised in a periodic array, nano-particles couple with each other through the scattered field, meaning that the field affecting a given particle of the array is the sum of the incident field and remitted fields from all other particles in the array [84]. In this picture, the entire system can be described using the coupled dipole approximation. The local field at a given particle i can be written as [85]:

$$\mathbf{E}_{i,loc} = \mathbf{E}_{i,inc} - \sum_{j \neq i} A_{ij} \mathbf{P}_j \tag{2.23}$$

With $\mathbf{E}_{i,inc}$ the incident field at the position of the dipole at position i, A_{ij} the dipole interaction matrix that takes into account the dipole-dipole interaction with the retardation due to the spacing between dipoles and $\mathbf{P}_j$ the induced dipole at position j. For an infinite array of identical particles under normal incident light, this coupled system can be analytically solved, and the polarisation for every particle can be expressed as:

$$\mathbf{P} = \alpha_{eff} \mathbf{E}_0 = \frac{\alpha_s}{1 - \alpha_s S} \mathbf{E}_0 \tag{2.24}$$

With α_s the polarisation of a single isolated particle and S the retarded dipole sum derived from the dipole interaction matrix, and of equation:

$$S = \sum_{i \neq j} e^{ikr_{ij}} \left[\frac{(1 - ikr_{ij})(3cos^2(\theta_{ij}) - 1)}{r_{ij}^3} + \frac{k^2 sin^2(\theta_{ij})}{r_{ij}} \right] \tag{2.25}$$

With k the angular wave number of the incident light, $r_{ij} = |\mathbf{r_{ij}}|$ the distance between dipole i and j and θ_{ij} the angle between the vector $\mathbf{r_{ij}}$ and the induced polarisation direction. Note that Equation 2.25 only depends on the geometry and the incident light configuration, but not on any material parameters. This enables the tailoring of resonances to specific wavelengths, enhancing the absorption and the optical response of the system at that wavelength.

Equation 2.24 provides the effective polarisability and therefore the scattering and absorption cross section, denoting the collective impact on the plasmonic resonances. An example of the extinction spectrum of such a system is shown in Figure 2.3 (a). A new resonance condition can be observed for $\Re(1/\alpha_s) = \Re(S)$, which yields a much sharper resonance near the diffraction edge of the array called surface lattice resonance (SLR), as illustrated in Figure 2.2(b). Compared to the LSPR, the absorption at the SLR wavelength is much larger due to a higher confinement of the light and increased light-matter interactions in the metal. The retarded dipole sum provides additional parameters that can be tuned to shift the resonance position and enhance the quality factor, thereby providing a sharper accessible resonance. One way to do so is by modifying the periodicity along the incident light polarisation direction to bring the diffraction

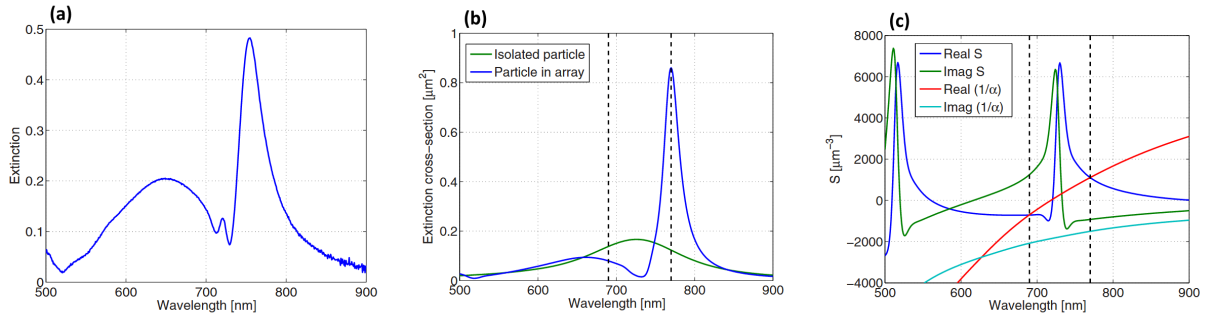

Figure 2.3: (a) Extinction spectra, (b) cross section and (c) shape factor of a periodic square array of Ag nano-disk with a diameter of 120 nm and a periodicity of 480 nm. The diffraction edge is at 727 nm. Figure taken and adapted from [86].

edge wavelength closer to the single particle resonance wavelength [87] [78]. Near the diffraction edge, the S factor's real and imaginary parts resonantly peak before dropping to almost zero. If this peak is near the isolated particle resonance, then for a specific wavelength, the real part of S and $1/\alpha$ match and a SLR is observed as shown in Figure 2.3 (b) and (c). The quality factor of these resonances is dictated by the difference in the imaginary parts of these parameters [86]. Another important factor in achieving a strong SLR is the symmetry of the surrounding dielectric environment. A mismatch between the substrate and superstrate optical index can hinder particle coupling, leading to a smaller quality factor [88][89]. This is due to the difference in the speed of light, which impacts dipolar electric coupling mediated by the scattered light propagating through these two materials.

2.2 Magneto-optics

2.2.1 Magneto-optical effects in thin films

For a plane wave propagating in free space along its wave vector $\mathbf{k}$, the electric field $\mathbf{E}$ is orthogonal to the propagation direction and is therefore in the transverse plane to $\mathbf{k}$. The polarisation of light can be represented by the complex amplitude vector $\mathbf{E}_0$ such that $\mathbf{E}(\mathbf{r},t) = \Re(\mathbf{E}_0 e^{i(\mathbf{k}\cdot\mathbf{r}-\omega t)})$ where ω is the angular frequency of the wave. Using Jones calculus formalism, the Jones vector $\mathbf{E}_0$ can be fully represented in a 2D base of the transverse plane[90] [91].The two most common bases used are the s-p base and the circular base. The s-p base is a Cartesian base defined with respect to an interface. The p vector is in the plane of incidence to that interface, and the vector s is orthogonal to the plane of incidence. The circular base is a natural coordinate system for expressing light polarisation in the context of magnetic systems [91].

The first magneto-optical effect was discovered in transparent heavy glass by Faraday in 1845 [92]. He demonstrated that a magnetic field applied along the propagation direction of light can affect the polarisation of the light when it propagates through certain materials. Later, a similar effect was discovered in reflection at the surface of a magnetic pole by Kerr [93]. He then observed this phenomenon in different geometrical configurations [94]. These effects are characterised by a rotation and a gain of ellipticity of the light's polarisation, in transmission for the Faraday effect and in reflection for the Kerr effect, when a strong magnetic field is applied or when interacting with a magnetic material.

The origin of these effects is associated with magnetic circular birefringence (MCB) and magnetic circular dichroism (MCD). Both MCB and MCD are linked to a difference in the optical indices for opposite directions of circularly-polarised light in a magnetic material or a diamagnetic material under a strong external magnetic field [73]. MCB is associated with a difference in the real part of the optical indexes, causing a difference in propagation speed through the material, which leads to a phase shift between opposite circularly-polarised light. This phase shift leads to a rotation of the light polarisation [91]. MCD, on the other hand, is associated with a difference in the imaginary part of the optical indices, causing a difference in absorption during propagation through the material thereby changing the ellipticity. At magnetic interfaces, differences in the complex optical indices cause differences in the amplitudes and phases [72] of the reflected light for opposite circular polarisation, leading to rotation and ellipticity by itself. In complex structures with multiple interfaces, such as those studied in this thesis, the observed rotation and ellipticity result from all internal reflections undergoing these effects as they propagate and are reflected or transmitted. As a result, it becomes difficult to disentangle these effects; therefore, the system must be studied as a whole.

The Kerr and Faraday magneto-optical effects are linked to complex magneto-optical material parameter Q that can be found in the expression of the permittivity of a magnetic material. In its most general form, the permittivity of such material can be written as the following tensor:

$$\epsilon = \epsilon_0 N^2 \begin{bmatrix} 1 & -iQm_z & iQm_y \\ iQm_z & 1 & -iQm_x \\ -iQm_y & iQm_x & 1 \end{bmatrix} \tag{2.26}$$

With N the complex optical index of the material, Q the complex magneto-optical material parameter, also sometimes called Voigt constant and $\mathbf{u}_M = \mathbf{M}/M_s = (m_x, m_y, m_z)$ the unitary magnetisation direction. This shape of the permittivity highlights the different possible configurations and their sensitivity to magnetisation [17].

If z is the direction normal to the sample surface and the light also propagates along z, then the electric field direction must be in the transverse xy plane $\mathbf{E} = (E_x, E_y, 0)$. This means that the electrical displacement vector in the sample $\mathbf{D} = \epsilon\mathbf{E}$ can only depend on the M_z component of the magnetisation and, therefore, the resulting light polarisation will only carry information about the magnetisation along the z direction. This configuration is known as the polar magneto-optical Kerr effect (P-MOKE). If the light shines onto the sample at an angle, the reflected light is also affected by the in-plane magnetisation. If the magnetisation is parallel to the light's

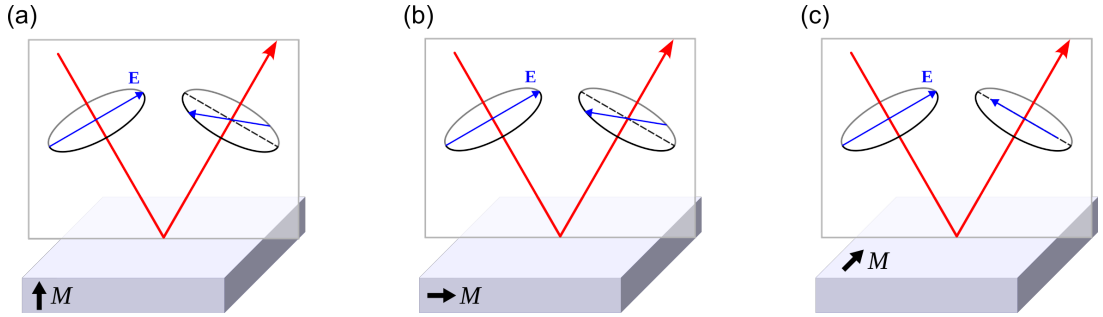

Figure 2.4: Illustration of the different MOKE configurations. (a) Polar MOKE. (b) Longitudinal MOKE. (c) Transverse MOKE.

incident plane, then the reflected light polarisation will change due to M. This configuration is called longitudinal MOKE (L-MOKE). Finally, if the magnetisation is orthogonal to the light's incident plane, then the reflected light intensity will depend on the magnetisation but not its polarisation. This configuration is called transverse MOKE (T-MOKE). These configurations are illustrated in Figure 2.4.

For a given system, the full electromagnetic solution can be derived from Maxwell equations and the optical and magneto-optical parameters of the media. This can be done for layered systems by using the transfer matrix method (TMM) which is detailed in the next chapter. Here a different approach is taken. The magnetic system is taken as a whole and only the incident, reflected and transmitted light is considered, as illustrated in Figure 2.5. Using this approach, the MCD, defined as the normalised difference of absorption between circular polarisations, can be retrieved from the measurement of the transmitted and reflected polarisation and intensities without prior knowledge of the system's optical or magneto-optical properties.

When linearly polarised light is reflected from or transmitted through a magnetised material, its polarisation will rotate and become elliptical. This change of polarisation can be described through Jones calculus formalism as a matrix multiplication of the initial polarisation $\mathbf{E}_i$ with a matrix of complex coefficients characterising the sample's effect on the polarisation:

$$\mathbf{E}_r = \begin{bmatrix} r_{pp} & r_{ps} \\ r_{sp} & r_{ss} \end{bmatrix} \times \mathbf{E}_i \tag{2.27}$$

$$\mathbf{E}_t = \begin{bmatrix} t_{pp} & t_{ps} \\ t_{sp} & t_{ss} \end{bmatrix} \times \mathbf{E}_i \tag{2.28}$$

With x_{ij} ($x \in \{r, t\}$ denoting reflection and transmission), the complex coefficient linking the j-th component of incident polarisation to the i-th component of resulting polarisation. Note, at normal incidence the coefficients are linked such that $r_{pp} = r_{ss}$ and $r_{ps} = -r_{sp}$. These matrices can be expressed in the circular base, in which case they become diagonal.

In the continuation of this work, the base in which the polarisation is expressed and the sign of the associated angle will follow Atkinson et al.'s sign convention [95]. The polarisation frame of reference is static with respect to the laboratory frame and right circular polarisation (RCP) corresponds to clockwise circularity (σ_+) associated with a positive angle for the rotation and for the ellipticity, as illustrated by Figure 2.5. In this reference, for normal-incident linearly polarised light along the p direction, the rotation θ and ellipticity η can be calculated from the Jones matrix as follows [96]:

$$\Psi_X = \frac{E_{x,s}}{E_{x,p}} = \frac{x_{sp}}{x_{pp}} \tag{2.29}$$

$$\theta_X = \frac{1}{2}\tan^{-1}\left(\frac{2\Re(\Psi_X)}{1-|\Psi_X|^2}\right) \tag{2.30}$$

$$\eta_X = \frac{1}{2}\sin^{-1}\left(\frac{2\Im(\Psi_X)}{1+|\Psi_X|^2}\right) \tag{2.31}$$

With $X \in \{K, F\}$ denoting the Kerr effect in reflection ($x = r$) and the Faraday effect in transmission ($x = t$), respectively. The sign convention of Kerr/Faraday rotation and ellipticity is illustrated in Figure 2.5. More detail on the description of the elliptical polarisation of the light can be found in Annexe B. The complex Kerr angle can be defined as:

$$\Phi_X = \theta_X + i\eta_X \tag{2.32}$$

Note that in most cases, the rotation and ellipticity are very small; thus, using the small angle approximation, Equations (2.30) and (2.31) can be simplified and:

$$\Phi_X = \Re(\Psi_X) + i\Im(\Psi_X) = \Psi_X \tag{2.33}$$

Another, more intuitive, way to define the rotation and the ellipticity can be done in the circular base. In this reference frame, E^+ and E^- correspond to the complex amplitude of the right-circular polarisation (RCP) component and left-circular polarisation (LCP) component, respectively. Then the rotation and ellipticity can be written as:

$$\theta_X = \frac{\arg(E_X^+) - \arg(E_X^-)}{2} \tag{2.34}$$

$$\eta_X = \tan^{-1}\left(\frac{|E_X^+| - |E_X^-|}{|E_X^+| + |E_X^-|}\right) \tag{2.35}$$

There is a link between the MCD and the Kerr and Faraday ellipticities. The reflection and transmission for circular polarised light can be expressed using the following equations:

$$R_\pm = R(1 \pm \tan(\eta_K))^2 \tag{2.36}$$

$$T_\pm = T(1 \pm \tan(\eta_F))^2 \tag{2.37}$$

From this, the MCD can be easily retrieved:

$$\text{MCD} = -4\,\frac{R\tan(\eta_K) + T\tan(\eta_F)}{A} \tag{2.38}$$

With R, T and A, the reflection, transmission and absorption of the sample. More detail on how this formula is related to the measured MCD can be found in Annexe B. This relation was verified and confirmed using the transfer matrix method and experimental measurements described in the next chapters.

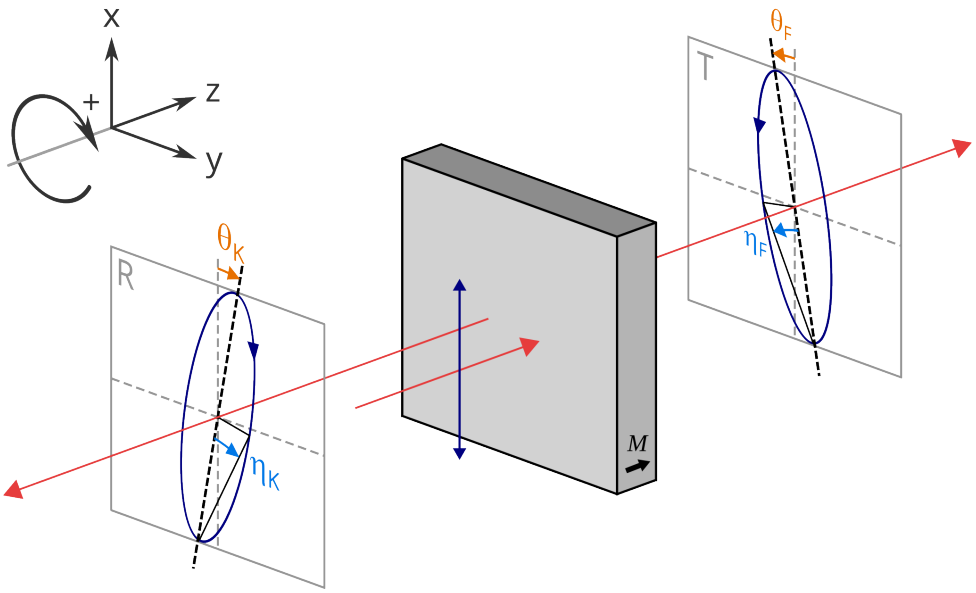

Figure 2.5: Illustration of Kerr and Faraday rotation and ellipticity. The frame of reference is fixed for both transmission and reflection. The angles are taken positive clockwise when looking along the z-axis.

2.2.2 Magneto-optical effects in plasmonic systems

In 1999, Kravets et al. observed a large enhancement of the Faraday rotation in CoFe-HfO_2 granular media and associated it to the surface plasmon resonance of the system. The existence of surface plasmon resonances in magneto-plasmonic systems was experimentally confirmed by Chen et al. through near-field microscopy [97]. In systems that exhibit resonances, rotation and ellipticity will be affected by the resonance.

As described in Sections 2.1.3 and 2.1.4, plasmonic resonances come from the effective polarisability of the particle. Around the resonance frequency, the induced dipole described by the polarisability shows a peak in amplitude and a phase jump, as illustrated in Figure 2.6. This phase change can be understood as the system transitioning from being fast enough to follow the excitation and remain in phase with it, to a situation where it lags behind the excitation.

The nano-structures studied in this thesis are nano-disks with out-of-plane magnetisation. In this case, the permittivity of the structure can be expressed in the circular base along the out-of-plane axis. In that base, the permittivity is diagonal, with different values for left and right circular polarisations. For symmetry reasons, taking opposite magnetisation direction is identical to exchanging the circular polarisation directions.

The difference in effective permittivity for opposite polarisation can be understood to originate from a constants Lorentz force acting on the forced circular motion of electrons. This force will reduce/increase the radius of the electron orbital motion, thereby blue/red shifting its resonance frequency by an amount given by the so called cyclotron frequency [98] $\omega_C = e\frac{B}{m_e}$.

The light induced circular motion of electron can be retrieved through the expression of the polarisability tensor in the circular base. The induced dipoles or circular motion will re-emit and contribute to the polarisation of the transmitted and reflected light. Linear polarised light, being the superposition of a left and a right circular polarisation with identical amplitude and phase, will excite both of these circular modes. The phase and amplitude of these re-emitting modes result in the rotation and ellipticity of the reflected and transmitted polarisation, as described by Equations 2.34 and 2.35. The shift in resonance frequencies will lead to different behaviour for the rotation and ellipticity. The ellipticity spectrum, characterised by the difference in the

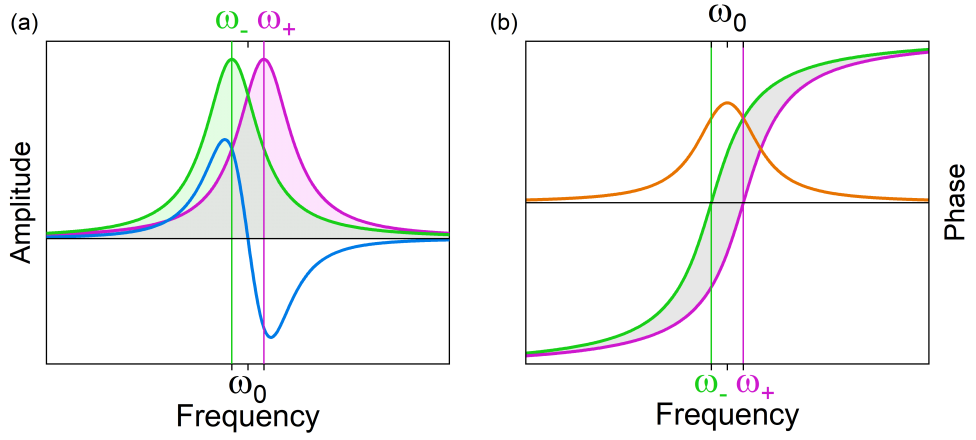

Figure 2.6: Illustration of the rotation (orange line) and ellipticity (blue line) at resonance coming from the difference in amplitudes (a) and phases (b) of the induced dipoles for opposite circular polarisation. ω_-, ω_+ and ω_0 denote the resonance frequency of circular left, circular right and linear polarisation, respectively.

circular mode amplitude spectra, will cross zero at the resonance frequency and change sign, as illustrated in Figure 2.6 (a). The rotation spectrum, on the other hand, is the difference between the phase spectra of the two circular modes. The rotation peaks at the resonance frequency as shown in Figure 2.6 (b). These behaviours were further studied and measured by Maccaferri et al. in non-interacting, randomly distributed Ni elliptical nano-disks [99] [100] as shown in Figure 2.7. They demonstrated that these magneto-plasmonic systems can be modelled as two damped oscillators coupled via spin-orbit coupling. This model was later extended by Kataja et al. to SLRs in periodic rectangular arrays by considering an additional radiative coupling between the particles [101].

In particular, Freire-Fernández et al. studied the SLRs in periodic arrays of Co/Pt multilayer nanodisks, a system very similar to the one investigated in this thesis [102]. They optimised the geometry and showed, at an equal filling factor, a sixfold enhancement of the measured Kerr angle at the SLR wavelength compared to the full film.

MCD, being linked to the Kerr and Faraday ellipticities through Equation 2.38, will have a similar behaviour: crossing zero and changing sign near the resonance frequency. This phenomenon has been shown in periodic and randomly distributed Ni nano-disks by Kataja et al. through the measurement of the extinction and MCD spectra [103].

The IFE, on the other hand, is related to the rotation through the magneto-optical susceptibility of the material. Furthermore, the confinement of the electric field by the plasmonic system at the resonance enhances the $E \times E^*$ component in the IFE formula. The overall effect should reach a maximum at the resonance frequency. No change in the sign of the effect is expected in the plasmonic structures studied in this work.

Magnetic materials are typically poor plasmonic materials due to their high loss, resulting in weak and broad resonances. To enhance the impact of plasmonic resonances on magneto-optics, hybrid systems composed of noble and magnetic metals have been studied. González-Díaz et al. showed this concept by fabricating Au/Co/Au nano-particles and studying the impact of the fraction of Co on the MO response [104] [105]. They demonstrated the trade-off between the resonance quality and the MO response. They also observed a change in the spectral behaviour of the Kerr rotation and ellipticity depending on the fraction of Co in the particle. The ellipticity

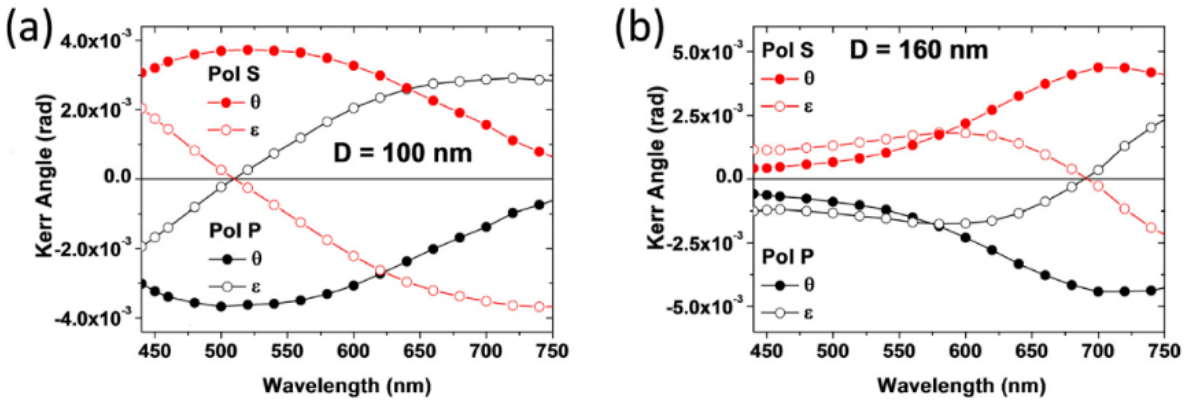

Figure 2.7: P-MOKE rotation (filled symbols) and ellipticity (open symbols) spectra of randomly distributed Ni nano-disks of diameter (a) 100 nm and (b) 160 nm. The measurements were performed for two orthogonal polarisations, Pol S (red) and Pol P (black). Figure taken from [99].

spectra transition from bipolar crossing zero at the resonance frequency to unipolar peaking at the resonance frequency. They explain this by the existence of two types of transitions at the origin of the MO activity: the paramagnetic and diamagnetic transitions, associated with the real and imaginary parts of the off-diagonal terms of the permittivity. In non-magnetic material, the latter dominates and leads to a zero crossing of the ellipticity. In magnetic materials, both contributions exist, leading to a difference in amplitude and a shift in frequency for opposite circular polarisations, as described before. If the real part dominates, then the frequency shift is negligible compared to the amplitude difference, resulting in a peak in the ellipticity spectrum at the resonance. This explains the sometimes observed shift of the zero crossing of the ellipticity compared to the plasmonic resonance.

2.2.3 Magnetisation control with plasmonics

In this final section of this chapter, some previous works featuring the control of magnetism through plasmonics are reviewed. Control of magnetisation in magneto-plasmonic systems can be achieved through demagnetisation or AO-HIS. Since both effects have a thermal origin, the enhancement of the optical absorption and the confinement of the electric field by plasmonic structures at the resonance wavelength lead to lower threshold laser fluences and smaller affected areas.

Cheng et al. demonstrated a reduction in the threshold fluence required to locally demagnetise a Co/Pt multilayer by using Au nanoparticles on top of a SiO_2 buffer layer [106]. Through transmittance spectra measurements, they observed the LSPR associated with the isolated response of the particles. At this wavelength, they observed a lower threshold fluence compared to wavelengths away from the resonance. They attributed this difference to an enhancement of the electric field due to confinement, resulting in greater absorption.

Liu et al. demonstrated single-shot toggle switching in TbFeCo at a nano-metric size with the use of Au plasmonic antenna placed on top of an SiN buffer layer [12]. They showed that the switching threshold laser fluence is reduced around plasmonic antennas compared to regions without antennas. They corroborated their experimental results with calculations of the near field, showing an enhancement of the electric field near the antenna due to its confinement.

Verges et al. studied the behaviour of AO-HIS in different periodic nanodisk arrays made of Co/Gd/Pt multilayers [11]. They showed lower switching fluence thresholds at the SLR compared to that of the full film. They demonstrated that the threshold fluence spectra are correlated to the extinction spectra of the array as shown in Figure 2.8, highlighting the thermal origin of AO-HIS. They also observed a modulation of the magneto-optical contrast around the resonance. Finally, they reported that, at the plasmonic resonance, up to a 17-fold enhancement in readout sensitivity can be achieved over an equivalent full film. This enhancement value is obtained after scaling the magneto-optical responses with the array filling factor, to take into account differing amounts of magnetic material in the array and the film.

Recently, Pezeshki et al. proposed the integration of plasmonic nanoantennas into photonic devices to enable all-optical writing and reading of magnetic racetrack memory [108]. Their proposed system utilises gold antennas and photonic cavity solutions. Simulations show that the resulting confinement and enhancement of the electric field and absorption in the magnetic track significantly reduce the switching energy. Confinement of the electromagnetic fields, due to plasmonic effects, allows for the reading of magnetic domains as small as 100 x 100 nm^2.

Another original way to use plasmonics to control magnetic systems was demonstrated by Ignatyeva et al. In their work, they demonstrate a way to selectively excite SPP in two distinct GdFeCo layers separated and encapsulated in Si_3N_4 [109]. Using the prism coupling technique

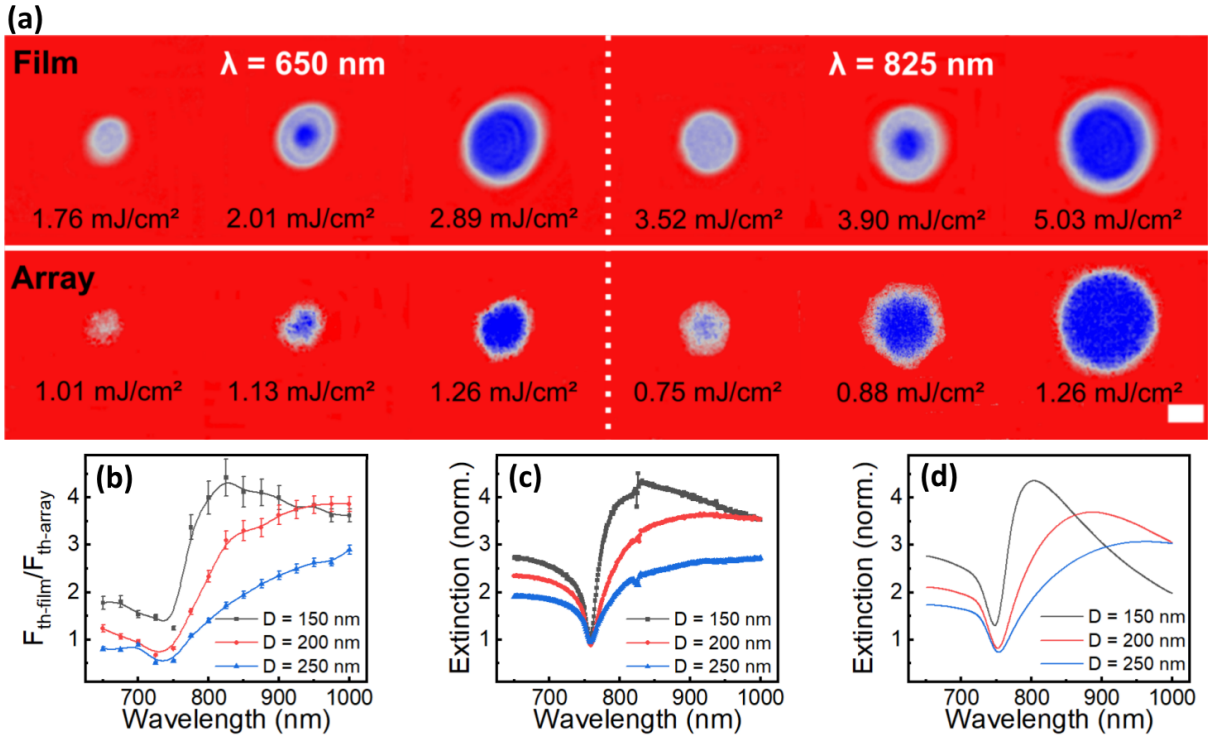

Figure 2.8: (a) MOKE images of final magnetisation states after single-shot AO-HIS in a $[Co/Gd/Pt]_2$ film (top) and a $[Co/Gd/Pt]_2$ nanodisk array with period P = 500 nm and disk diameter D = 150 nm (bottom). Results are shown for a wavelength of 650 nm (left) and 825 nm (right). (b) Ratio of the AO-HIS threshold fluence for the film and the plasmonic array. (c) Extinction spectra scaled by their filling factor and normalised by the full film extinction spectrum. (d) Simulated normalised extinction spectra. Figure taken and adapted from [107].

and depending on the polarisation direction (s or p), they can couple to SPPs of different amplitudes in both layers, resulting in higher absorption in one of the films and, in turn, leading to a lower OA-HIS threshold for that layer. In this manner, the magnetic layers can be addressed and switched independently or simultaneously at higher fluence.

Studies of AO-HDS in plasmonic systems are scarce, with most works being theoretical or simulation studies on the enhancement of IFE in plasmonic structures.

Using quantum hydrodynamic, Hurst et al. simulated the circular motion of electrons in an Au nanoparticle induced by circularly polarised light [110]. They showed that these modes can be associated with a circular current, which in turn generates magnetisation. They associated this phenomenon to the inverse Faraday effect. They also showed that the maximum intensity of this induced magnetisation is reached at the LSPR of the particle. This is in agreement with the expected behaviour described in the previous section.

Chang et al. further studied the plasmonic-induced inverse Faraday effect by simulating a Co/Pt multilayer film capped with SiO_2 and featuring a periodic square array of Au nanodisks on top [111]. The electromagnetic field of the system under circular light excitation was simulated using COMSOL Multiphysics®. They used the resulting electric field distribution to calculate the IFE-induced effective magnetic field. Using the two-temperature model, they also calculated the temperature transients in the magnetic layer. Finally, importing all these

elements into a micromagnetic Monte Carlo simulation allowed them to study the stochastic behaviour of AO-HDS. In this way, they were able to reproduce the multi-shot switching and thermal demagnetisation characteristic of AO-HDS as seen in Figure 2.9.

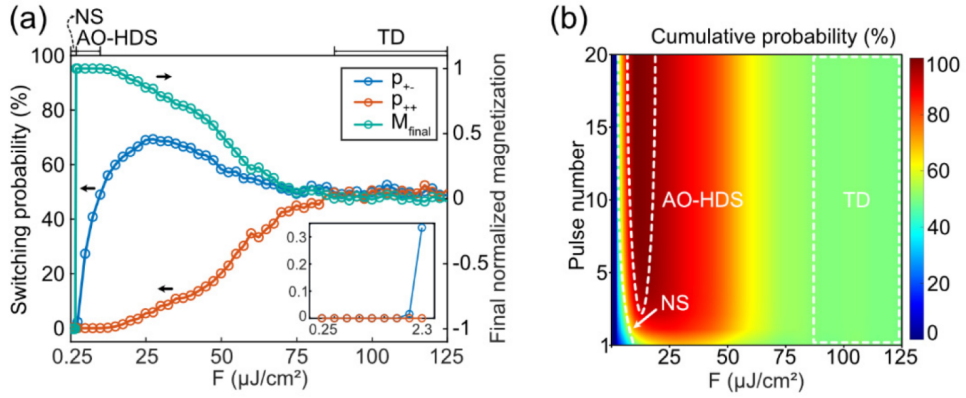

Figure 2.9: Monte Carlo simulation results of AO-HDS in a Co/Pt film coupled with a plasmonic system. (a) Switching probability and normalised final magnetisation state as a function of laser fluence. The insert is a zoomed-in plot near the switching threshold. (b) Cumulative switching probability as a function of laser fluence and pulse number. NS, AO-HDS, and TD stand for no switching, all-optical helicity-dependent switching, and thermal demagnetisation, respectively. Figure taken from [111].

Kataja et al. studied the behaviour of Ni nanoparticle arrays under high fluence femtosecond laser pulses at the resonance wavelength [112]. Using multiple circularly polarised laser pulses, they did not observe AO-HDS. Instead, they observed demagnetisation, similar to that induced by linearly polarised light. Nevertheless, they demonstrated a lower threshold fluence for demagnetisation and field-assisted magnetisation switching at the resonance wavelength, where the extinction reaches its maximum.

As shown in previous works, plasmonic systems are a promising platform for studying and controlling magnetisation. Plasmonic devices have the ability to confine electromagnetic fields at sub-wavelength scales and, in consequence, enhance light-matter interactions. They also allow the adjustment and enhancement of the underlying mechanism behind all optical switching through the tailoring of plasmonic resonances. The work presented in this thesis aims at identifying the mechanism behind AO-HDS through the design of plasmonic resonances that generate distinctive spectral IFE and MCD responses. The fabrication processes, characterisation methods and measurement techniques used in this study are introduced in the next chapter.

Chapter 3

Methodology

In this chapter, the various processes, measurement methods, simulations and analyses used during this project are presented. In the first part, sample preparation will be covered, followed by the method for their characterisation and simulation. Finally, a general introduction to the all-optical switching setup is given, and the developed measurement processes are presented.

3.1 Sample fabrication

All studies reported in this thesis rely on the growth of high-quality magnetic thin films on substrates. This is done through DC magnetron sputtering by Michel Hehn [1]. Magnetron sputtering is a physical vapour deposition (PVD) technique that involves bombarding a target with a highly energetic ionised plasma. This causes the release of atoms from the target, which will then redeposit themselves on the sample facing the target. Some magnets are added beneath the target to confine the plasma, resulting in higher and better-controlled deposition rates. Sputtering is also used to cap the final sample with SiO_2; however, in this case, the RF sputtering technique is employed.

For full film samples, no additional fabrication steps are required; however, some samples are patterned into plasmonic devices. Before nano-fabrication, the full film's magnetic properties are characterised using a magneto-optical Kerr effect (MOKE) magnetometer. This technique will be described later.

A top-down approach has been employed to pattern the sample. This means that the pattern is etched into an already deposited full film, rather than the material being deposited after patterning, as it is the case with a lift-off approach. The patterned structures have sizes of around 100 nm. This size is below the resolution of the mask based UV lithography machine accessible for this project. Therefore, electron beam lithography (EBL) is used instead. Electron beam lithography is a maskless patterning technique that uses electro-sensitive resist coated onto the sample and a sweeping, focused beam of accelerated electrons to modify the chemical properties of the resist locally. Depending on the resist, this technique can have a resolution down to 10 nm. Two types of resist exist: positive and negative resist, depending on whether exposure to the electron beam makes it more or less soluble in a specific solvent called a developer. In the case of positive resist, the exposed region is more soluble in the developer, meaning that for a well-chosen development time, the exposed resist will be removed while the unaffected regions will remain. For negative resist, the process is reversed: the exposed resist is less soluble and therefore remains after development. For this project, a negative etch-resistant resist (Micro Resist Technology ma-N 2403) is used. After sample cleaning, the resist is spin-coated onto the full film and then baked on a hot plate. Spin coating allows for the deposition of a uniform layer of resist over the sample. The thickness of the resist can be controlled by adjusting its viscosity and the speed and acceleration of the spin-coater.

Next, the samples are loaded into the EBL machine, making sure that the sample holder makes a good electrical contact with the deposited metallic film. If the deposited film is not conductive, or in the case of patterning onto an electrically isolating substrate, an additional conductive coating needs to be deposited on top of the resist to avoid charge accumulation. A stage precisely moves the sample to align the write field with the desired region of the sample. The electron beam current is controlled using an aperture, and it is measured to calculate the exposure time required to obtain the desired dose. The beam is swept using deflectors and a beam blanker to draw the pattern within the write field. To avoid stitching issues, the entire pattern is kept within the boundary of a single writing field. In this thesis, a writing field of 500 µm x 500 µm is used to pattern array patches of identical size. The required dose depends on the resist and will affect the development time. A dose that is too high will broaden the features, while too small of a dose will results in the features being dissolved by the developer making then smaller or even disappear. Dose tests are done to optimise the dose and development time

[1] Spintronics and Nanomagnetism group, Physics of Matter and Material department, Université de Lorraine, CNRS, Institut Jean Lamour, Nancy F-54000, France

(Microposit MF-319 developer) as the dose slightly depends on the size of the structures.

After development, the patterns are transferred to the films by etching. The remaining resist acting as a mask protecting the regions that constitute the structure from being etched. To achieve this, ion beam etching (IBE) is employed. Ion beam etching is a dry etching technique in which the sample is exposed to a highly energetic beam of atoms to physically expel material from its surface. The atoms ejected from the sample can be collected and analysed by spectroscopy to follow the etching process and stop it when the substrate is reached. Etching is performed at a slight angle, and the sample holder is in constant rotation to etch the redeposition on the sides of the resist.

During the etching process, not all of the resist is etched away, so a removal step is required. This type of resist hardens to gain etch resistance. To remove the hardened resist, both a chemical remover and plasma ashing are used a few times. The samples are left for several hours in the heated remover (Microposit Remover 1165) while applying some ultrasound. In addition, the samples underwent O_2 plasma ashing, meaning exposing the sample to an oxygen plasma that reacts with the resist, turning it into ash. This process, while removing most of the resist, leaves behind some residues between the structures. To dispose of these residues, the samples are cleaned with a weakly concentrated alkaline detergent (RBS 2%) while applying some ultrasound. The progress of resist removal is monitored using atomic force microscopy (AFM). AFM measurements of the final structures are shown in Annexe A.

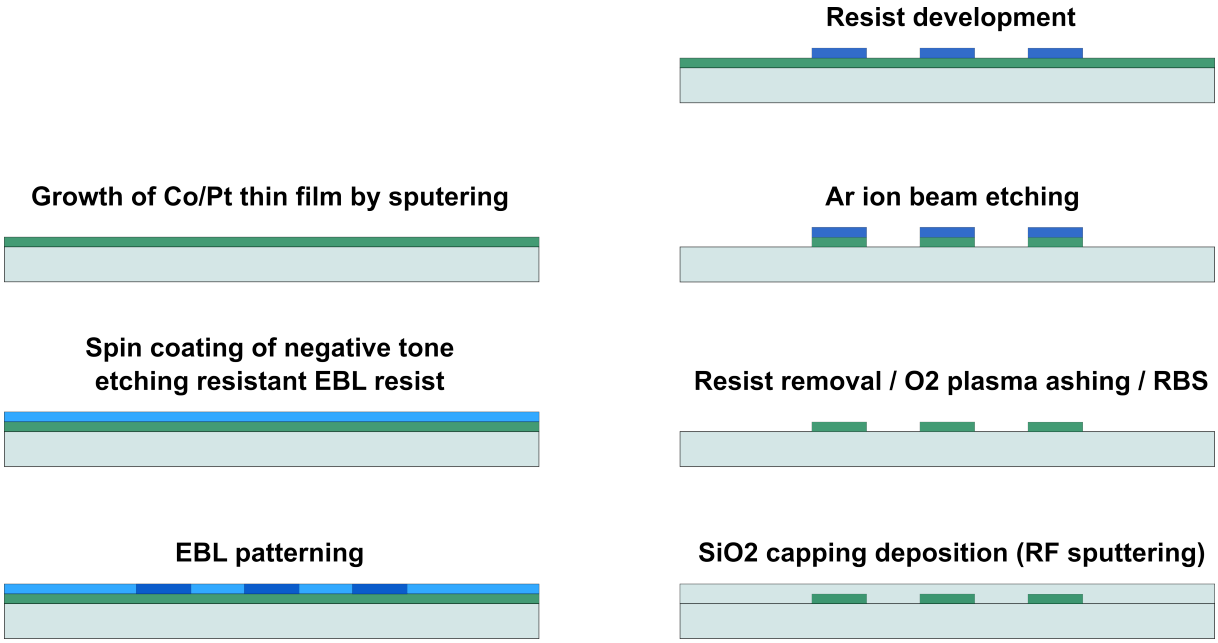

Figure 3.1: Schematic of the nanofabrication process.

As described in the previous chapter, to obtain a sharp SLR, the periodic arrays need to be embedded into an optically homogeneous media. Therefore, Some samples are capped with 200 nm of SiO_2 using RF sputtering. The refractive indices of the capping layer and substrate were measured by Thomas Easwarakhanthan [2] and the sputtering parameters were tuned by Laurent Badie [3], to match the index refractive of the capping layer to that of the substrate.

[2]Nanomaterials for Optoelectronics group, Physics of Matter and Material department, Université de Lorraine, CNRS, Institut Jean Lamour, Nancy F-54000, France

[3]Centre de Compétences Micro et Nanotechnologies, Université de Lorraine, CNRS, Institut Jean Lamour,

An overview of the nanofabrication steps is given in Figure 3.1, and the parameters used in the different nanofabrication steps are compiled into the following table:

Spincoating (ma-N 2403)	Speed	: 6000 rpm
	Acceleration	: 6000 rpm/s
	Time	: 60 s
Baking (hotplate)	Temperature	: 90°C
	Time	: 60 s
EBL	Voltage	: 20 kV
	Aperture	: 7.5 µm
	Current	: 13.21 pA
	Writing field	: 500 µm x 500 µm
	Step size	: 7.8 nm
	Dose	: 100 →150 µC/cm^2
Developement (MF-319)	Time	: 50 s
	Rinsing	: deionised water
Etching (Ar IBE)	Rotation	: yes
	Etching angle	: 10°
	Beam voltage	: 200 V
Removal (remover 1165)	Ultrasound	: yes
	Temperature	: 80°C
	Time	: ∼ 10 h
	Rinsing	: isopropanol
Plasma ashing (O_2)	Power	: 150 W
	Time	: 240 s
Cleaning (RBS 2%)	Ultrasound	: yes
	Time	: 300 s
	Rinsing	: deionised water
Sputtering (SiO_2)	Process gas	: Ar/O_2
	Source	: RF
	Power	: 200 W
	Pressure	: 6E-3 mbar
	Duration	: 1400 cycles

3.2 Sample characterisation

The samples are characterised at different stages of the fabrication process. The out-of-plane hysteresis loops of the thin films are measured before nanofabrication to check for out-of-plane anisotropy. The measurements are performed using a magneto-optical Kerr effect (MOKE) magnetometer. After nanofabrication, the samples' optical and magneto-optical spectra are measured on a dedicated setup at Aalto University.

3.2.1 Magneto-optical Kerr effect magnetometer

As described in Section 2.2, when linearly polarised light reflects from or is transmitted through a magnetic material, the light polarisation rotates and becomes elliptical. This can be used to

Nancy F-54000, France

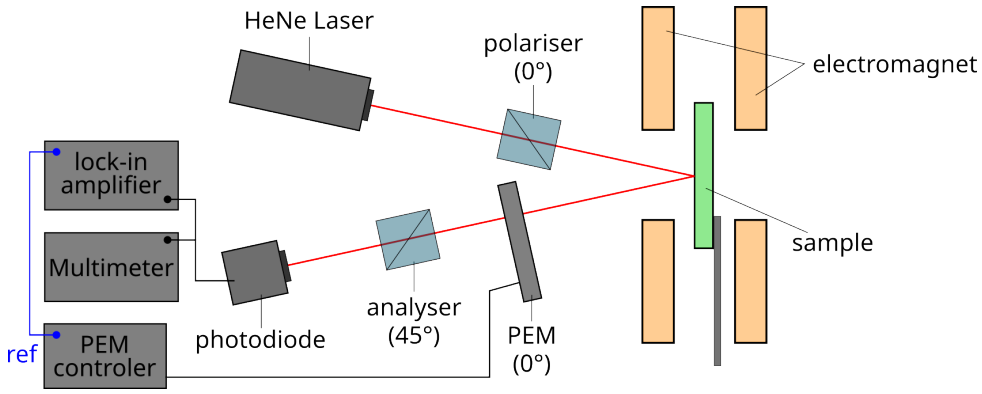

Figure 3.2: Schematic of the MOKE magnetometer setup.

probe the direction of magnetisation, as opposite magnetisation directions yield opposite signs of the rotation and ellipticity.

To obtain quantitative measurements of the rotation, the lock-in detection method is utilised. This technique relies on the modulation of the reflected light polarisation components using a photoelastic modulator (PEM). A PEM is a wave plate whose retardance can be controlled and modulated at a fixed frequency. This means that the speed of light, that is linearly polarised along its active optical axis, can be modulated. This induces a phase difference between the orthogonal polarisation components of light. The polarisation of the light transmitted through the PEM is modulated depending on the retardance modulation amplitude and the relative angle between the PEM axis and the light polarisation direction.

The magnetometer is used in polar MOKE configuration, the incidence beam is at near to normal incidence to the sample surface. This configuration provides the close to the maximum out-of-plane magnetisation sensitivity. A continuous-wave HeNe laser with a wavelength of 633 nm is used as the source. The emitted light is linearly polarised by a Glan-Taylor polariser and reflected on the sample at near normal incidence through the pole of an electromagnet. The reflected beam goes through the PEM set at a 0° angle with respect to the polariser. The polarisation is projected along an axis by a second polariser set at 45° to the PEM axis. The intensity of the resulting beam is measured using a fast photodiode. The ensuing signal and the modulation reference signal from the PEM are fed to a lock-in amplifier, which retrieves the amplitude of the different harmonic components of the signal. The average DC signal is also measured in parallel with a multimeter. A schematic of the setup is provided in Figure 3.2.

By using the Jones matrices formalism to calculate the effect of each optical element on the polarisation, the intensity measured by the photodiode is obtained [113]:

$$I_{\mathrm{R}} \simeq I_{\mathrm{DC}}[1 + 2\theta_K J_0(\rho_0) - 4\eta_K J_1(\rho_0)\sin(\omega t) + 4\theta J_2(\rho_0)\cos(2\omega t) + ...] \tag{3.1}$$

With I_{DC} the average intensity, θ_K and η_K the Kerr rotation and ellipticity respectively, J_n the first kind Bessel function of order n, ρ_0 and ω the retardance modulation amplitude and frequency, respectively. Higher orders of the decomposition into Bessel functions are not considered, as both the rotation and ellipticity can be retrieved from the two first order and the higher orders can be filtered out by the lock-in. For a well-chosen retardance modulation amplitude: $\rho_0 = 2.405$ rad $= 0.383$ wave, the zero-th order Bessel function is equal to zero. In this case, the rotation and ellipticity can be retrieved:

$$\theta_K = \frac{\sqrt{2}}{4J_2(\rho_0)} \frac{V_{2\omega}}{V_{\mathrm{DC}}} \tag{3.2}$$

$$\eta_K = \frac{\sqrt{2}}{4J_1(\rho_0)} \frac{V_{\omega}}{V_{\mathrm{DC}}} \tag{3.3}$$

With V_{DC}, V_ω and $V_{2\omega}$, the DC voltage measured by the multimeter and the rms voltages for the first and second harmonic components of the signal measured by the lock-in. More detailed calculations describing this measurement can be found in Annexe B.

Out-of-plane magnetic hysteresis curves are recorded by sweeping the applied magnetic field while measuring the rotation and/or ellipticity. From the shape of the loop, information about the sample's anisotropy can be extracted. Note that this technique does not provide an absolute measurement of saturation magnetisation M_s, unlike SQUID magnetometers or vibrating sample magnetometers (VSM). On the other hand, MOKE magnetometers offer several advantages over other methods, including speed, the ability to probe magnetisation locally, and the possibility of adjusting the wavelength of light to modify sensitivity to different elements.

3.2.2 Optical spectrometer

To study the plasmonic response of magnetic nanodisk arrays, optical transmission and reflection spectra are measured at near-normal incidence. These data are subsequently used to determine absorption spectra.

A continuous white light laser with an acousto-optic tunable filter (AOTF) is used to sweep the wavelength of the incident beam. The tunable filter has two outputs (450-830 nm and 830-1400 nm). Depending on the wavelength, a flipper mirror is used to select which output beam is sent and focused onto the sample. An additional flipper mirror and CCD camera are placed into the reflected light path to help position the beam onto the structures. The intensity of the reflected and transmitted beams is measured with a pair of photodiodes as shown in Figure 3.3.

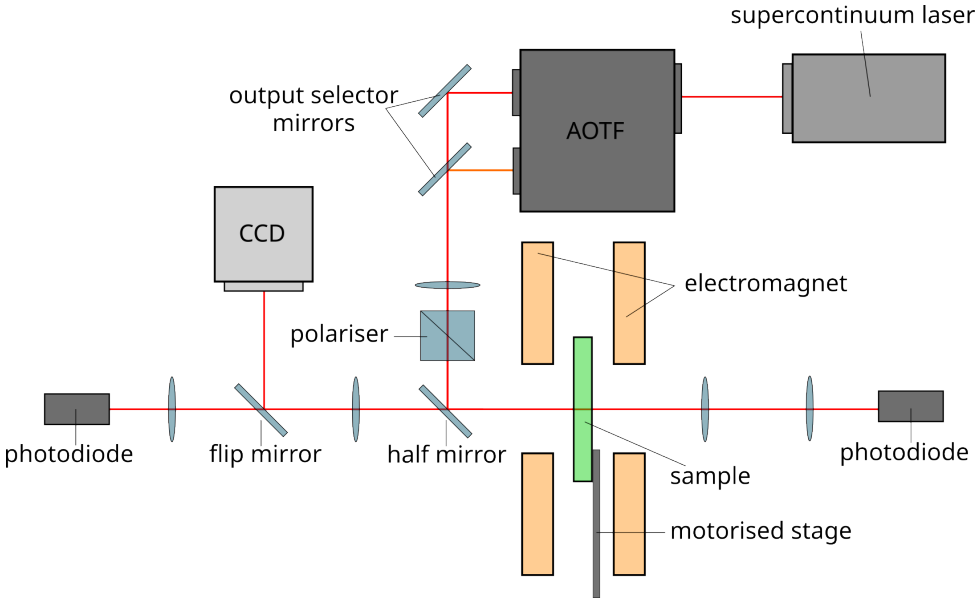

Figure 3.3: Schematic of the optical spectrometer.

To remove the environment contribution to the signal, the dark currents for both diodes are measured and subtracted from their corresponding signals. For every structure, three measurements are performed: one on the plasmonic structure, one on the substrate and one without the sample (only in transmission). From the last two measurements, and assuming no absorption in the glass substrate, the transmittance and reflectance of the glass are retrieved. They are used to normalise the signal of the structure with the substrate reference. This allows the removal of the spectrum of the filtered laser source from the signals and to properly normalises them. The final transmission and reflection spectra are calculated using the following formulas:

$$T = \frac{T_s}{T_{sub}} \frac{T_{sub}}{T_0} = \frac{T_s}{T_0} \tag{3.4}$$

$$R = \frac{R_s}{R_{sub}} (1 - \frac{T_{sub}}{T_0}) \tag{3.5}$$

With R_i and T_i being the signals in reflection and transmission, after subtracting the associated dark current. The indices s, sub, and 0 correspond to the signal on the structure, on the substrate, and without a sample, respectively.

For a periodic structure, below a specific wavelength, some diffracted beams can be observed in both reflection and transmission. Those beams are not collected and therefore not measured by this setup. At these wavelengths, the calculated absorption from the measurements will differ from the actual absorption.

3.2.3 Magneto-optical spectrometer

To be able to measure the Kerr/Faraday rotation and ellipticity spectra the previous optical setup is modified. The output of the AOTF is polarised using a Glan-Taylor polariser. For the transmitted and reflected beam paths, a PEM set at a 0° angle with respect to the polariser and an analyser set at 45° to the PEM axis are added. The retardance modulation amplitude of the PEMs is set to $\rho_0 = 2.405$ rad $= 0.383$ wave. The beam intensity is then measured using two fast photodiodes. Four lock-ins are used, two for each photodiode, to measure both

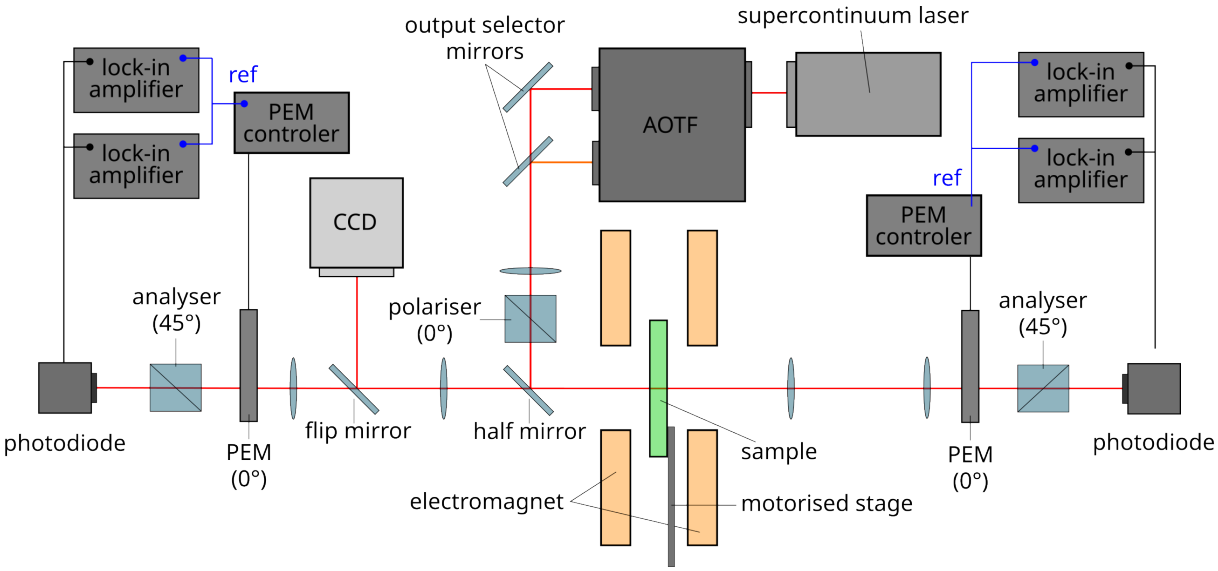

Figure 3.4: Schematic of the magneto-optical spectrometer.

rotation and ellipticity simultaneously. The probe beam is focused down to fit on the patches of magneto-plasmonic structures fully. A simplified schematic of the setup is shown in Figure 3.4.

Equations 3.2 and 3.3 are used to calculate the Kerr and the Faraday rotation and ellipticity. The details of the calculations for this setup and the used approximations can be found in Annexe B. For each wavelength, the magnetic field is swept to record complete hysteresis loops. Each loop is processed to centre them and to correct for possible slopes coming from high-field paramagnetic and/or diamagnetic contributions. The magneto-optical response at that wavelength is taken as half the signal between the two saturated states.

3.2.4 Magnetic circular dichroism spectrometer

Magnetic circular dichroism spectra are measured by modifying the previous magneto-optical setup. The output of the AOTF is polarised using a Glan-Taylor polariser. The beam then go thought a single PEM with axis at a 45° angle to the polariser axis, before being focused on the structures. The retardance modulation amplitude of the PEM is set to $\rho_0 = 1.571$ rad $= 0.25$ wave. The transmitted and reflected beam intensities are then measured using two fast photodiodes. This configuration of the setup is illustrated in Figure 3.5.

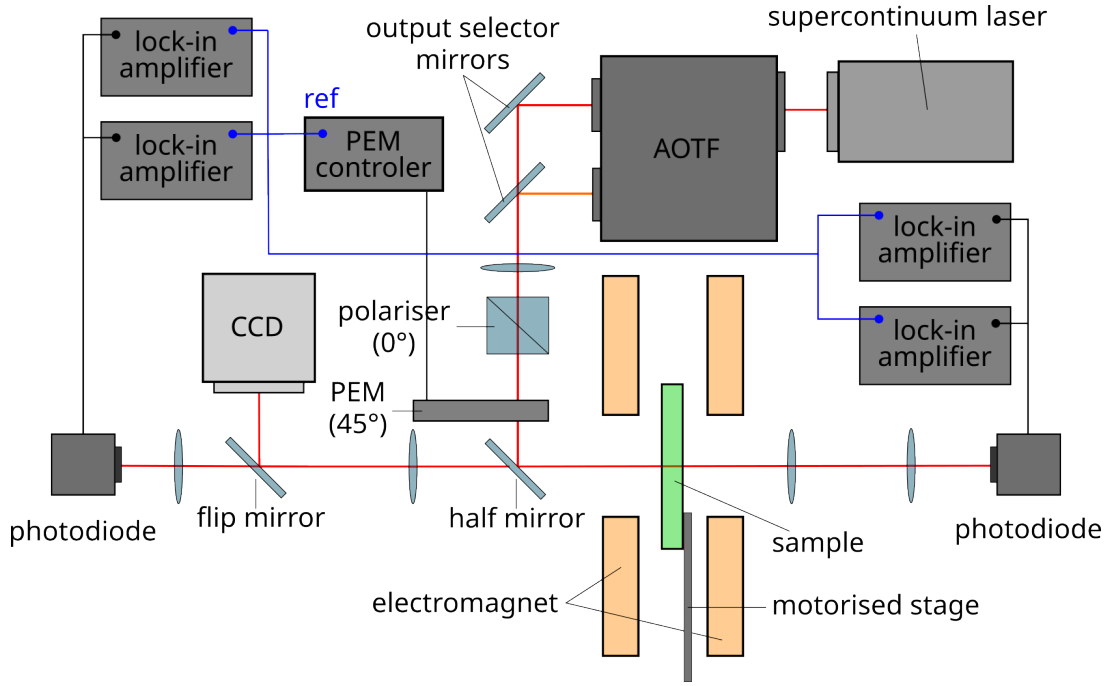

Figure 3.5: Schematic of the MCD spectrometer.

The lock-ins are set to retrieve the DC and first harmonic component of the signal. In this configuration, the PEM acts as a oscillating quarter-wave plate, modulating the light polarisation between opposite circular polarisations. The difference in transmission (T) and reflection (R) can then be obtained through the following relations:

$$\frac{\Delta T}{T} = \sqrt{2}\frac{V_{T,\omega}}{V_{\mathrm{T,DC}}} \tag{3.6}$$

$$\frac{\Delta R}{R} = \sqrt{2}\frac{V_{R,\omega}}{V_{\mathrm{R,DC}}} \tag{3.7}$$

The MCD, defined as the normalised difference in absorption between opposite circular polarisation can then be calculated from these measurements and the optical measurements:

$$\mathrm{MCD} = \frac{\Delta A}{A} = -\frac{T\frac{\Delta T}{T} + R\frac{\Delta R}{R}}{1 - T - R} \tag{3.8}$$

The details of the calculations for this setup and the used approximations can be found in Annexe B.

3.3 Simulations

3.3.1 Transfer Matrix method

The transfer matrix method (TMM) is a numerical technique that allows the calculation of the propagation of electromagnetic waves in stratified media. In its simplest form, the 2x2 TMM only consider two waves, one propagating forward and the other one backwards. This approach does not take into account any changes to the polarisation of the light. To do so, two waves in both directions are needed to create a base in which the polarisation can be expressed. This is the case for the 4x4 TMM, where the polarisation is usually decomposed into the s and p base.

To simulate the MO response and to fit the measured signal, an open-source Python toolkit called *PyLlama* [114] is used and built upon. *PyLlama* implements the 4x4 TMM formalism and provides a framework to define structures and layers described by arbitrary full 3x3 permittivity matrices. Magneto-optical systems are not directly implemented but can be described as a material with a specific permittivity matrix. The code provides as output the full reflectance and transmittance of the system, as well as the reflection and transmission Fresnel matrix, which includes all the information about the polarisation of the reflected and transmitted light. From this, the Kerr/Faraday rotation and ellipticity can be calculated.

An interface to implement magneto-optical systems was developed. Code snippets of this interface implementation and an example can be found in Annexe C. It consists of a way to import tabulated optical indexes and Voigt constants and to automatically calculate the permittivity matrix depending on the wavelength and magnetisation direction. An easy way to describe stacks composed of magnetic layers is also integrated. Finally, a function taking the output of the *PyLlama* simulation and calculating the rotation and ellipticity is added. The interface is benchmarked against results from literature [115] [116], yielding identical results (see Figure C.1 in Annexe C).

3.3.2 Comsol simulations

To study and optimise the optical and magneto-optical behaviour of the magneto-plasmonic structures, finite elements method (FEM) simulations are performed using the Wave Optics Module of COMSOL Multiphysics® [117][118]. Two types of structures are considered: periodic square arrays of nano-disks or a single isolated nano-disk.

In the case of the periodic square arrays, Floquet periodic boundary conditions are used to emulate an infinite array of nano-disks while limiting the simulation size. This also allows the definition of a periodic port to excite and analyse the plane wave modes of the model. Furthermore, periodic ports can extract the different diffraction orders that may arise due to the periodic nature of the studied structures, as illustrated in Figure 3.6 (a).

The magnetic material that constitutes the nano disks is defined by a full 3x3 complex tensor for its permittivity. This allows the consideration of the magneto-optical interaction occurring in

the studied systems. The off-diagonal terms in the permittivity are set using the complex Voigh constant Q and depend on the magnetisation direction. The method to obtain the optical and magneto-optical constants used in these simulations can be found in Chapter 4.

The randomly distributed disks are simulated using the scattered field formulation [118][119], taking an analytical plane wave solution as background field [120] as illustrated in Figure 3.6 (c). The simulated area is surrounded by perfectly matched layers (PML) that will emulate an infinite non-reflective medium [121][118]. In this case, only the absorption spectrum and near-field distribution can be easily accessed. For the absorption, the total power dissipation density can be integrated over the particle volume, then normalised by the incident intensity divided by the particle area density (number of disks per surface area).

Linear and circular polarisations are used to excite the systems. Opposite circular polarisation directions and/or the opposite magnetisation directions are simulated to fully characterise the magneto-optical response. In the case of periodic structure, the transmitted, reflected, and absorption spectra can be directly accessed in COMSOL if the diffracted orders are correctly taken into account. Furthermore, the transmitted and reflected polarisation can be extracted and converted to Kerr/Faraday rotation and ellipticity as illustrated in Figure 3.6 (b). In both cases, since the near-field distribution is saved in the output, the inverse Faraday effect amplitude can be calculated by integrating i(ExE*) over the disk volume.

3.4 All optical switching experiments

3.4.1 Femtosecond laser setup

All optical switching of magnetisation requires high-energy ultra-fast laser pulses. To generate this kind of pulses, a Light Conversion PHAROS amplified femtosecond laser is used. This laser

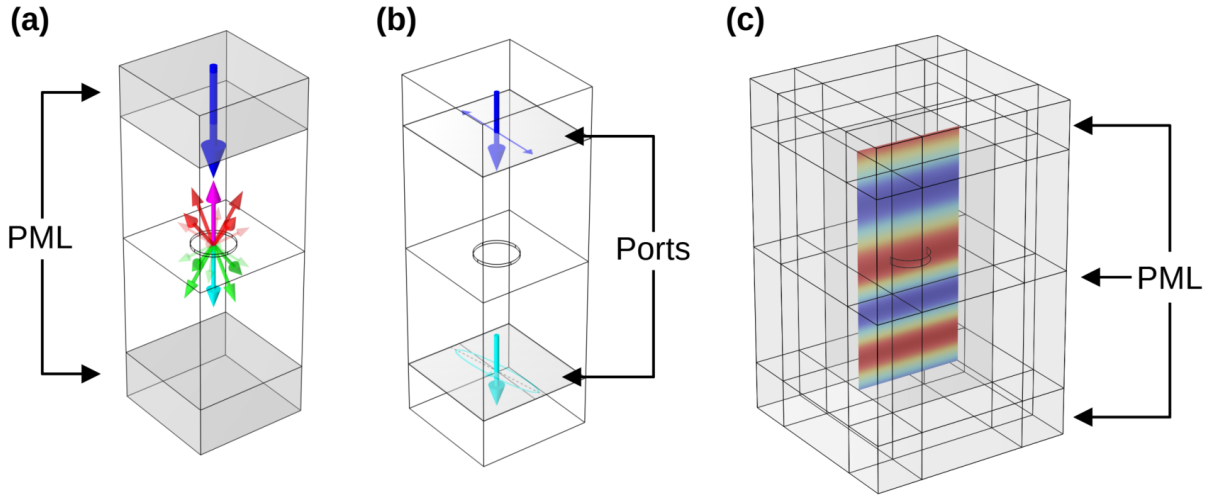

Figure 3.6: Illustration of the COMSOL geometries used to simulate the different spectra of (a)-(b) periodic square arrays of nano-disks and (c) isolated nano-disks. (a) Illustration of the incident light (blue arrow) and the resulting reflected (magenta arrow), transmitted (cyan arrow) and the diffraction orders (red and green arrows). (b) Illustration of the incident (blue) and transmitted (cyan) polarisation at the simulation ports. Illustration of the analytical background electric field used as input in the scattered field formulation to simulated isolated nano-disk.

has an output wavelength of 1030 nm and integrates a motorised compressor, allowing pulse durations τ_p from 300 fs to more than 10 ps. It also integrates a pulse picker, enabling single to multiple pulse emission or dividing the base repetition rate (100 kHz) of the continuous pulse train emission. The laser is used to pump two Light Conversion ORPHEUS optical parametric amplifiers (OPA), which can tune their output wavelength from 300 nm up to 1600 nm. The main output of the laser can be used directly or, after passing through a beta barium borate (BBO) crystal, to halve its wavelength to 515 nm. The OPAs and the BBO rely on nonlinear optical effects at very high intensities, and they only properly work at the shortest pulse duration ($\sim$ 230 fs).

The sample is pumped using one of the laser or OPA outputs. The power and, therefore, the pulse energy is controlled using a half-wave plate-polariser pair. The polariser angle is fixed, and the half-wave plate is motorised. This allows for automatic calibration, using a power meter just before the sample, of the transmitted power against the half-wave plate angle. The resulting mapping is fitted with the theoretical transmitted power $P = P_0\cos^2(2\theta - \phi)$ with P_0 the incident power (fit parameter), θ the half-wave plate angle and ϕ the angle between the initial polarisation and the polariser (fit parameter). This procedure allows for the computerised control of the power, enabling automated power sweeps. The pump beam is focused onto the sample at near-normal incidence. The last mirror on the pump path is motorised, allowing it to move or sweep the beam on the sample. For some experiments, a quarter-wave plate is added as the last element in the pump path to circularly polarise the light.

To image the laser-induced magnetisation changes, a MOKE microscope is integrated into the setup allowing the detection of changes in the reflected light polarisation. The probe light is linearly polarised using a polariser and then steered onto the sample with an angle of incidence of around 45°. The sample surface is imaged using a 5cm focal length lens, and the local magnetic contrast can be obtained through an analyser inserted in the imaging path. Resulting image are captured with a Hamamatsu ORCA-Fusion BT CMOS camera. The analyser angle is

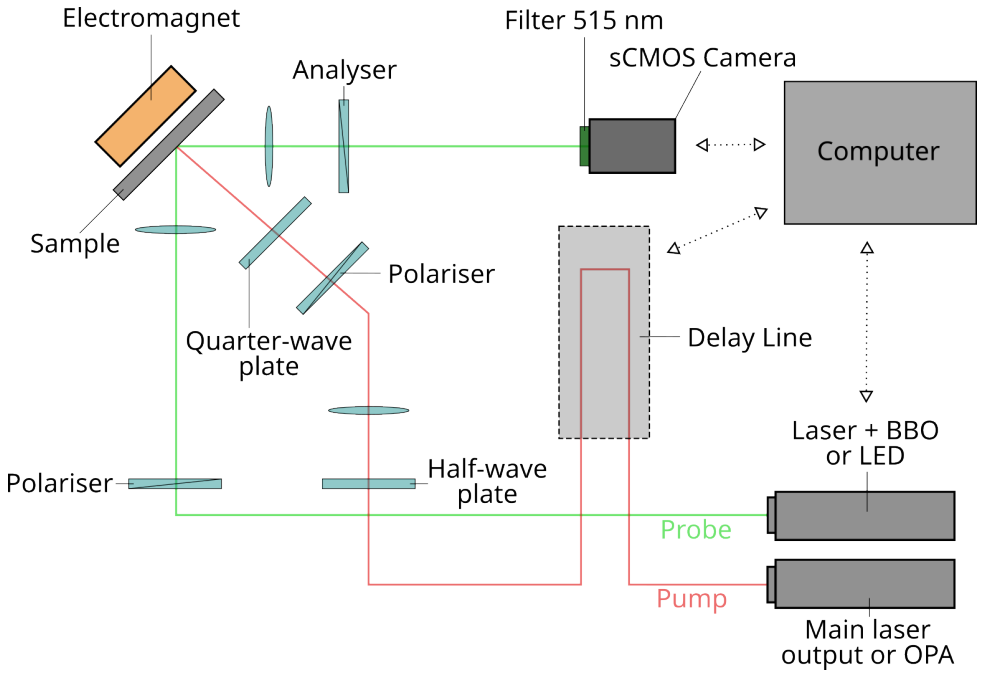

Figure 3.7: Schematic of the femtosecond laser setup.

carefully chosen to optimise the contrast between opposite magnetisation directions; usually, the analyser is nearly crossed with the polariser. Note, due to the 45° angle of incidence, the MOKE microscope is sensitive to both in-plane and out-of-plane magnetisation. The light source for imaging is either a green LED or the main laser output coupled with the BBO. A notch filter with a centre wavelength of around 515 nm is added to the camera to filter out any light from the pump or any parasitic light from the room.

The sample is attached to an XYZ stage, which allows it to be moved to the region of interest. A GMW Associates projected field electromagnet mounted to a rotation and translation stage is used to apply a magnetic field in any direction. A simplified schematic of the setup is shown in Figure 3.7.

3.4.2 State diagram

Several parts of femtosecond laser setup were automated in this thesis project, allowing systematic explorations of parameter spaces. A state diagram is one of such parameter space exploration that compiles the behaviour of the AOS depending on the pulse duration and laser fluence. To produce a state diagram, the main output of the laser is used as the pump, and the LED serves as the imaging light source. The laser internal motorised compressor is used to change the pulse duration, which is measured using an autocorrelator and mapped onto the compressor steps. This procedure enables programmable setting of the pulse duration. By assigning a set of power and pulse durations, the setup control program automatically performs measurements for all parameter combinations. In practice, the switching power threshold depends on the pulse duration. The power threshold dependence on pulse duration is coarsely estimated from tests with a few pulse durations, usually the shortest and longest pulses, and a few points in between. This allows for the interpolation of the power range of interest for all pulse durations in the sweep, which significantly reduces the time of the experiments.

The experiment is performed as follows:

1. The pulse duration is set using the integrated compressor.
2. The power is set by rotating the half-wave plate as previously described.
3. The sample is saturated in a given direction ($\uparrow$ or $\downarrow$) by the electromagnet.
4. A background image of the initial saturated state is taken.
5. A single laser pump pulse is sent.
6. The final magnetic state is imaged.
7. Steps 3 to 6 are repeated multiple times to average out any fluctuations in laser power.
8. Steps 3 to 7 are repeated for the opposite initial state.
9. Steps 2 to 8 are repeated for every power in the range of interest.
10. Steps 1 to 9 are repeated for every pulse duration in the range of interest.

The contrast in the final magnetic state images are normalised using the background images. Due to the probe angle the image is horizontally compressed. By using the measured scaling factor along both the horizontal an vertical direction, the images are scaled back to the correct aspect ratio. The contours of the switched areas are extracted using a threshold at half contrast

between the saturated state levels. Since the pump has a Gaussian fluence distribution, the contours are circular, and their radius is derived from the area of the switched domain via $r = \sqrt{(A/pi)}$. Each radius is associated with a power that is converted to pulse energy through the repetition rate, $Ep = P/R_{rep}$. Using the technique developed by J. M. Liu to measure laser spot size [122], the relation between the radius and the pulse energy is fitted with the following formula:

$$r_{sw} = \sigma \sqrt{ln(\frac{E_p}{\pi \sigma^2 F_{th}})} \tag{3.9}$$

With σ the Gaussian width and F_{th} the switching threshold fluence. With enough data points, the fitting parameters σ and F_{th} are estimated with high accuracy. A more detailed explanation and an extension of Liu's technique can be found in Chapter 6.

Using this technique, the switching threshold fluence is measured for all pulse durations, and the laser beam size is determined accurately. The beam size is used to determine the peak fluence from the power. Above a certain threshold, the magnetisation breaks down into small, irregular domains due to excessive heating. To extract this threshold, the images showing such features are flagged, and the number of occurrences versus peak fluence is fitted with a logistic function:

$$N = \frac{N_F}{1 + e^{-\frac{F - F_{md}}{\omega}}} \tag{3.10}$$

With N_F the number of data points at that fluence, F_{md} the multi-domain threshold fluence and ω the stochastic spread of the threshold. Note that, due to the stochastic nature of multi-domain formation resulting from the collapse of small domains, many iterations at every power are advised. Typically, ten repeats are performed, with five repeats for each of the initial states.

From those two thresholds, complete state diagrams can be produced, facilitating comparisons of AOS behavior in different magnetic films.

Chapter 4

AO-HDS in Co/Pt multilayer thin films

This chapter presents experimental results for Co/Pt multilayer thin films. The samples' magnetic properties are first examined, followed by measurements of their optical and magneto-optical response. From these measurements, the magneto-optical parameters are extracted. AO-HDS experiments are then described, and for various films, state diagrams are presented. Finally, the wavelength dependence of AO-HDS is compared to MCD and IFE spectra.

4.1 Magnetic properties of Co/Pt multilayer thin films

For this study, Co/Pt multilayers were selected as they exhibit strong AO-HDS, are widely studied in the community and have promising properties for applications [22][123][124]. The thin film samples were grown via magnetron sputtering by Michel Hehn [4]. The films were grown on glass substrates and are composed of the following stack: glass/Ta(3 nm)/Pt(X nm)/[Pt(Y nm)/Co(Z nm)]$_N$/Pt(3 nm) with $N \in \{1, 2, 3, 4, 10\}$, $X \in \{2.0, 3.0\}$, $Y \in \{1.0, 2.0\}$ and $Z \in \{0.6, 0.8\}$ as illustrated in Figure 4.1 (a), (b).

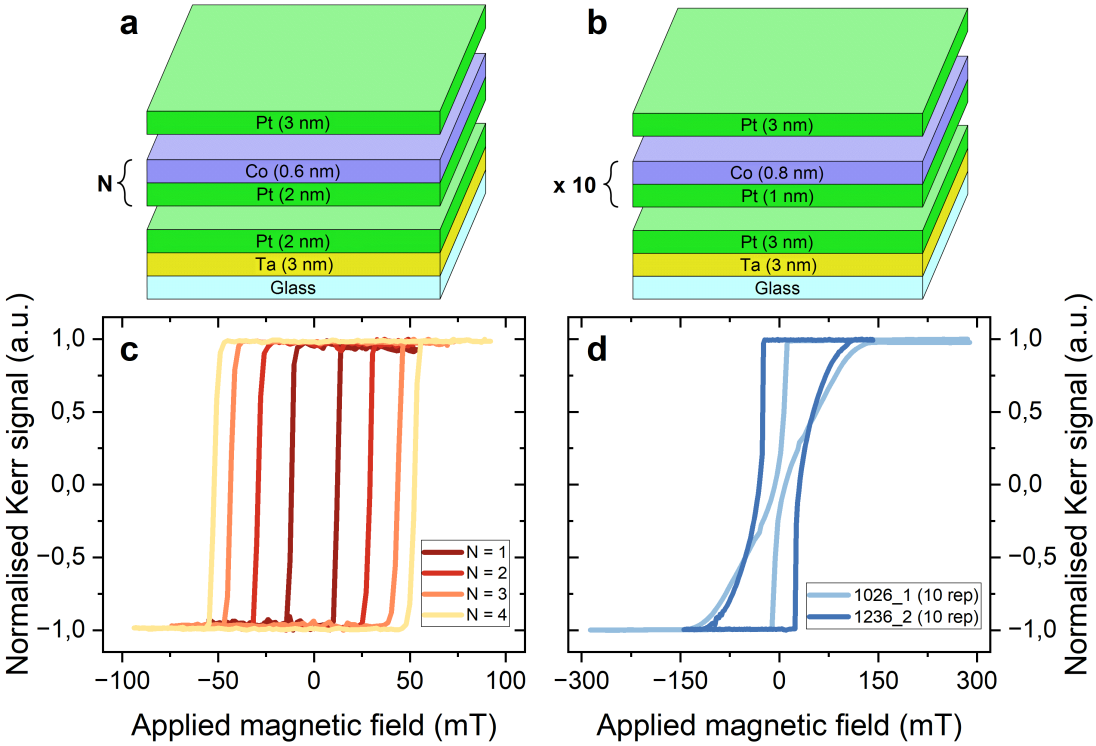

Figure 4.1: (a), (b) Representation of the studied stacks with $N \in \{1, 2, 3, 4\}$ Co/Pt repetitions and 10 Co/Pt repetitions, respectively. (c), (d) Normalised polar MOKE hysteresis loops for the corresponding multilayers.

After deposition, the magnetic properties of the films were measured with a magneto-optical Kerr effect magnetometer in polar configuration. The results are shown in Figure 4.1 (c), (d). For the first set of samples (1 to 4 Co/Pt repetitions), the measurements show a square hysteresis loop, confirming perpendicular magnetic anisotropy. Moreover, the coercivity increases with the number of repetitions. This phenomenon has already been observed and studied [123] [125] and is explained by a higher nucleation field, as defects in the layers are influenced by other layers stabilising them. This increases the field required for nucleation sites to locally initialise switching through domain wall motion. The second set of samples (10 Co/Pt repetitions) shows more complicated hysteresis loops. These samples still exhibit perpendicular magnetic anisotropy, but the magnetisation breaks down into a maze of domains when no magnetic field or a very low field is applied. A high field is required to fully saturate the sample. This behaviour is described

[4] Spintronics and Nanomagnetism group, Physics of Matter and Material department, Université de Lorraine, CNRS, Institut Jean Lamour, Nancy F-54000, France

extensively in literature [126] [127] [128]. Samples 1026_1 and 1236_2 have the same stack but were grown several months apart. Slight changes in growth conditions could explain the observed difference in behaviour. The exact origin of this difference is unknown.

4.2 Magneto-optical characterisation

Optical and magneto-optical characterisation was performed using the magneto-optical spectrometry setup at Aalto, described in the methodology chapter (page 46 - 48). Results are compiled in Figure 4.2.

None of the optical or magneto-optical spectra exhibit any pronounced features as a function of wavelength. The variation of the spectra with respect to the number of Co/Pt repetitions is monotonous with the exception of the Kerr ellipticity (e). For an increasing number of Co/Pt repetitions, the reflection R (a) increases, while transmission T (b) and absorption A (c) both decrease. This behaviour is expected for metallic films. With the exception of the Kerr ellipticity η_K (e), all magneto-optical responses, the Faraday rotation θ_F (h) and ellipticity η_F (f), as well as the Kerr rotation θ_K (g), increase with the number of Co/Pt repetitions.

For dilute solutions, MCD is commonly calculated from the extinction $(1-T)$, as only the transmission signal is measured and reflection can be neglected. In this case, the MCD can be derived from the transmission, the normalised difference of transmission, or from the Faraday ellipticity:

$$\mathrm{MCD}_T = \frac{\Delta(1-T)}{1-T} = -\frac{T\frac{\Delta T}{T}}{1-T} = -4\frac{T\tan(\eta_F)}{1-T} \tag{4.1}$$

The index T indicates that this value is derived from transmission only, which might differ from the actual MCD. The validity of this approach requires that R is sufficiently small so that $1-T \simeq A$ and that the measured Faraday ellipticity originates solely from the difference of the imaginary parts of the refractive indices for left and right-handed circularly polarised light, $\Delta\kappa$. In this case, the Faraday ellipticity is expected to strongly increase with t_m, the effective thickness of the magnetic material in the sample.

$$\eta_F(t_m) = \exp(-\Delta\kappa t_m) - \exp(\Delta\kappa t_m) \tag{4.2}$$

This observation is consistent with the measured increase of the Faraday ellipticity with the number of Co/Pt repetitions shown in Figure 4.2 (f). However, using this convention for the definition of MCD may lead to severe overestimations of the actual normalised difference in absorption, $\Delta A/A$, which is the relevant definition of MCD for this work. This becomes evident when considering that the measured Kerr and Faraday ellipticities exhibit opposite signs. A positive Kerr ellipticity indicates that the reflectivity for right-circularly polarised light is larger than that for left-circularly polarised light. Consequently, more left-circularly polarised light is transmitted, giving rise to a negative transmitted ellipticity in the material.

If MCD does not compensate for the imbalance in circular polarisation intensities via absorption, the measured Faraday ellipticity will necessarily remain opposite in sign to the reflected one. This effect reflects the conservation of total angular momentum, with the associated balance expressed in Equation 2.38. In the absence of MCD, this equations shows that the Faraday ellipticity can be expressed as:

$$\eta_F(t) = -\frac{\Delta R(t)}{4T(t)} \tag{4.3}$$

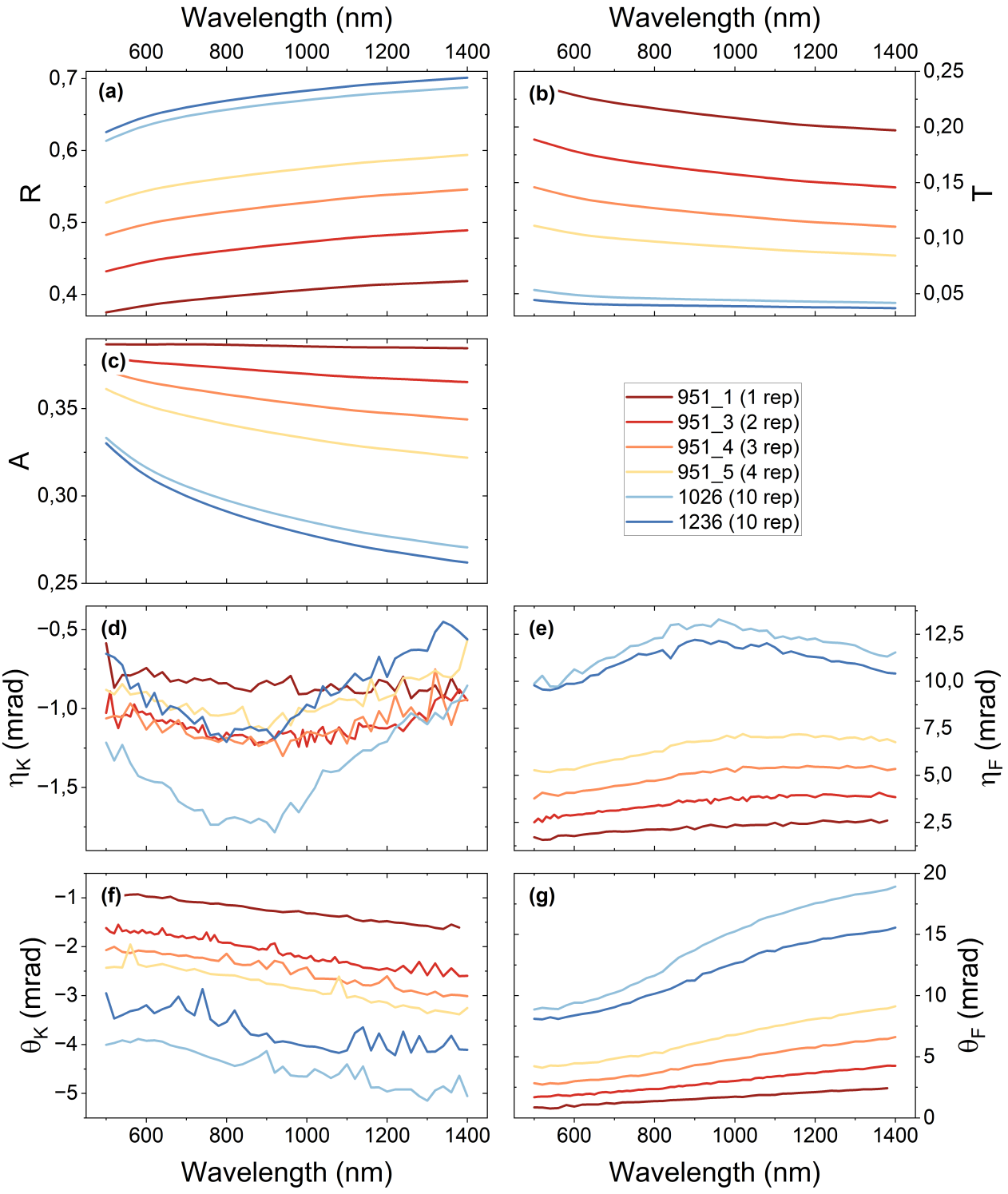

Figure 4.2: Measured optical and magneto-optical spectra for Co/Pt multilayer thin films. (a) Reflection, (b) transmission and (c) absorption spectra. (d) Measured MCD retrieved from measurements in transmission and reflection. (e) Kerr ellipticity, (f) Faraday ellipticity, (g) Kerr rotation and (h) Faraday rotation spectra.

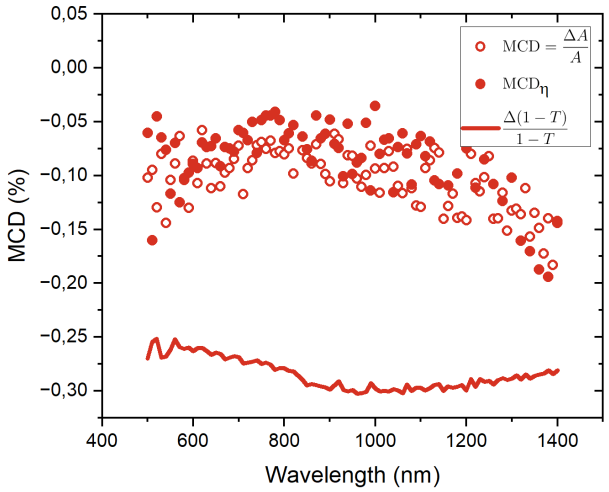

Figure 4.3: MCD spectra from sample 951_3 (2 Co/Pt repetitions) using different formulas for the calculation of MCD. (open symbols) MCD calculated as the normalised difference of absorption. (filed symbols) MCD calculated from the measured Kerr and Faraday ellipticities. (line) Normalised difference of the extinction.

In the case of thickness-independent ΔR, this leads to a comparable increase in both Faraday ellipticity and MCD_T with increasing magnetic film thickness, even in the absence of any absorption difference between opposite circular polarisations in the film.

To properly determine the MCD, defined as the normalised absorption difference $\Delta A/A$, both transmitted and reflected signals must be measured, from which the value can be calculated using Equation 3.8. Alternatively, MCD can be obtained from optical reflectivity and ellipticity measurements via Equation 2.38; in this case, the result is denoted as MCD_η. As demonstrated in Annexe B and shown in Figure 4.3, both approaches are fully equivalent.

Figure 4.4 shows the spectra of ΔR, ΔT, MCD and MCD_T for all films, calculated from the optical and magneto-optical measurements. For the first sample set (1 to 4 Co/Pt repetitions), ΔR and ΔT (a) have similar amplitudes but opposite sign, resulting in a small MCD that is significantly weaker than MCD_T (b). In this case, the amplitude of ΔT is slightly larger than that of ΔR, so MCD and MCD_T mostly share the same sign. This behavior contrasts with the second set of samples (10 Co/Pt repetitions), where ΔR dominates ΔT for most wavelengths (c), leading to sign differences between MCD and MCD_T (d).

The determination of MCD for the films leads to the following conclusions:

1. The measurement of $\Delta R/R$ and $\Delta T/T$ with the dedicated setup configuration is identical to the measurement of η_K and η_F. Either approach can be used to calculate MCD, as shown in Figure 4.3.

2. The experimental determination of the MCD of metallic multilayer structures requires knowledge of R, T, η_F and η_K. Measurements of T and η_F alone, are insufficient. They lead to erroneous values of MCD_T, which can diverge (approaching infinity), when the true MCD is zero, and can even yield the wrong sign, as demonstrated in Figure 4.4 (d).

3. The MCD of a bulk material, defined as the difference between the imaginary parts of the refractive indices for opposite circular polarisations, fundamentally differs from the MCD

of a thin film made of this material, defined as the normalised difference in absorption for opposite circular polarisations. This difference arises from reflection effects at the film interfaces, which depend on both $\Delta\kappa$ and the corresponding differences in the real parts of the refractive indices Δn, i.e., the magnetic circular birefringence (MCB).

4. The differences in reflectivity, transmission, and absorption between right- and left- circularly polarised light in a metallic multilayer stack, strongly depend on the thicknesses and refractive indices of all layers, even when the stack comprises only a single magnetic material with given intrinsic MCD ($\Delta\kappa$) and MCB (Δn).

5. It should be possible to optimise MCD of a multilayer stack for a given purpose, for example, to maximise its magnitude for strong helicity-dependent switching, by selecting appropriate layer thicknesses and material combinations (refractive indices).

To enable such optimisations, the full experimental dataset is used to derive the material

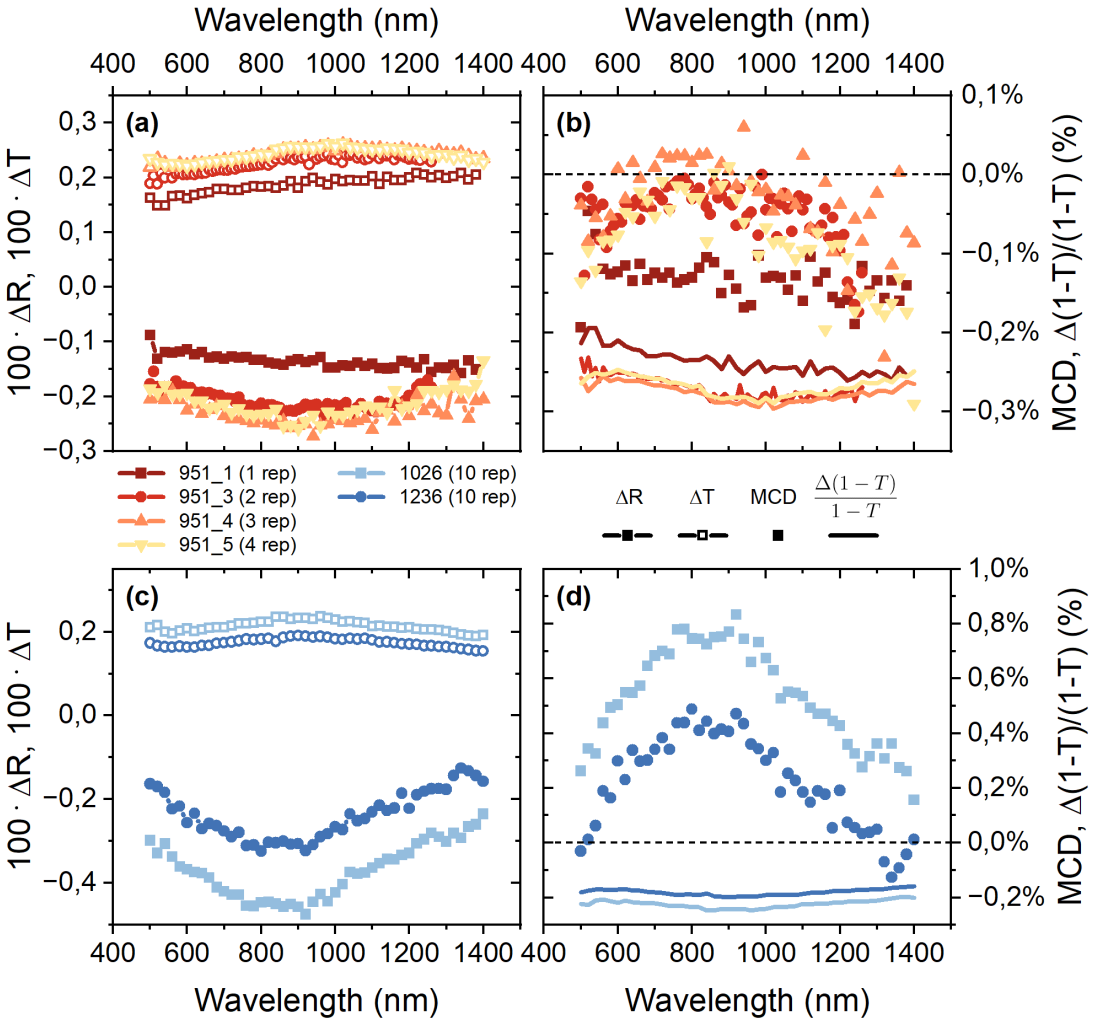

Figure 4.4: MCD spectra for Co/Pt multilayer thin films. (a), (c) ΔR (filed symbols) and ΔT (open symbols) spectra for the different samples. (b), (d) MCD (filed symbols) and extinction ratio (lines) for the different samples.

specific magneto-optic parameters. The simulation of magnetic thin films and the retrieval of their wavelength dependent magneto-optical parameters are discussed in the next section.

4.3 Simulation and Voigt parameter fitting

To simulate the magneto-optical response of the magnetic films, a few parameters are needed, such as the optical indices n and κ and the complex Voigt parameter $Q = Q_r + iQ_i$. For some materials, these parameters can be found in literature. R. Atkinson has published tabulated values for optical and magneto-optical properties of Co/Pt and CoNi/Pt multilayers [116]. However, the samples studied in his paper consist of more bilayer repetitions, and the Co and Pt layer thicknesses are different. Nevertheless, Atkinson proposed a method to extract those values for any samples through spectroscopic ellipsometry and measurements of Kerr/Faraday rotation and ellipticity spectra.

In this work, measurements were carried out on full thin films grown simultaneously with those used for the fabrication of plasmonic nanostructures. The samples included Co/Pt multilayers with 1,2,3,4, and 10 repetitions, as described in the previous section. Spectroscopic ellipsometry was performed using a J.A. Woollam M-2000UI system[5]. After calibration with a reference sample, the measurements were performed at three incidence angles (65°, 70° and 75°) for wavelengths from 245 to 1690 nm. The optical constants were extracted by fitting the data with the CompleteEASE® software package [129].

The multilayer stack was modelled as a glass substrate, described by a Cauchy equation, with a homogeneous film on top. The optical indices of the effective metallic films are described by an adjustable B-Spline allowing the fitting of their optical responses. The film thickness was set to the total thickness of the multilayer, the B-Spline resolution was set to 0.1 eV, and the Kramers-Kronig mode was activated to constrain the extracted optical spectra of to physically meaningful values and shapes. The resulting fitted spectra for different films are plotted in Figure 4.5.

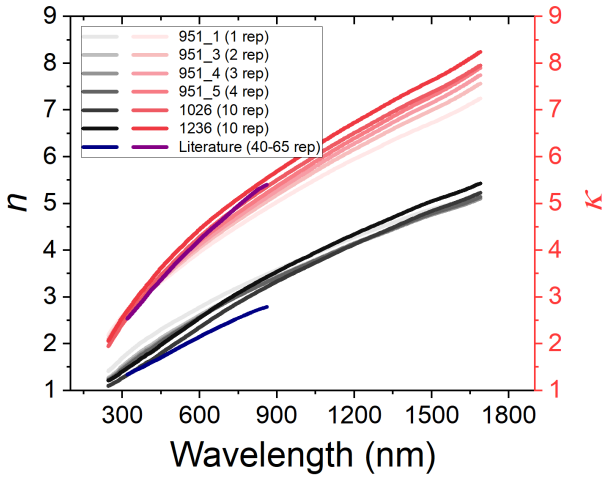

Figure 4.5: Spectra of optical indices n and κ for Co/Pt multilayers. The legend indicates the sample name and number of Co/Pt repetitions. Curves corresponding to the indices measured by R. Atkinson [116] are shown for comparison.

A weak dependence of the optical constants on the number of Co/Pt repetitions is observed.

[5]This equipment belongs to the Soft Matter and Wetting group, Department of Applied Physics, Aalto University, Aalto FI-00076, Finland. Access and training were kindly provided by the main user, Sakari Lepikko.

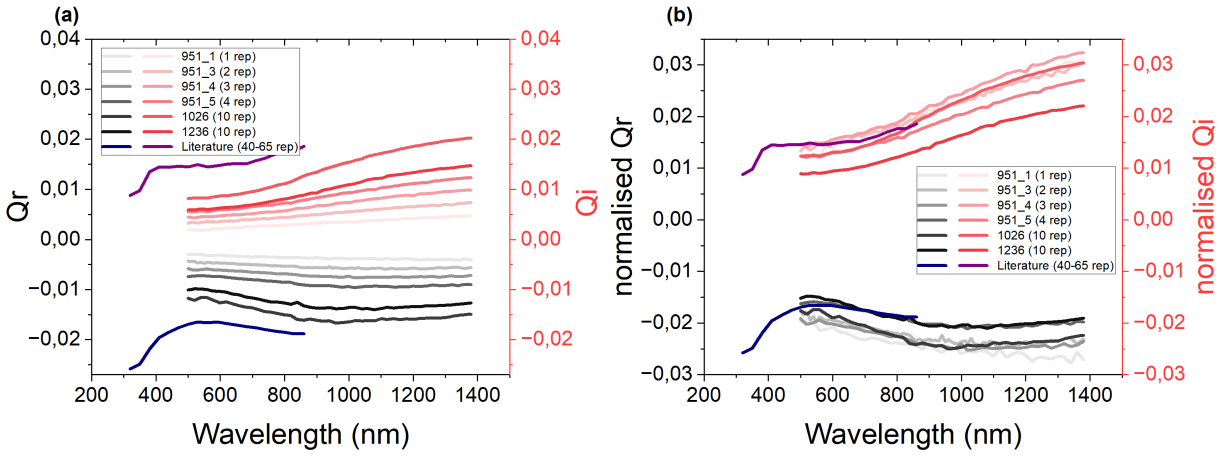

Figure 4.6: Voigt parameter spectra for Co/Pt multilayers. (a) Non-normalised effective Voigt parameters. (b) Voigt parameters normalised by the ratio between the total and magneto-optical active thickness of the film. The legend indicates the sample names and number of Co/Pt repetitions. The literature curves correspond to the parameters fitted by R. Atkinson [116].

This effect is attributed to the relative thickness contributions of the Co/Pt multilayer and the Ta buffer layer. As the number of repetitions increases, the impact of the Ta layer becomes progressively diluted. The extracted optical constants are in good agreement with literature values. In addition, the optical constants of the glass substrate were determined for later use.

The measured Kerr/Faraday rotation and ellipticity spectra discussed in the previous section were simulated and fitted using the 4x4 transfer matrix method (4x4 TMM) described in the methodology chapter (page 49).

The samples were modelled as single homogeneous magnetic layers of the corresponding thickness, magnetised along the out-of-plane direction, and supported by a glass substrate. Using the optical constants obtained from ellipsometry, the measured MO response at normal incidence was fitted by tuning the complex Voigt parameters $Q = Q_r + iQ_i$ at each wavelength [116]. The resulting values of Q_r and Q_i are compiled in Figure 4.6 (a).

The variation of the obtained Voigt parameters with the number of Co/Pt repetitions is more pronounced than that observed for the optical constants. Both Q_r and Q_i increase with the number of repetitions but appear to saturate when compared with the results of R. Atkinson. This is surprising, as Voigt parameters are considered as intensive properties. As with the optical constants, this behaviour can be partly attributed to the decreasing impact of the Ta buffer layer as the Co/Pt thickness increases.

Normalisation of the Voigt parameters is not straightforward; as the magneto-optically active layer includes not only the Co layers but also the polarised Pt, arising from proximity-induced magnetism. As a first approximation, each Co layer can be assumed to induce an effective magnetisation in the adjacent Pt equivalent to around 1 nm of magneto-optically active material (0.5 nm at each interface) [130] [131]. Using this normalisation mostly rectifies the apparent thickness dependence, although some discrepancies remain. For example, sample 1236 seems to behave as if its effective thickness is smaller than anticipated. In any case, the extracted values can be used as effective Voigt parameters corresponding to a homogeneous magnetic material of the same thickness as the measured films.

4.4 All-optical helicity-dependent switching

4.4.1 State Diagrams

State diagrams were produced for opposite circular polarisations on selected films following the procedure described in the methodology chapter. A polariser and a quarter-wave plate were added to the pump path as the final optical elements before the sample, as illustrated in Figure 3.7. The polarisation was characterised using an additional polariser and a calibrated power meter to measure the transmitted power. Two quarter wave-plate (QWP) positions, corresponding to the polarisations of interest, were fully characterised and used in the experiments: 45° and 315°, corresponding to right circular polarisation (σ_+) and left circular polarisation (σ_-), respectively. Instead of using a single laser pulse, the samples were irradiated with $N_p \in \{100, 1000, 10000\}$ pulses.

Observations of the final magnetisation state using MOKE microscopy before post-processing reveal clear helicity-dependent behaviour. Figure 4.8 shows the final magnetisation state of sample 951_1 (1 repetition of Co/Pt) after 1000 pulses of 1.2 ps for different peak fluences, depending on the initial magnetisation state and light polarisation. Figure 4.8 (a) depicts the results for a peak fluence of 1.60 mJ/cm², for which two combinations of initial magnetisation and light polarisation show full switching ($(\uparrow, \sigma_+)$ and $(\downarrow, \sigma_-)$), while the other combinations remain unaffected ($(\uparrow, \sigma_-)$ and $(\downarrow, \sigma_+)$). This anti-symmetric behaviour with respect to the initial state and circular polarisation is characteristic of AO-HDS. Increasing the peak fluence, as shown in Figure 4.8 (b), results in the previously switched combinations forming a switched ring around a multidomain region, while the non-switched states only show multidomains. The

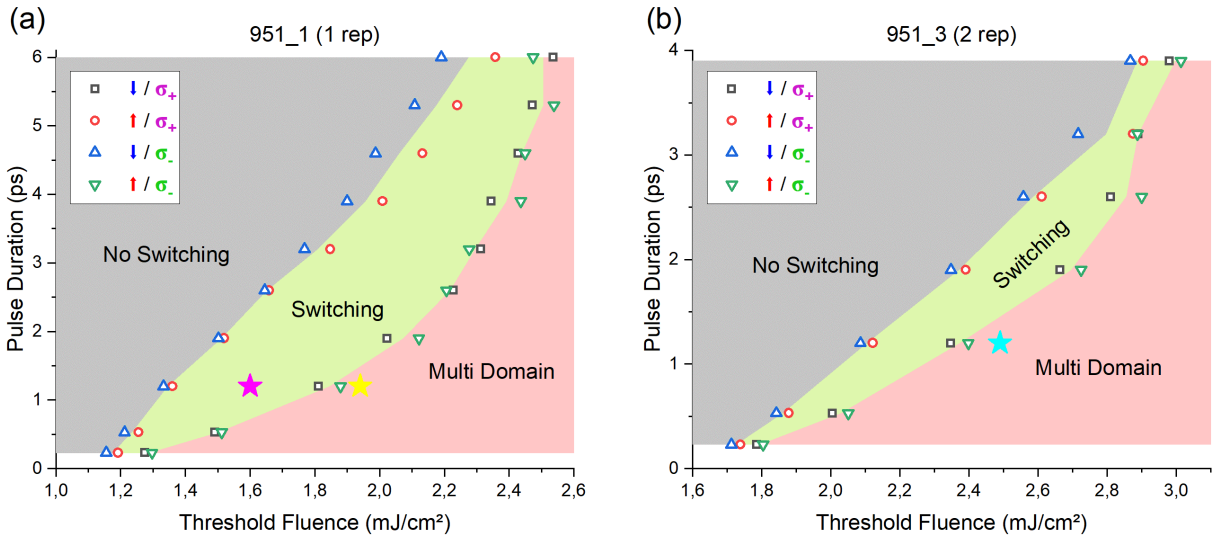

Figure 4.7: AO-HDS state diagrams of Co/Pt multilayers films. (a) State diagram of sample 951_1 (1 Co/Pt repetition). (b) State diagram of sample 951_3 (2 Co/Pt repetitions). The state diagrams are obtained with 1000 laser pulses at a repetition rate of 100 kHz and pump wavelength of 1030 nm. The open symbols represent the fitted thresholds for the corresponding light polarisation and initial magnetisation state. The background colours indicate the calculated threshold fluences of combinations corresponding to switching or multidomain formation. The magenta, yellow and cyan stars correspond to the pulse duration and peak fluences used in Figure 4.8 and Figure 4.9, respectively.

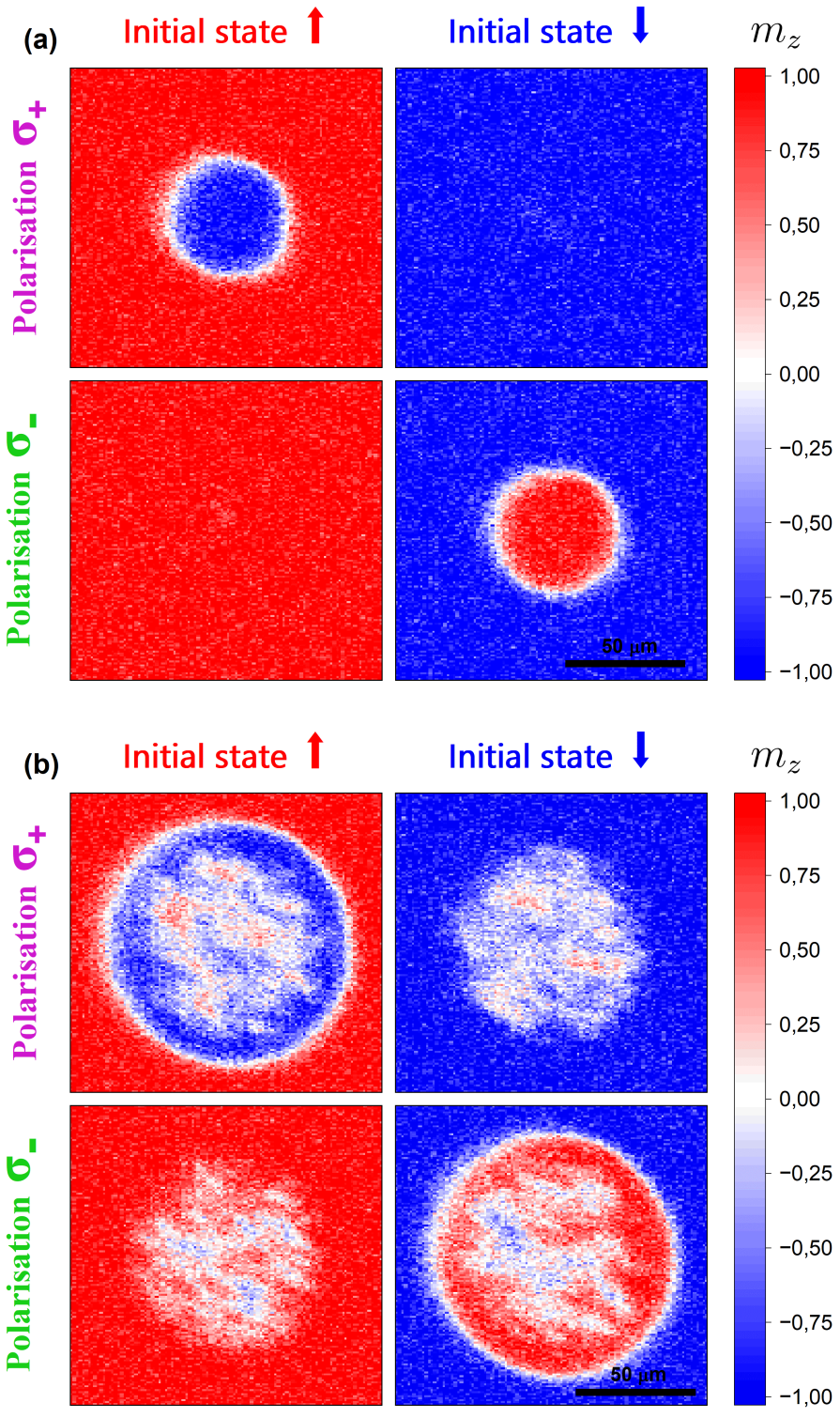

Figure 4.8: Normalised MOKE images of the final magnetisation states of sample 951_1 (1 Co/Pt repetition) after 1000 laser pulses of 1.2 ps depending on the initial state (up or down magnetisation) and the circular polarisation of light (σ_+ or σ_-). Results are shown for a peak laser fluence of (a) 1.60 mJ/cm^2 and (b) 1.94 mJ/cm^2. The pump wavelength is 1030 nm, the repetition rate is set to 100 kHz, and the laser spot radius is 98 µm. The scale bar in the bottom right corresponds to 50 µm. All images are plotted on the same scale.

size of the switched and multi-domain regions was determined by measuring the radius of the smallest circle enclosing the affected area. A pixel was considered part of the affected region if its contrast changed by more than a threshold set above the background noise. Depending on the combination of initial magnetisation and light polarisation, this radius corresponds to either the switched or multidomain threshold.

Fitting the evolution of the radius with pulse energy using Equation 3.9 provides a threshold fluence for every combination of initial magnetisation and light polarisation. These threshold fluences are compiled for all pulse durations of interest in Figure 4.7 (a). This state diagram differs from the previously reported static state diagram for Co/Pt in the AO-HDS section (Figure 1.9). The switching threshold fluence increases linearly with pulse duration, while the multidomain threshold fluence exhibits a more quadratic dependence. These results define the fluence window for AO-HDS, which is largest for a pulse duration around 2 ps.

Measurements were also conducted on sample 951_3 (2 repetitions of Co/Pt). Similar behaviour was observed, but the gap between the switching and multidomain thresholds was smaller as shown in Figure 4.9. For similar ratios between the peak laser fluence and the multidomain threshold, the switched ring is less pronounced. Correspondingly, the ratio between the radii of the affected regions for switching and multidomain states is reduced. The multidomain patterns also differ between samples. The domains in sample 951_3 appear smaller than in sample 951_1.

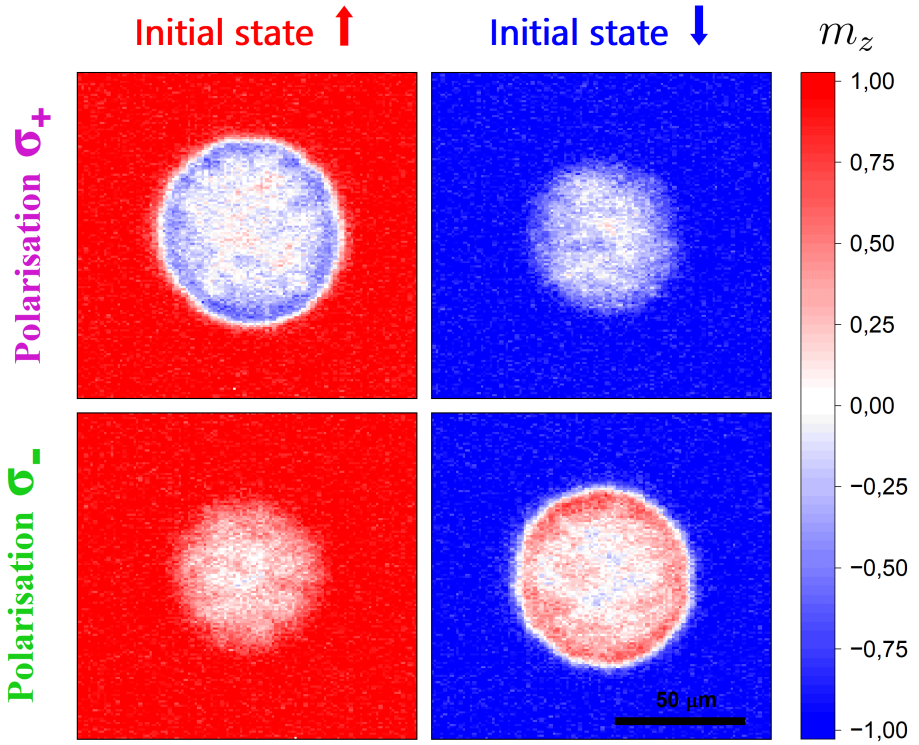

Figure 4.9: Normalised MOKE images of the final magnetisation states of sample 951_3 (2 Co/Pt repetitions) after 1000 laser pulses of 1.2 ps, depending on the initial state (up or down magnetisation) and circular light polarisation (σ_+ or σ_-) for a peak fluence of 2.49 mJ/cm^2. The pump wavelength is 1030 nm, the repetition rate is set to 100 kHz, and the laser spot radius is 101 µm. The scale bar in the bottom right corresponds to 50 µm. All images are plotted on the same scale.

This difference is especially noticeable in the non-switching configuration: sample 951_1 exhibits sharp, and irregular domain edges with regions nearly reaching full contrast, whereas the domain edges in sample 951_3 are smoother, and the contrast changes barely cross zero. This reduced helicity dependence is confirmed by the state diagram in Figure 4.7 (b). Compared to sample 951_1, the threshold fluences are higher and the relative fluence window for switching is smaller.

This trend of diminishing AO-HDS with increasing number of Co/Pt repetitions continues: for three or more repetitions, switching is barely observed. Films with ten repetitions were not measured because, at zero field, sample 1026_1 spontaneously forms a multidomain state, and sample 1236_2 did not show any signs of AOS. The observed trends of decreasing domain size and switching window with increasing number of Co/Pt repetitions reflects the impact of increasing demagnetising fields and is the reason for the minimum domain size criterion for AOS put forward by Elhadri et al.[66].

4.4.2 Spectral behaviour

Finally, the wavelength dependence of AO-HDS in the thinnest film was studied by changing the pump wavelength instead of the pulse length. To ensure proper operation of the optical parametric amplifier, the pulse duration was fixed at 230 fs. Only the single-repetition sample was studied, as it showed the largest AO-HDS window. Measurements were performed for three polarisation settings: right circular (σ_+), left circular (σ_-) and linear polarisation. Threshold fluences were extracted from the fits of the spot radii versus pulse energy for the circular polarisations and normalised by the multidomain threshold obtained with linear polarisation. The data were grouped according to whether they corresponded to the switching or multidomain threshold. The results are summarised in Figure 4.10.

These results reveal a very small difference between the switching and multidomain thresh-

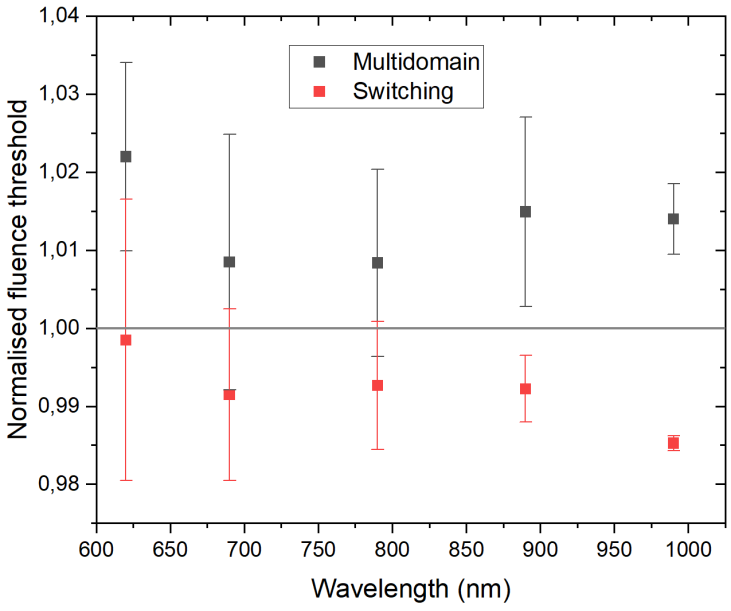

Figure 4.10: Normalised AO-HDS switching and multidomain fluence threshold spectra of sample 951_1 (1 Co/Pt repetition). The fluence ratios values are calculated from the switching and multidomain thresholds extracted for circular polarised light divided by the multidomain thresholds extracted for linearly polarised light.

olds, with a maximum of 3 % at a wavelength of 990 nm. A slight increase in the threshold gap with wavelength is observed, but no definitive correlation can be established, as the MCD and rotation spectra remain relatively flat within the measured wavelength range. This measurements highlights the main challenge in disentangling the contributions of MCD and the IFE in AO-HDS. In thin films, their spectral behaviours are too similar to distinguish them spectrally.

To address this, magneto-plasmonic structures are studied in the next chapter, introducing distinct features into their magneto-optical spectra that allow separation of MCD and IFE effects on AO-HDS. The magneto-optical study described in this chapter produced a complete characterisation of the optical and magneto-optical properties of Co/Pt multilayer thin films. These parameters will be utilised to simulate the plasmonic and magneto-plasmonic responses of the nanodisks discussed in the next chapter.

Chapter 5

AO-HDS in Co/Pt nanodisks

In this chapter, the impact of plasmonic resonances on the spectral behaviour of all-optical helicity-dependent switching in nanometric magneto-plasmonic structures is studied. Sample exhibiting plasmonic resonances in the visible to near-infrared range were fabricated, their magneto-optical spectra were measured, and their response to circularly polarised femtosecond laser pulses was characterised. While switching experiments on periodic arrays did not show a clear correlation with the measured magneto-optical spectra, a sign change in the switching spectra at the plasmonic resonance wavelength was observed for samples with randomly distributed Co/Pt nanodisks. This observation suggests a central role of MCD, or an MCD-like effect, in all-optical helicity-dependent switching.

5.1 Motivation

AO-HDS is a promising phenomenon for next-generation data storage devices. However, to fully exploit its potential and optimise its efficiency, the underlying mechanism must be thoroughly understood. Furthermore, plasmonic systems can enhance light-matter interaction, potentially reducing the energy required for switching. Magneto-plasmonic systems thus provide an ideal platform for investigating and optimising AO-HDS.

As described in the Chapter 1, the origin of AO-HDS is still debated, with multiple mechanism potentially contributing. This thesis focuses on magnetic circular dichroism (MCD) and the inverse Faraday effect (IFE), as described in previous chapters. Near plasmonic resonances, the spectral responses of MCD and IFE are different, enabling their effects on AO-HDS to be disentangled through wavelength-dependent measurements.

5.2 Sample preparation

For this study, samples with ten Co/Pt repetitions (1026_1 and 1236_2) were chosen due to their strong magneto-optical contrast and pronounced magneto-plasmonic response. Using the nanofabrication process described in Section 3.1, the films were patterned into randomly distributed nanodisks and periodic nanodisk arrays, as illustrated in Figures 5.1 (a) and (b). The structural parameters of the nanodisks, including disk diameters D and array periodicity P, were characterised using Atomic Force Microscopy (AFM), see Annexe A for more details. The dimensions of the nanodisks and arrays were chosen to position plasmonic resonances in the visible to near-infrared spectral range. The packing density of the randomly distributed nanodisks was

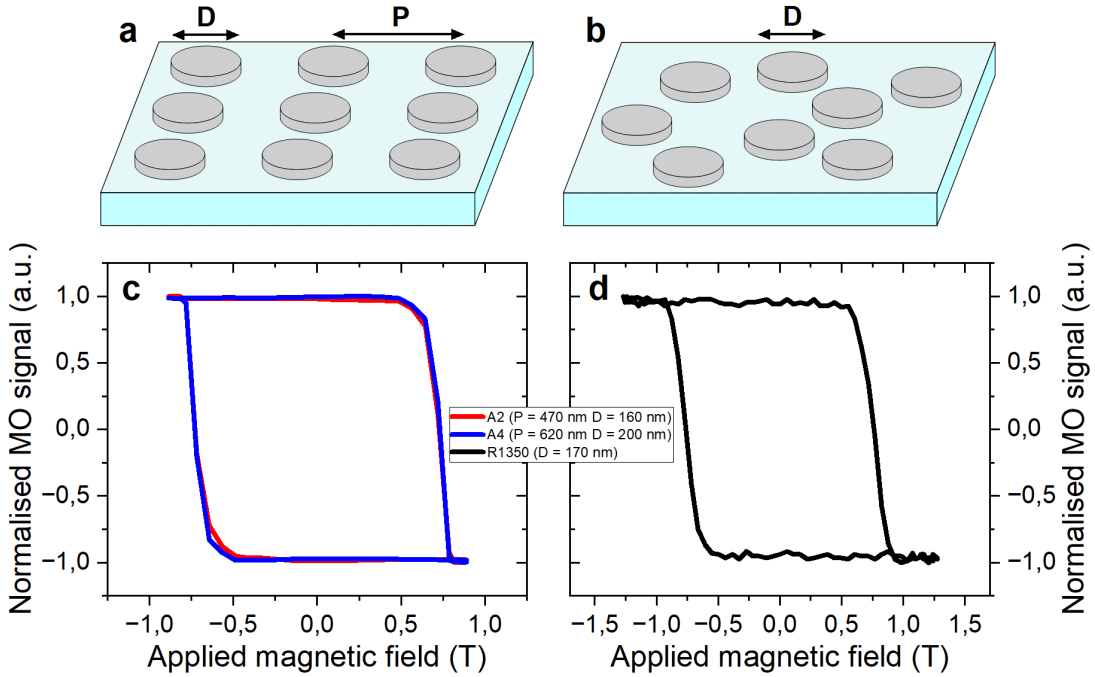

Figure 5.1: Representation of the studied plasmonic systems. (a) Periodic square array of nanodisks with periodicity P and diameter D. (b) Randomly distributed nanodisks with diameter D. (c), (d) Polar MOKE hysteresis loops for the studied systems.

matched to that of the periodic arrays. In some cases, arrays were capped with 200 nm of SiO_2 to create a uniform dielectric environment for optimal SLR excitation.

Polar MOKE hysteresis loops for both periodic and randomly distributed nanodisks are shown in Figure 5.1 (c) and (d). These results illustrate that patterning of the films into nanodisks preserves perpendicular magnetic anisotropy. However, the coercivity greatly increases to around 730 mT for the periodic arrays and 770 mT for the randomly distributed nanodisks. In contrast to thin films, the small size and higher coercivity of the nanodisks maintain the magnetisation mostly uniform within each disk (see Annexe D). This uniformity allows the initialisation of a saturated magnetisation state for AO-HDS experiments, whereas thin films would break into multidomain configurations at zero field.

5.3 Optical and magneto-optical characterisation

Optical and magneto-optical characterisation of the nanodisk arrays was performed using the setup in Aalto University, as described in the methodology chapter (page 46 - 48). In parallel, COMSOL simulations were carried out using the structural parameters measured by AFM, together with the permittivities and Voigt constants derived from ellipsometry measurements on the full films. Figure 5.3 show results for two periodic square arrays capped with 200 nm of SiO_2 and immersed in index-matching oil, alongside corresponding COMSOL simulations. Panels (a) and (e) show the absorption spectra, where diffraction orders and surface lattice resonances (SLRs) are clearly visible. As described in Sections 2.1.3 and 2.1.4, the wavelength and width of SLR can be tuned by varying the disk size and array periodicity. In these experiments, the plasmonic structures were designed to exhibit resonances around 800 nm and 1030 nm, which correspond to the natural wavelengths of the femtosecond laser systems at IJL. Panels (c)/(g) and (d)/(h) highlight the relationship between Kerr/Faraday ellipticity and MCD. In particular, panels (d) and (h) compare the MCDs of the plasmonic arrays with that of the full films, revealing a three to fourfold enhancement of MCD in the magneto-plasmonic arrays at specific wavelengths. The MCD of the arrays crosses zero and changes sign at the SLR wavelength.

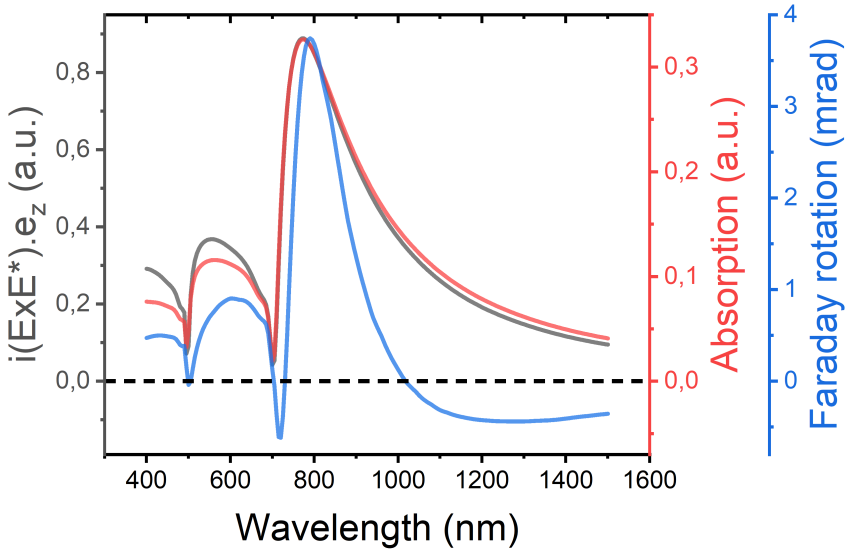

Figure 5.2: Simulated spectra of $i(E \times E^*).e_z$, absorption and Faraday rotation for a nanodisk array with 10 Co/Pt repetitions, periodicity $P = 470$ nm and diameter $D = 160$ nm.

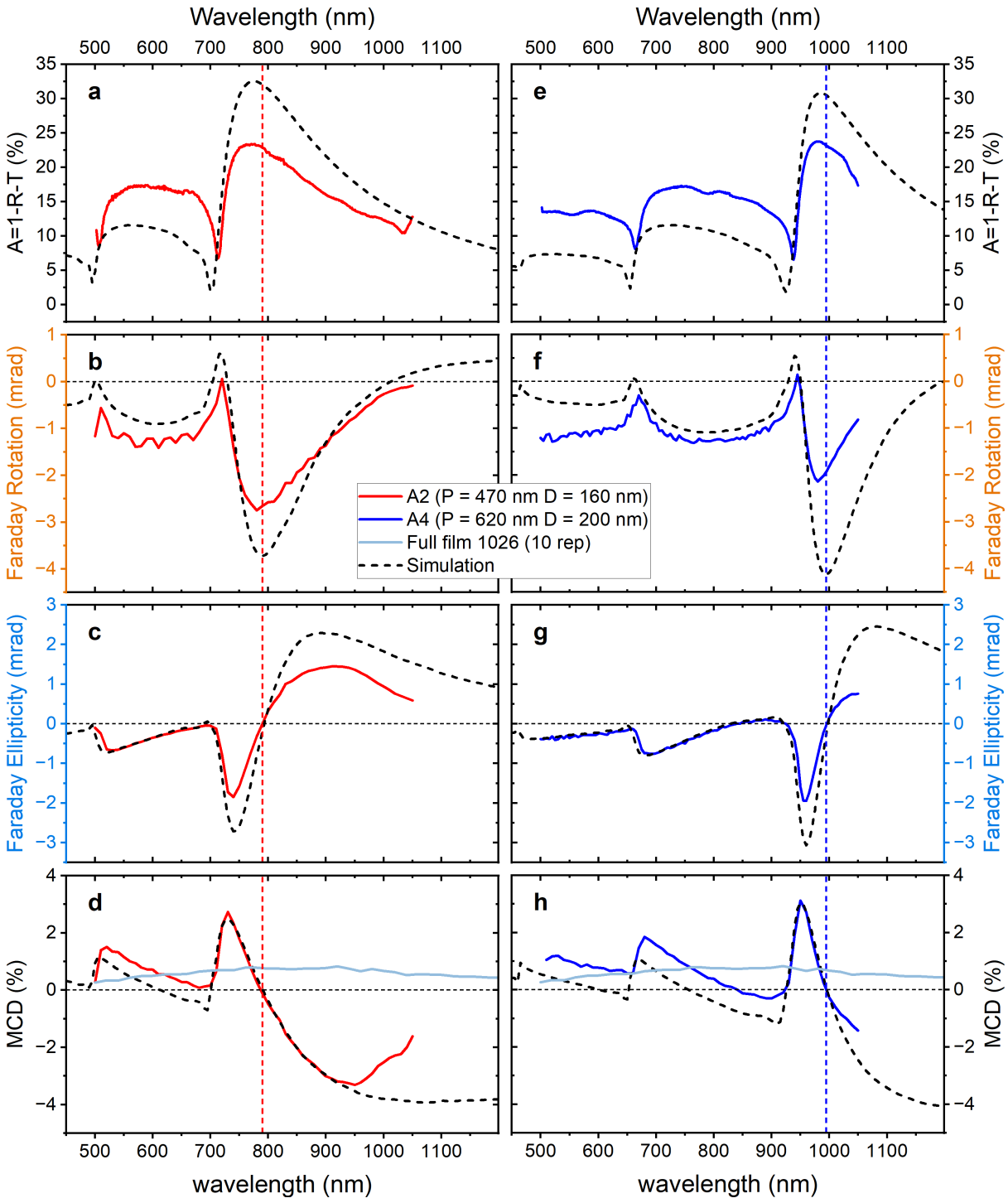

Figure 5.3: Measured and simulated optical and magneto-optical spectra for a sample with 10 Co/Pt repetitions (1026_2) nanofabricated into two periodic square arrays: array A2 (P = 470 nm D = 150 nm) in red (a)-(d) and array A4 (P = 620 nm D = 190 nm) in blue (e)-(h). (a),(e) Measurements of absorption. (b),(f) Measurement of MCD. (c),(g) Measurement of the Faraday rotation. (d),(h) Measurement of Faraday ellipticity. The black dashed curves indicate corresponding COMSOL simulations for the same structures. The light blue curves in (d), (h) correspond to the MCD of the full film with 10 Co/Pt repetitions (1026). The vertical coloured dash lines indicate the wavelength where the MCD/Faraday ellipticity crosses zero.

COMSOL simulations reproduce most features of the experimental spectra, including the resonance wavelengths. Minor discrepancies in resonance amplitudes are attributed to non-ideal sample geometries: nanodisks are not perfect cylinders, and impact of nanofabrication on optical and magneto-optical constants is not fully known. Nevertheless, the position of resonances and zero crossings of ellipticity and MCD are well reproduced.

The simulation also allow investigation of the link between the IFE and Faraday rotation. Figure 5.2 show the simulated IFE, Faraday rotation, and absorption for array A2 (P = 470 nm and D = 160 nm). The simulations show that MCD is maximal at the resonance wavelength, where near fields are confined and enhanced. Kerr and Faraday rotations are also amplified at the resonance but may change sign away from it, as observed in both experiments and simulations. In contrast, the IFE does not change sign in these structures. A better indicator of the IFE amplitude is the absorption spectrum. This is because both the absorption and IFE scale linearly with the intensity of the near field: $A \propto \Re(i(E.E^*)) \propto |E|^2$ for absorption and $M_{IFE} \propto i(E \times E^*) \propto |E|^2$ for IFE. The plasmonic resonance amplifies both effects due to the confinement and enhancement of near fields in the magneto-plasmonic structures. While the Faraday and inverse Faraday effects are linked through the Verdet constant, in a dissipative medium, the constants governing the two effects differ [60], which explains the differences in

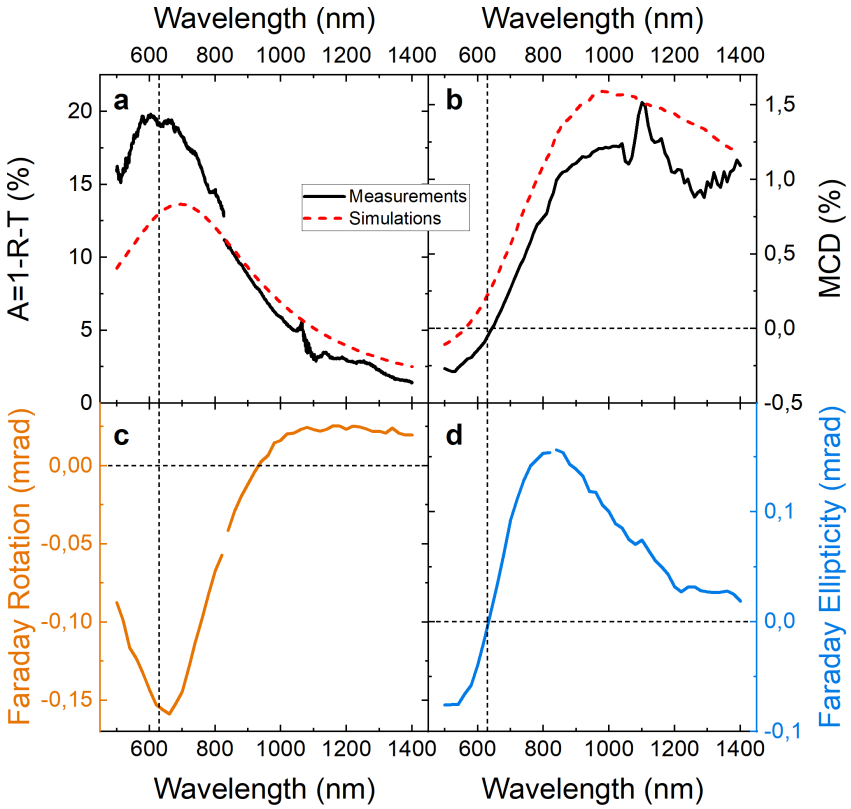

Figure 5.4: Measured and simulated optical and magneto-optical spectra for a sample with 10 Co/Pt repetitions (1236) nanofabricated into randomly distributed disks with diameter D = 170 nm (R1350). (a) Measurement and simulation of absorption. (b) Measurement and simulation of MCD. (c) Measurement of the Faraday rotation. (d) Measurement of Faraday ellipticity. The vertical dash lines indicate the wavelength where the MCD/Faraday ellipticity crosses zero.

their spectral features.

Figure 5.4 shows the optical and magneto-optical characterisation of randomly distributed nanodisks with a diameter of 170 nm. As expected, the observed localised surface plasmon resonance (LSPR) is much broader compared to the SLRs observed in periodic arrays. The links between Faraday ellipticity and MCD, as well as between rotation and absorption, remain consistent with those described for the periodic structures. Some noise, likely originating from the laser or the optical acoustic filter, produces artificial features in the absorption and MCD signals above 1050 nm. Discrepancies between the experimental and simulated LSPR wavelengths and amplitudes are attributed to the initial thin film being thinner than expected. Additionally, small differences in optical and magneto-optical properties between samples 1026_1 and 1236_2, which are supposedly identical but grown at different times, were also observed in the full films (see previous chapter). Despite these minor differences, the overall shape of the plasmonic resonance is well reproduced by the simulations.

5.4 All-optical switching experiments

5.4.1 Measurements

To perform the switching experiments, the setup described in Section 3.4.1 was modified. Imaging was performed using an LED, while the pump beam was provided by one of the OPAs. A polariser and a quarter-wave plate were added at the end of the pump path to control the light polarisation. The polarisation was characterised using another polariser and a calibrated power meter to measure transmitted power. Three polarisations states of interest were fully characterised and used in the experiments: linear polarisation (QWP at 0°), right circular polarisation (RCP, QWP at 45°), and left circular polarisation (LCP, QWP at 315°). Due to the high coercivity of the nanofabricated structures (around 750 mT), the electromagnet in the setup could not saturate the samples. To address this, a custom-made permanent gap magnet was designed and built[6]. A position-adjustable rail was also built to safely slide the magnet around the fix samples, as the gap of the magnet is relatively small (5 mm), without causing damage. Finally, to enable scanning of the laser across the sample, the last mirror in the pump path was motorised.

The experiments were performed as follows:

1. The wavelength is set using the OPA. The power is measured and tuned according to the absorption spectrum to avoid burning the sample.
2. The quarter-wave plate is set to one of the three polarisation positions.
3. The sample is saturated in a given direction (↑ or ↓) by sliding the permanent magnet, making sure not to touch or move the sample.
4. A background image of the initial saturated magnetisation state is taken.
5. The pump shutter is opened and the laser beam is swept across the sample and back to its initial position.
6. The final magnetisation state is imaged.
7. Steps 3 to 6 are repeated for the opposite initial magnetisation state.

[6]Emmanuel Héré Competence Center, Institut Jean Lamour, Nancy F-54000, France

8. Steps 2 to 7 are repeated for all three polarisations.

9. Steps 1 to 8 are repeated for every wavelength in the range of interest, usually with a greater density of points near the plasmonic resonance in order to resolve any relevant features.

5.4.2 Post-processing

The measurement data were analysed to extract the final partial switching levels. First, the illumination was corrected by normalising the grey levels of all images so that the average grey level of a bare substrate region coincided for all images. Next, the magnetic contrast of images showing the final magnetisation state was normalised using the difference between images of the two opposite saturated states. To avoid any local division by zero, the background difference was smoothed with a Gaussian filter. To increase the signal-to-noise ratio, the contrast levels were averaged along the direction of laser sweeping, resulting in a cut-line of the region of interest (ROI) of the device, as illustrated in Figure 5.5. In this representation, a plateau is observed, corresponding to laser fluences that yield the same magnetic contrast. The final contrast levels are independent of the initial magnetisation and depend solely on the polarisation of the pump. For a given polarisation, both saturated states partially switch to the same magnetic contrast for fluences above a certain threshold.

Furthermore, the observed AO-HDS effect is symmetric, which is consistent with the symme-

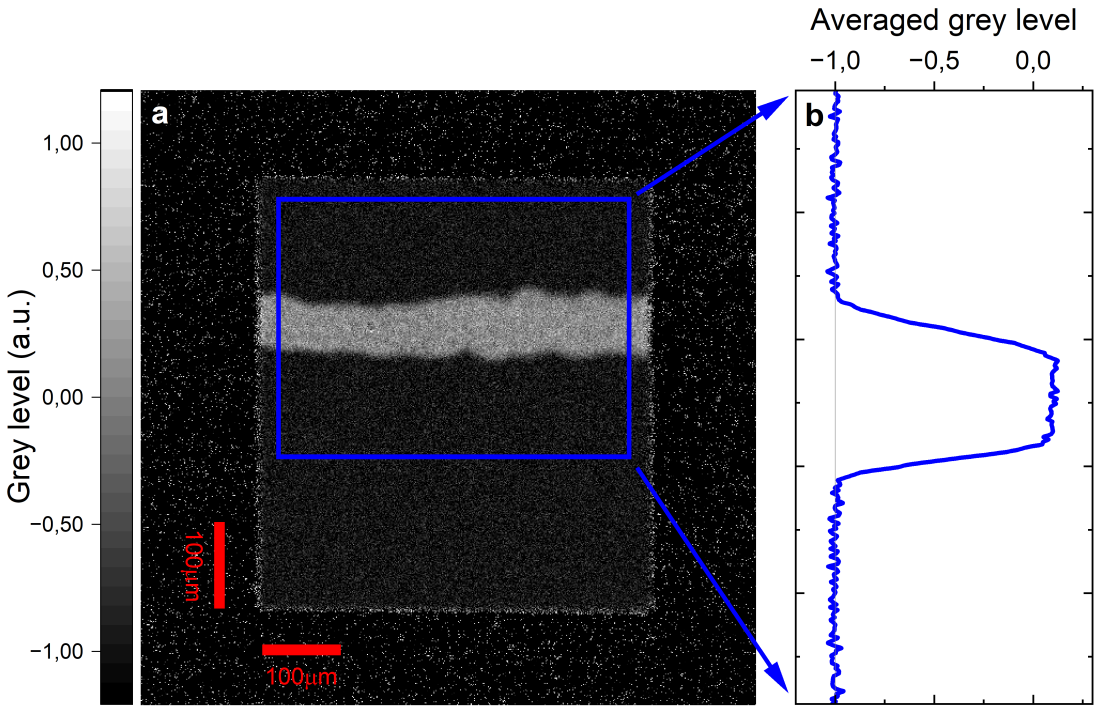

Figure 5.5: (a) Typical image normalised magnetic contrast obtained after laser sweeping. The scale bars indicate 100 µm. (b) Average grey-level cut-line of the region of interest. Signal after averaging along the horizontal direction, parallel to the laser sweeping direction. The data was recorded on sample 945_1c ($[Co/Pt]_1$), structure C2, saturated P-, swept with a 990 nm pump with the quarter wave-plate set at 315°.

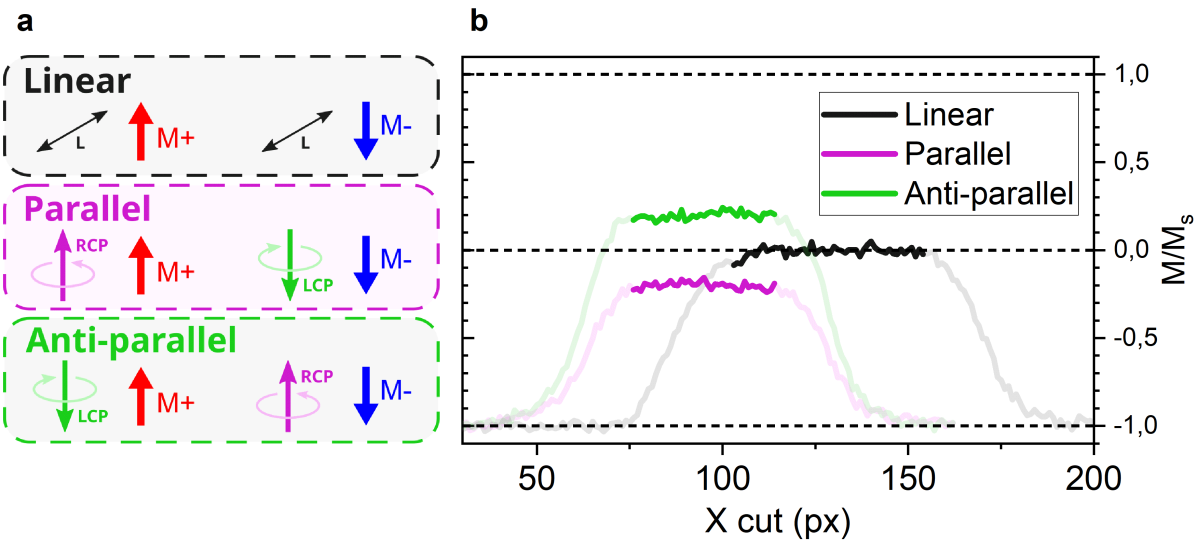

Figure 5.6: (a) Grouping of data based on the symmetry of initial magnetisation state and light polarisation combinations. (b) Example of averaged cut-lines and extracted plateaus for the different combinations.

try of the system. The results can therefore be grouped as follows: both initial states for linear polarisation are grouped, while the circular polarisations are grouped depending on whether the magnetisation is parallel or anti-parallel to the angular momentum of light, as illustrated in Figure 5.6 (a). The grouped cut-lines are then aligned and subtracted from each other. The resulting cut-lines exhibit plateaus that are extracted and averaged to produce the final partial switching values, as shown in Figure 5.6 (b). This procedure is repeated for all measured wavelengths to yield the AO-HDS spectra discussed in the next section.

5.5 Results

5.5.1 All-optical helicity-dependent switching spectra

To study the impact of plasmonic resonances on AO-HDS, the previously described protocol was applied at wavelengths from the visible to the near-infrared range.

For sample 1026_2 ($[Co/Pt]_{10}$) and periodic structure A2 (P = 470 nm and D = 160 nm), the measured AO-HDS spectra are plotted in Figure 5.7. No change of sign is observed, and the maximum effect occurs around 1100 nm. This wavelength does not correspond to either the plasmonic resonance or the maximum MCD amplitude. Switching seems to disappear at the diffraction order and at shorter wavelengths. These results may be explained by the fact that the magneto-optical spectra were measured in a fully saturated state, where all nanodisks were magnetised in the same direction. The surface lattice resonance, being a collective effect, may lose its impact on the MO response in a demagnetised state or when adjacent disks have different magnetisation directions. Since AO-HDS usually relies on multiple laser pulses, the first few pulses may create a non-uniform magnetisation distribution, suppressing the effect for subsequent pulses. In this scenario, only individual disk resonances remain relevant. The disappearance of AO-HDS at the diffraction order and at shorter wavelengths can also be attributed to diffracted beams that emerge when the wavelength is smaller than the diffraction edge. These beams carry

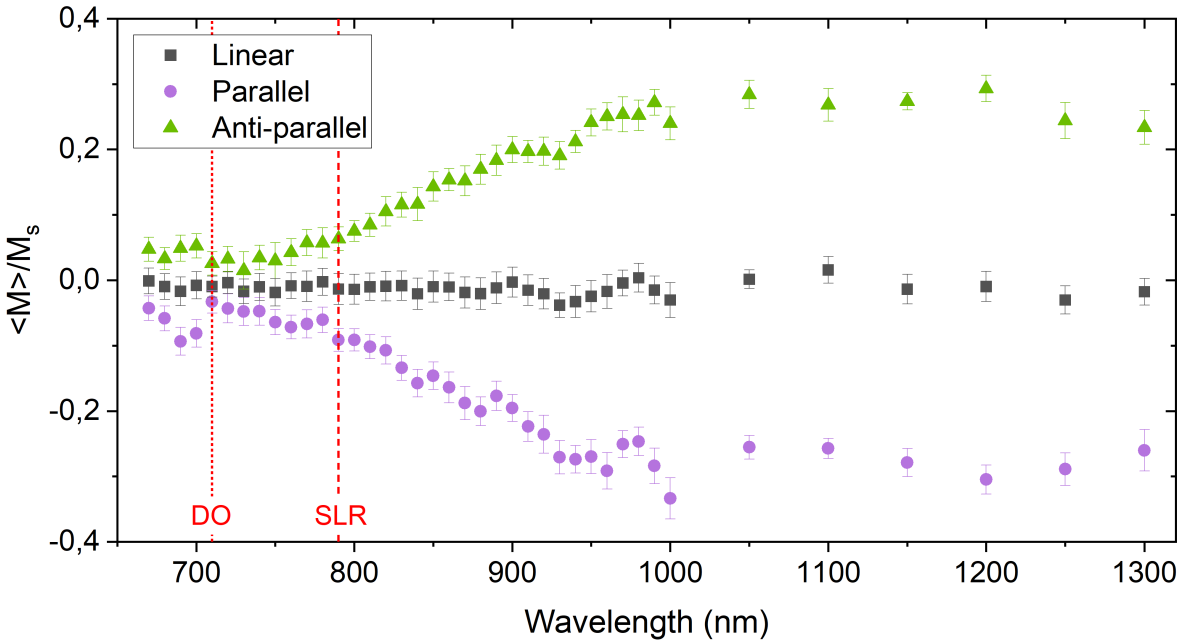

Figure 5.7: AO-HDS spectra for sample 1026_2 ($[Co/Pt]_{10}$), with periodic structure A2 (P = 470 nm and D = 160 nm). The red dashed lines indicate the wavelength of the diffraction order and the SLR wavelength, respectively.

their own rotation and ellipticity [132], [133], potentially dispersing the angular momentum that would otherwise interact with the system. Most samples patterned into periodic arrays showed similar behaviour, with a maximum switching occurring in the near-infrared.

Having realised that magneto-optical lattice resonances are ill suited to enhance AO-HDS, the attention is now on the magneto-plasmonic resonance of individual disks. In order to obtain large enough signals, the impact of those resonances is studied in aperiodic nanodisk arrays with similar packing factor than the periodic arrays.

Measurements on randomly distributed nanodisks (R1350) from the same multilayer stack (sample 1236) are presented in Figure 5.8 (b). In this case, the AO-HDS effect exhibits a sign change. However, the wavelength at which this occurs does not coincide with the zero crossing of the MCD effect. This sign change can not be explained by the IFE, as the net magnetisation induced by IFE does not change direction with wavelength. Therefore, neither MCD nor IFE by themselves fully account for the measured AO-HDS behaviour.

The relative contributions of MCD and IFE can be evaluated by taking a linear combination of the MCD and absorption spectra. This approach shifts the zero crossing of the combine effect, with the direction of the shift depending on the relative sign of the absorption contribution. A good agreement between this linear combination and the measured AO-HDS spectra is found, with the decomposition into MCD and absorption (IFE) contributions shown in Figure 5.8 (a). It shows that the maximum amplitude of the MCD contribution, located at about 1100 nm, is two to three times larger than the IFE maximum contribution. This is further illustrated at the LSPR wavelength at 640 nm, where MCD is expected to be zero while IFE is maximal. At this wavelength, less than a 5 % switching is observed, compared to 15 % switching near the wavelength of maximum MCD contribution.

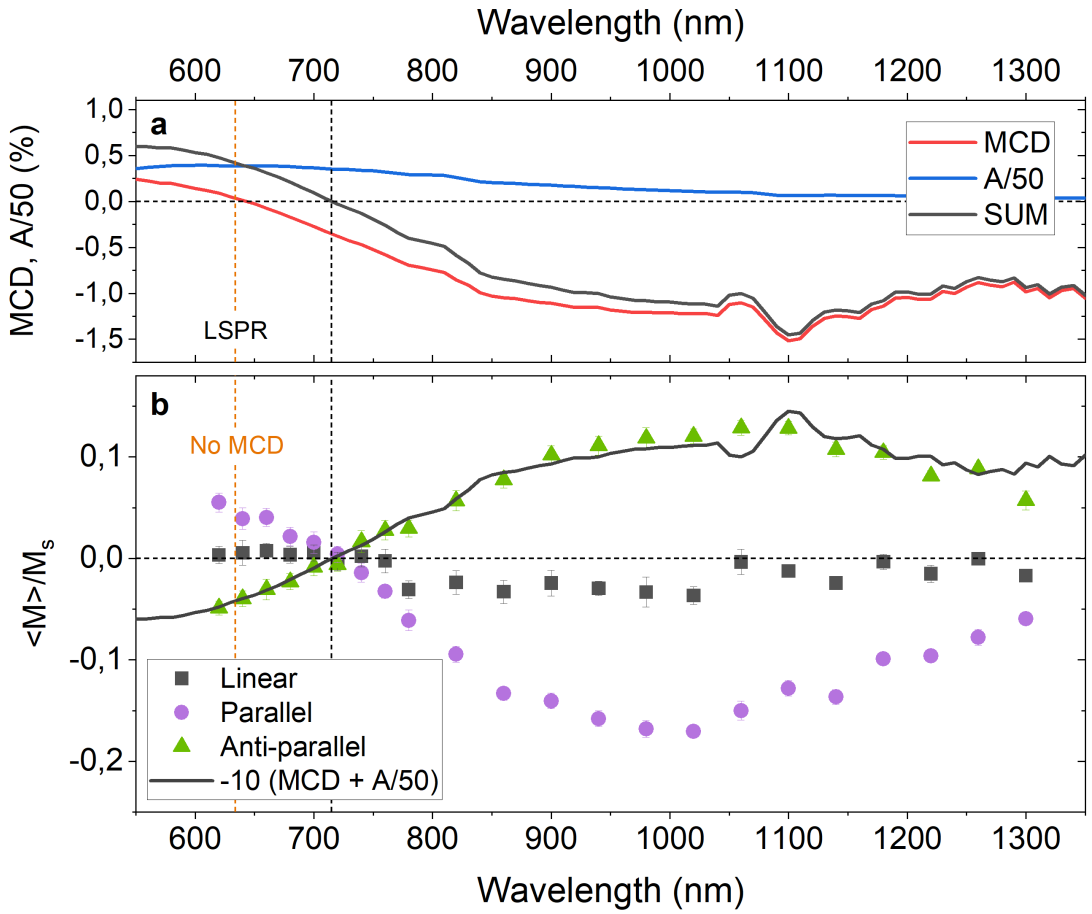

Figure 5.8: Compilation of results for sample 1236 ($[Co/Pt]_{10}$) with randomly distributed nanodisks (R1350) (D = 170 nm). (a) Measured MCD and scaled absorption spectra. (b) AO-HDS spectra. The orange dashed line indicates the zero crossing of MCD. The black dashed line corresponds to the zero crossing of the sum of the response. The solid black line in (b) is a linear combination of the MCD and absorption (IFE) spectra.

5.5.2 Pulse duration dependence

To further study AO-HDS in magneto-plasmonic structures, measurements were conducted as a function of pulse duration. For this, the main output of the 1030 nm laser was used, and the integrated compressor allowed tuning of the pulse duration. Two sample with similar periodic structures but different numbers of Co/Pt repetitions were measured: sample 945_1c ($[Co/Pt]_1$), array C2 (P = 470 nm and D = 250 nm) and sample 1026_2 ($[Co/Pt]_{10}$), array A2 (P = 470 nm and D = 160 nm). The results of the pulse duration dependence are presented in Figure 5.9. The most striking difference between these results and those obtained on continuous films (see Figure 4.7) is that the maximum pulse duration applicable for AO-HDS is longer than the maximum experimentally attainable value of 13ps. This finding highlights the fundamental difference between AO-HDS on granular media/uniformly magnetised nanodisks and continuous films. For the former, AO-HDS originates solely from different transition rates for oppositely magnetised grains/disks and is only limited by the condition that the ellipticity of the light has an impact on those rates. In contrast, the convergence of the thresholds for switching and multidomain formation limits the maximum pulse duration in these films. Analogous to the case

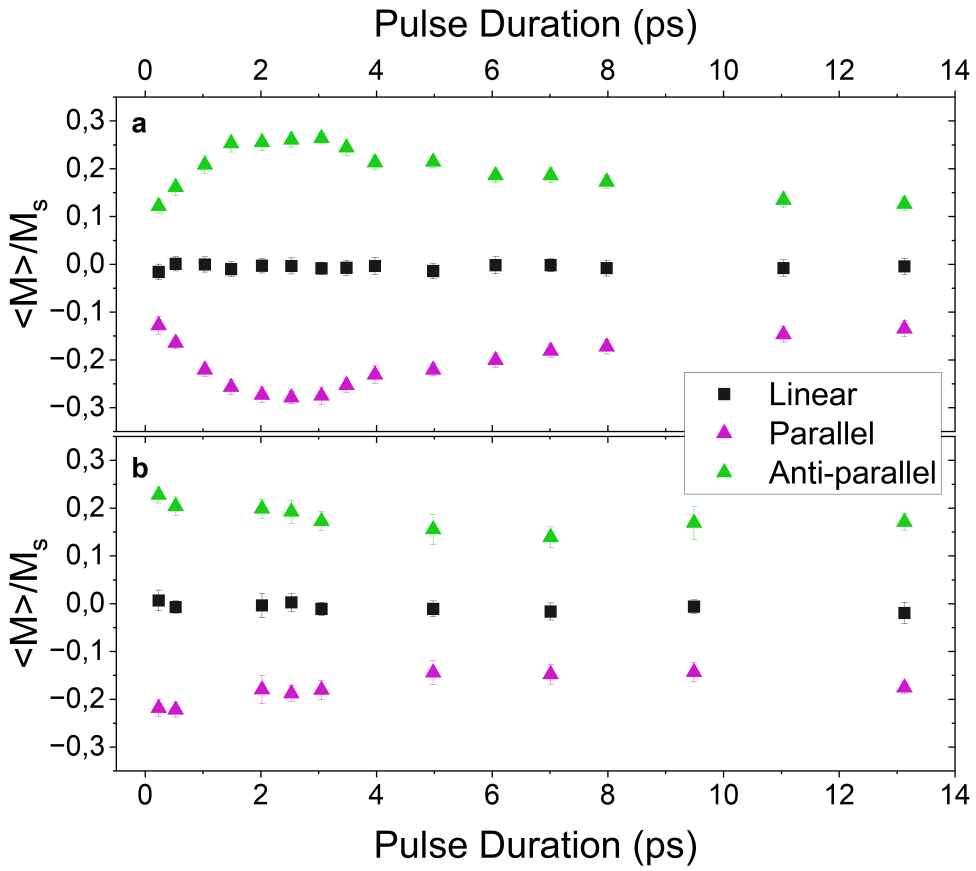

Figure 5.9: Dependence of partial switching on laser pulse duration. (a) Sample 945_1c ($[Co/Pt]_1$), array C2 (P = 470 nm and D = 250 nm). (b) Sample 1026_2 ($[Co/Pt]_{10}$), array A2 (P = 470 nm and D = 160 nm).

of helicity independent switching of GdFeCo films[40], this finding indicates, that the maximum pulse duration applicable for thin films is not limited by a breakdown of the underlying reversal mechanism itself but by delayed thermally activated multidomain formation driven by dipolar fields. A closer comparison between the results obtained for disks made of different material reveals slight differences between the pulse length dependencies of their AO-HDS efficiencies. Sample 945_1c shows a noticeable maximum AO-HDS efficiency around 2.5 ps, whereas sample 1026_2 shows a slight decrease from its maximum at 300fs to an almost constant value for $\tau_p \geq 3$ ps, as seen in Figure 5.9. The different behaviours are most probably related to distinct temperature dependencies of their magnetic properties that govern the transition rates.

5.5.3 Power dependence

Power-dependent experiments were carried out to characterise the fluence threshold of partial magnetic switching. Figure 5.10 (a)-(d) shows the results for sample 1026_2 ($[Co/Pt]_{10}$), array A2 P = 470 nm and D = 160 nm).

A gap in fluence threshold is observed between measurements performed with linear and circular polarisation. The data suggest that the system demagnetises at a lower fluence under linear polarisation compared to circular polarisation. This finding is surprising since one would expect that the total absorbed power should be similar for all polarisations, with slightly (less

than 1%) smaller/larger values for right/left handed circular polarisation due to MCD. The optical induced temperature rise and the induce IFE field do not depend on the total absorbed energy but the local absorbed energy density. Therefore, the observed gap might be related to differences in the spatial distribution of absorbed energy. Simulations show that near the resonance, the absorbed power density is differently distributed for linear and circular polarised light, as illustrated in Figure 5.10 (f)-(g). For linear polarisation, two hot spots form at the edge of the disk along the direction of polarisation. In contrast, circular polarisation generates four lower-amplitude hot spots at the disk edge. The higher local absorption for linear polarisation can induce local demagnetisation, which may trigger reversal of the disk magnetisation at a lower fluence.

Figure 5.10 also highlights absorption enhancement induced by the plasmonic resonance. Depending on whether the laser wavelength is on- or off-resonance, the fluence threshold can double or even triple. This difference is only due to absorption, as illustrated in Figure 5.10 (e), where the demagnetisation induced by linear polarisation is plotted as a function of the absorbed fluence. The absorption coefficients used for this correction are taken from the absorption spectrum shown in the inset. After correcting for absorption, the demagnetisation curves for linear polarised light align closely.

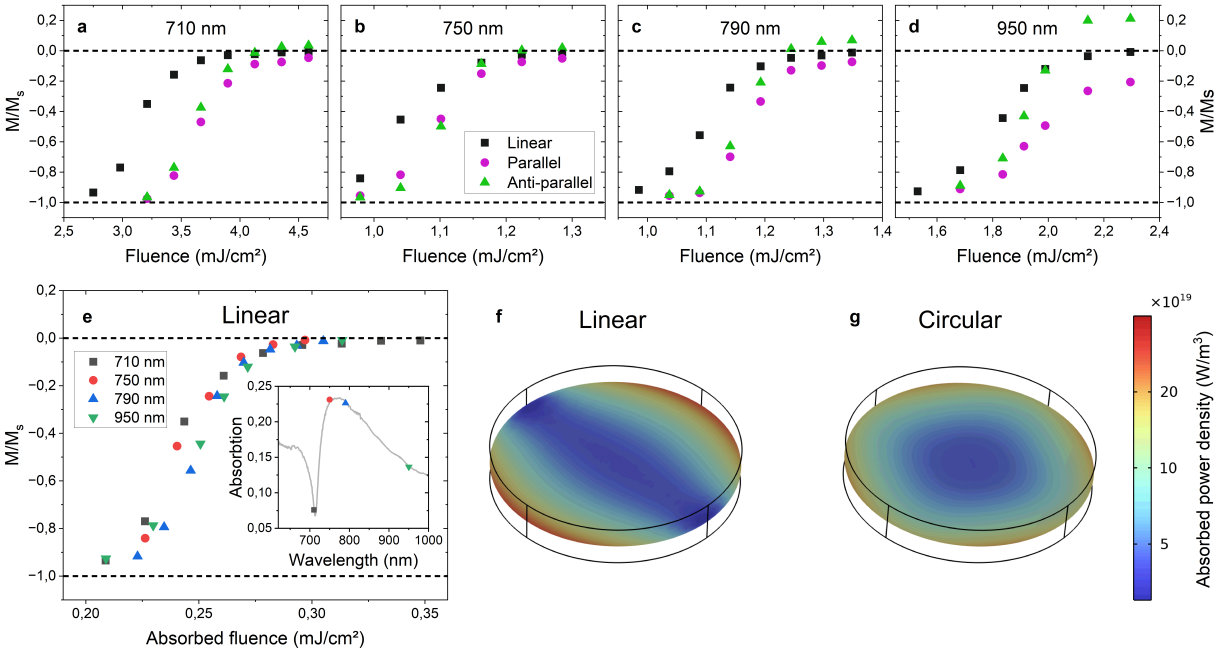

Figure 5.10: (a)-(d) Dependence of AO-HDS on laser fluence for sample 1026_2 ($[Co/Pt]_{10}$), array A2 (P = 470 nm and D = 160 nm) for different configurations and wavelengths: (a) 710 nm, (b) 750nm, (c) 790nm and (d) 950nm. (e) Same data for linear polarisation but plotted versus the absorbed fluence. The insert shows the absorption spectrum of the array. Relevant wavelengths are highlighted with symbols. (f)-(g) Simulated distribution of the absorbed power density for (f) linear and (g) circular polarised light at a wavelength of 710 nm.

5.6 Discussion

The results on AO-HDS in Co/Pt nanodisks provide several important insights. The optical and magneto-optical spectra were successfully engineered to exhibit a resonance at a chosen wavelength, using relatively simple designs. More complex plasmonic structures could be used to further optimise the response. Additionally, composite stacks combining magnetic materials and plasmonic metals, could enhance the plasmonic potential even further. Periodic arrays, however, reveals some of the limitations with the use of plasmonic resonance for AO-HDS. Collective magnetic effects, such as the surface lattice resonance–induced enhancement of the magneto-optical response, do not survive the switching process because the magnetisation does not remain uniform. Magnetic force microscopy measurements of the final states confirm that the nanodisks mainly support fully saturated magnetisation states and are not significantly magnetically coupled through the dipolar fields (see Annexe D). Consequently, the resonance of individual disks remains dominant, and the observed maximum switching amplitude is likely a result of the MCD of individual nanodisks.

The observed partial switching can be linked to the results of Huang et al.[48], discussed in Chapter 1. In their study, magnetisation jumps associated with the nucleation regime exhibit an equilibrium magnetisation point, where the amplitude of the jump is zero. At this point, the transition rates between magnetisation states are equal. The measured equilibrium magnetisation of approximately 20% is of the same order of magnitude as the maximum final magnetisation states observed in this chapter. In particular the pulse length dependent measurements performed on sample 945_1c (Figure 5.9 (a)) show a partial switching of approximately 25% at 2 ps for comparable Co/Pt multilayer and pulse duration as the one used in this paper. This agreement suggests that the AO-HDS measurements presented here primarily probe the impact of MCD and IFE on helicity-dependent nucleation occurring on short timescale. These observations also highlights the critical role of the micromagnetic relaxation (domain wall motion) in achieving complete switching in continues films. In its absence, as in the magneto-plasmonic systems studied in this chapter, only partial switching is observed, reinforcing the importance of both nucleation dynamics and subsequent relaxation processes in AO-HDS.

Chapter 6

Arbitrarily shaped laser spot characterisation technique

In this chapter, an extension of J. M. Liu's technique to characterise pulse laser spots is presented. This approach allows the visualisation and fitting of an arbitrary laser intensity distribution beam. After detailing the principle behind the method and its implementation, results will be presented for both common and non-trivial spot shapes.

6.1 Theoretical principles

A beam's shape is described by its normalised fluence distribution function $f(\mathbf{r})$ such that, for any vector $\mathbf{r}$ in the plane normal to the beam propagation direction, the fluence of the beam is:

$$F(\mathbf{r}) = F_0 \cdot f(\mathbf{r}) \tag{6.1}$$

With F_0, the peak laser fluence. The area of the laser spot A_s is then defined as :

$$A_s = \int_{-\infty}^{+\infty} \int_{-\infty}^{+\infty} f(\mathbf{r}) dx dy = 2\pi \int_0^{+\infty} r f_r(r) dr \tag{6.2}$$

With $r = |\mathbf{r}|$ and $f_r(r)$ the radial distribution defined as the azimuthal average of $f(\mathbf{r})$:

$$f_r(r) = \frac{1}{2\pi} \int_0^{2\pi} f(r, \phi) d\phi \tag{6.3}$$

The pulse energy, defined as the integral of the fluence over the whole normal plane, can therefore be linked to laser spot area through the relation:

$$E_p = \int_{-\infty}^{+\infty} \int_{-\infty}^{+\infty} F(\mathbf{r}) = F_0 A_s \tag{6.4}$$

Given a threshold fluence F_{th}, the threshold pulse energy E_{th} is the minimum pulse energy such that there exists a vector $\mathbf{r}$ where $F_{th} = F(\mathbf{r})$. This corresponds to $F_{th} = F_0$ and equation 6.4 directly gives:

$$E_{th} = F_{th} A_s \tag{6.5}$$

Now considering all vector $\mathbf{r}_{th}$ such as $F(\mathbf{r}_{th}) = F_{th}$ with $F_{th} \leq F_0$, using equations 6.4 and 6.5, equation 6.1 can be rewritten as :

$$\frac{1}{E_p} = \frac{1}{E_{th}} \cdot f(\mathbf{r}_{th}) \tag{6.6}$$

If a phenomenon occurring above a fixed threshold fluence F_{th} is now considered, then for a given pulse energy E_p, the vectors $\mathbf{r}_{th}$ in equation 6.6 are the points delimiting the affected and unaffected region. Plotting $1/E_{th}$ vs $\mathbf{r}_{th}$ yields an image of the fluence distribution function $f(\mathbf{r})$ of the laser spot scaled by $1/E_{th}$.

The previous approach, based on J. M. Liu's technique [122], relied on the inversion of the fluence distribution function to obtain a fit model for $|\mathbf{r}_{th}(E_p)|$. This had the downside of only working for reversible functions, and since only the radial distribution is considered, any azimuthal information is lost. Using this new approach, any beam shape can be reconstructed, and if an analytical description exists, the fluence distribution can directly be fitted.

6.2 Practical implementation

There are a few phenomena that allow the implementation of this approach. However, some processes are irreversible or inconvenient to automate. For this implementation, all optical helicity-independent switching in GdFeCo alloys is chosen, as it is reversible and easy to initialise the sample by applying a magnetic field. AO-HIS is characterised by the toggle switching of the magnetisation in regions where the fluence of the laser pulse exceeds a threshold fluence F_{sw}. In

AOS studies, this approach has the added benefit of extracting the switching threshold fluence from the fitting of the fluence distribution.

To demonstrate this method, the femtosecond laser setup described in the Methodology chapter (page 51) was used, with minor additions and changes. First, to compare the obtained *in-situ* beam shape with an *ex-situ* approach, a set of flipper mirrors was added to redirect the beam onto the camera sensor, allowing for easy switching between both configurations. In this configuration, several neutral densities, equivalent to an ND 8.0, were inserted in the pump path before the camera to protect it from laser-induced burning. The paths were adjusted so that the focal plane of the focusing lens corresponds to the plane of the sample and the plane of the camera sensor. In this way, both the sample and the camera sensor are exposed to identical fluence distributions. To do so, the sample is first brought into focus by either finding the lens position that minimises the energy needed to burn the sample or by fixing the pulse energy above the AO-HIS switching energy and finding the lens position that maximises the switched area. After that, the flipper mirror and NDs are inserted, and the camera position is adjusted to be in the focal plane by minimising the spot size. A sketch of the setup is shown in Figure 6.1.

Similarly to the state diagram procedure described previously, imaging was performed using the LED as the light source, while the main laser output was used as the pump. The pump power is set through the motorised half-wave plate. The pulse energy is calculated from the power and the laser repetition rate. The pulse energy is swept from the threshold energy to the highest possible value without burning or altering the sample. This restricted span highlights one of the limitations of this technique, as the laser pulse shape can only be reconstructed within the range where $f(\mathbf{r}) \leq F_{th}/F_0$. This limitation can be alleviated by fitting a theoretical, analytical

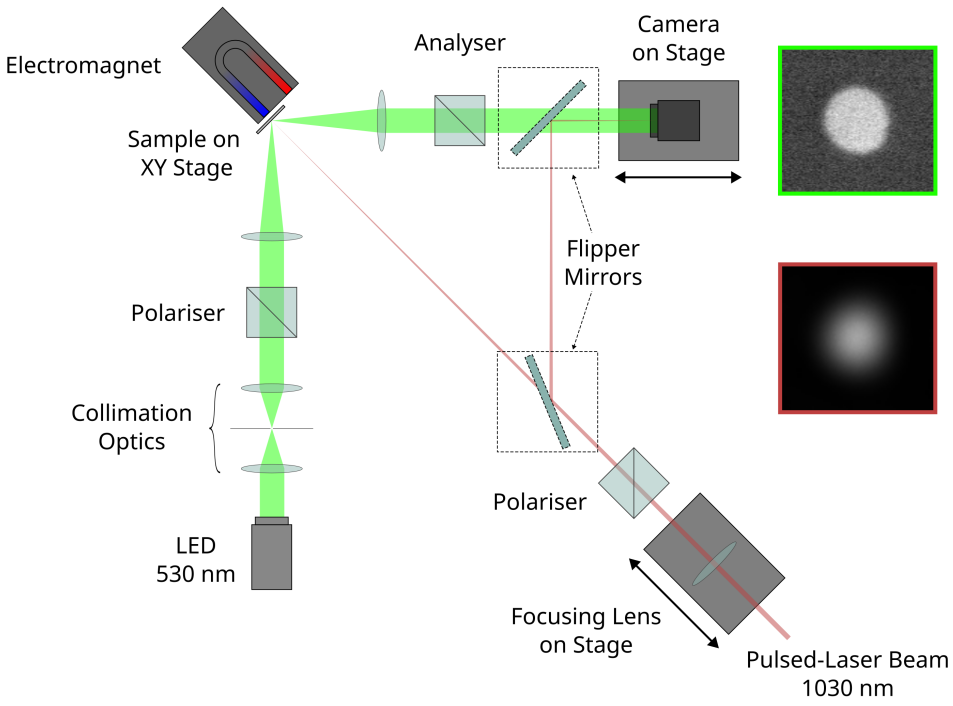

Figure 6.1: Sketch of the implemented setup. The insets show examples of *in-situ* induced domains (green frame) and the *ex-situ* intensity distribution imaged by the camera (red frame). Images are not to scale.

fluence distribution to the data in this limited range and extrapolating the fluence outside of that range from the model. Another complication arises from the appearance of a multi-domain state above a certain threshold. In the case of simple beams, this can be resolved by checking if the contours correspond to an area that was already switched at lower pulse energy.

For each power, the sample was saturated, a background of the initial state was taken, a single femtosecond laser pulse was sent, and the image of the resulting magnetic state was saved. This sequence is repeated a few times for each initial magnetisation state. After that, the flipper mirrors and the ND filters are put in place to image the spot directly on the camera.

The recorded data set was analysed in the following way: the grey levels of each image are normalised between 0 and 1 using the background images. The contours of the switched regions contours were extracted with a threshold at half the normalised contrast (0.5). Due to laser pointing instability, the reversed area position may fluctuate; therefore, the contours need to be centred either by considering them as close to circularly symmetric around a common point or by maximising the overlap between the resulting fluence distribution reconstruction from the contour and the directly imaged laser spot. Plotting $1/E_p$ versus the obtained contours gives a direct visualisation of the spot shape. Note that the density of energies is inversely proportional to the density of levels of the spot shape reconstruction. It is, therefore, advised to take more points at low pulse energy if some sharp features are present near the peak of the fluence distribution.

If the fluence distribution can be approximated as circularly symmetric, centred around the beam's centre, then a simpler approach can be used. In this case, Equation 6.6 becomes:

$$\frac{1}{E_p} = \frac{1}{E_{th}} . f_r(r) \tag{6.7}$$

The image normalisation and contours extraction remain the same as before, but equivalent radii are calculated from the contours:

$$r_{eq}(E_p) = \sqrt{A_c/\pi} \tag{6.8}$$

With A_c, the area enclosed by a contour. Plots of $1/E_p$ vs these radii will directly give the spot profile. Note that for some beam shapes, multiple concentric contours and, therefore, radii, can correspond to a given pulse energy.

6.3 Examples

The application of this technique is demonstrated through the characterisation of a few common pulse shapes: Gaussian, Laguerre-Gauss and Bessel-Gauss. These examples illustrate the strengths and limitations of this new approach.

6.3.1 Gaussian beam

One of the most commonly used beam shapes is the Gaussian beam, as it is the usual beam shape emitted by lasers. It remains Gaussian after passing through most optical elements. Its fluence distribution is characterised by a 2D axis-symmetric Gaussian function:

$$F_G(r) = F_0 e^{-\left(\frac{r}{\sigma}\right)^2} \tag{6.9}$$

With F_0 the peak fluence and σ the Gaussian width. This function is invertible (see equation 3.9), which is the basis of the Gaussian spot measurement technique developed by J. M. Liu [122].

Nevertheless, Liu's technique fails to capture any defects introduced by optical aberrations that would make the beam shape deviate from its ideal description.

To generate such fluence distribution, the pump beam was focused onto the sample surface using a 1 m planoconvex lens. The previously described procedure was performed to reconstruct the beam shape from the switched contours. The flipper mirror and filters were then used to record the intensity distribution on the camera in continuous emission, 100 kHz pulsed train mode.

The results are illustrated in Figure 6.2 (a) and (b). The *in-situ* reconstitution shows excellent agreement with the *ex-situ* direct imaging. This is accentuated in Figure 6.2 (c), which shows some contours from both techniques after proper normalisation. The imperfection of the beam is captured correctly by both approaches as a slight three-fold symmetric distortion.

Alternatively, assuming the radial distribution follows Equation 6.9, the contour's equivalent radius can be calculated using Equation 6.8. When the $1/E_p$ is plotted against these radii, as done in Figure 6.3, the resulting curve can be directly fitted with the analytical radial distribution $f_r(r)$ as shown in equation 6.7. This approach allows the retrieval of the threshold fluence F_{th} and the Gaussian width σ with high precision.

Note that since this first measurements, the used sample has aged, and a new sample was fabricated for the continuation of this work. A quick calibration was performed using a Gaussian beam, and the procedure was used to determine the switching threshold fluence,

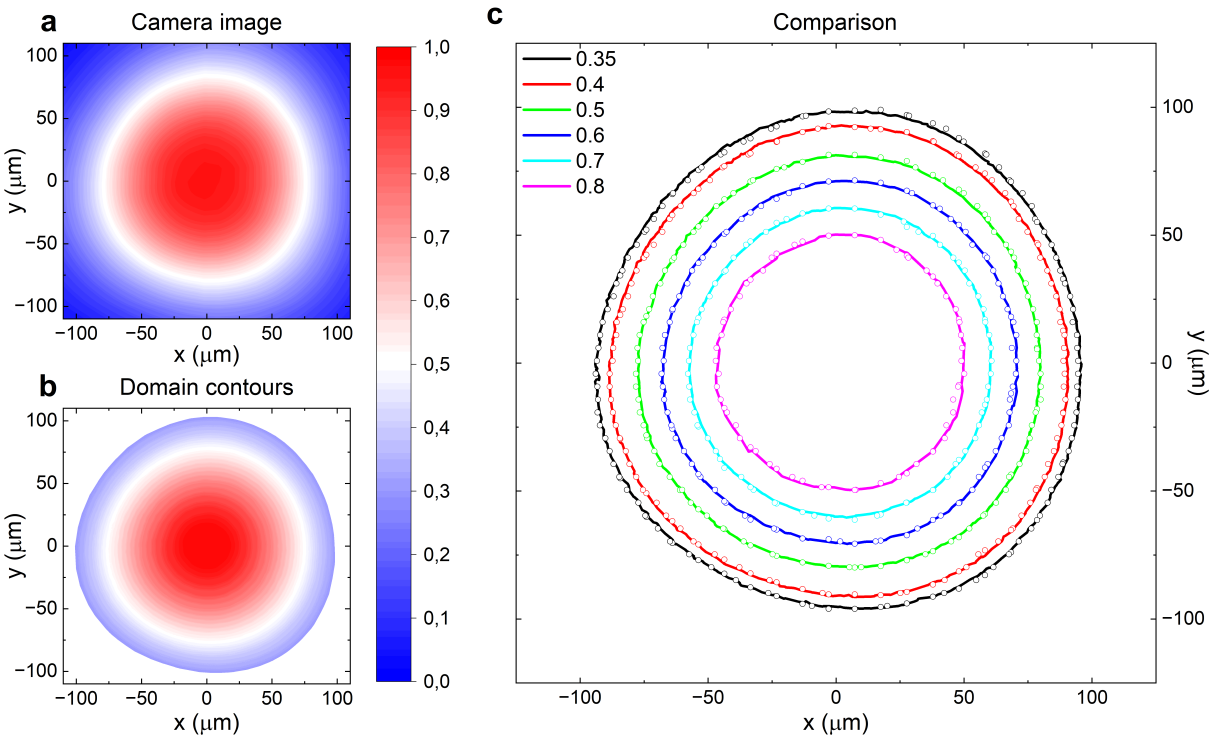

Figure 6.2: Beam reconstruction results for Gaussian beam. (a) *Ex-situ* intensity distribution obtained through direct imaging by the camera. (b) *In-situ* reconstruction of the fluence distribution. (c) Comparison of contours from domains (lines) and direct imaging by the camera (symbols). The colour scale and legend values correspond to F_{th}/F_0 for the domains and I/I_{max} for the camera images.

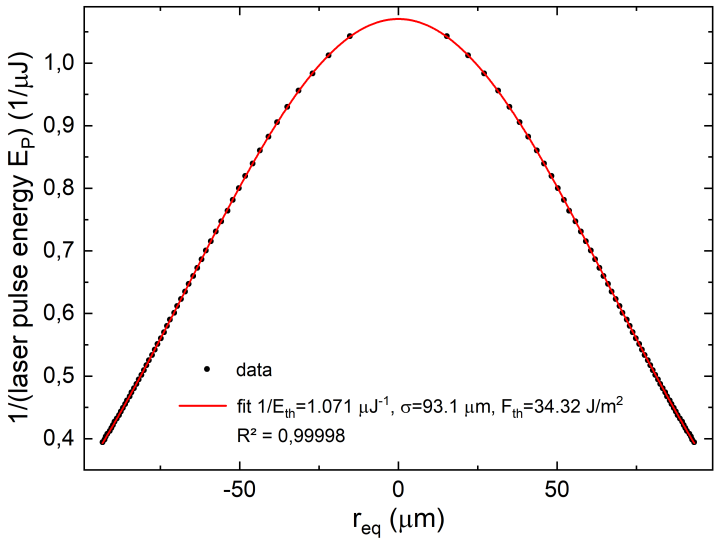

Figure 6.3: $1/E_p$ vs r_{eq} for Gaussian beam induced domains. The red line corresponds to a fit to the data using Equation 6.7. The fit parameters $1/E_{th}$, σ and the derived value F_{th} are given in the legend.

$F_{th} = 27.80\text{J/m}^2$. This threshold value will be used as reference for the other beam shapes presented in this chapter.

6.3.2 Laguerre-Gauss beam

Laguerre-Gauss beams are of interest as they can carry orbital angular momentum (OAM) and have been used in various applications, such as optical tweezers, among others. For this example, only a Laguerre-Gauss beam of radial index $p = 0$ and of azimuthal index $l = 1$ is considered. In the focal plan, this beam's fluence distribution is described by the following axis-symmetric

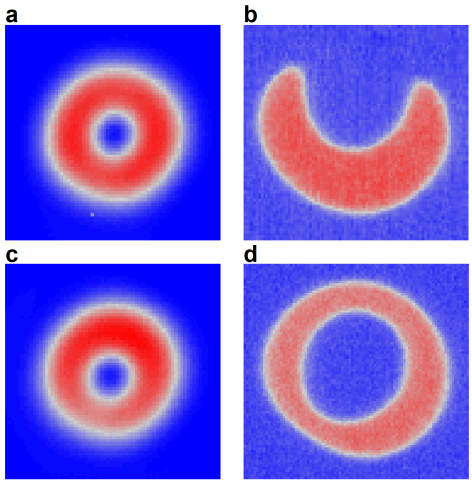

Figure 6.4: Vortex wave plate alignment mismatch between the direct intensity image (a),(c) and the induced switched domain (b),(d) when aligned with the direct camera image at a repetition rate of 100 kHz (a)-(b) and with the single-pulse induced switched domain (c)-(d)

function:

$$F_{LG}(r) = F_0 e^1 \left(\frac{r}{\sigma}\right)^2 e^{-\left(\frac{r}{\sigma}\right)^2} \tag{6.10}$$

With F_0 the peak fluence and σ the Gaussian width. This function cannot be inverted, meaning that Liu's technique can not be applied.

To obtain the beam shape, a spiral vortex wave plate (Vortex Photonics, V-1030-20-1) was inserted into the pump beam path before the focusing lens. The alignment of the plate is critical, as any slight deviation will result in an asymmetric fluence distribution. Such issues were encountered during the first attempts. The heating of the optical elements in continuous laser pulse train mode, used to image the beam directly on the camera, is sufficient to induce pointing direction changes, causing a misshaped beam. This led to different vortex wave plate's alignments for *ex-situ* and *in-situ* measurements as illustrated in Figure 6.4. To minimise this mismatch, the laser repetition rate was lowered to 1 kHz and 11 pulses were sent to induce the switched domains used for *in-situ* fluence reconstruction.

Using these new conditions, the vortex wave plate was aligned to achieve as close to an axisymmetric intensity distribution on the camera as possible before following the *in-situ* measurement procedure. The resulting distribution is shown in Figure 6.5. Again, the agreement between both approaches is striking. The slight asymmetry causing some unclosed circles is properly captured.

By assuming an axisymmetric distribution, the equivalent radius of both the inner and outer contour delimitations are retrieved from their enclosed area. The plot of $1/E_p$ vs these radii is shown on Figure 6.6. The theoretical fluence distribution (Equation 6.10) is used to fit the data. The threshold fluence extracted from this fit is $F_{th} = 26.3\text{J/m}^2$, which is noticeably smaller than that of the Gaussian beam. Additionally, small deviations between the data points and fits are observed. This is explained by imperfections in the fluence distribution generated by the plate. By modifying the fitted fluence distribution with:

$$f_{LG,mod}(r) \simeq 2.4756 \left(\frac{r}{\sigma}\right)^{3/2} e^{-\left(\frac{r}{\sigma}\right)^{5/2}} \tag{6.11}$$

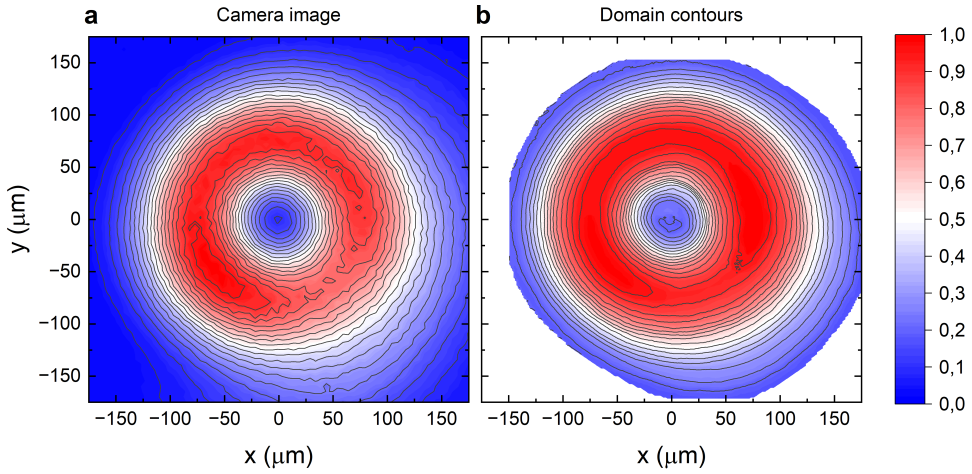

Figure 6.5: Results for the Laguerre-Gauss beam. (a) *Ex-situ* intensity distribution obtained through direct imaging by the camera. (b) *In-situ* reconstruction of the fluence distribution. The colour scale values correspond to F_{th}/F_0 for the domains and I/I_{max} for the camera images.

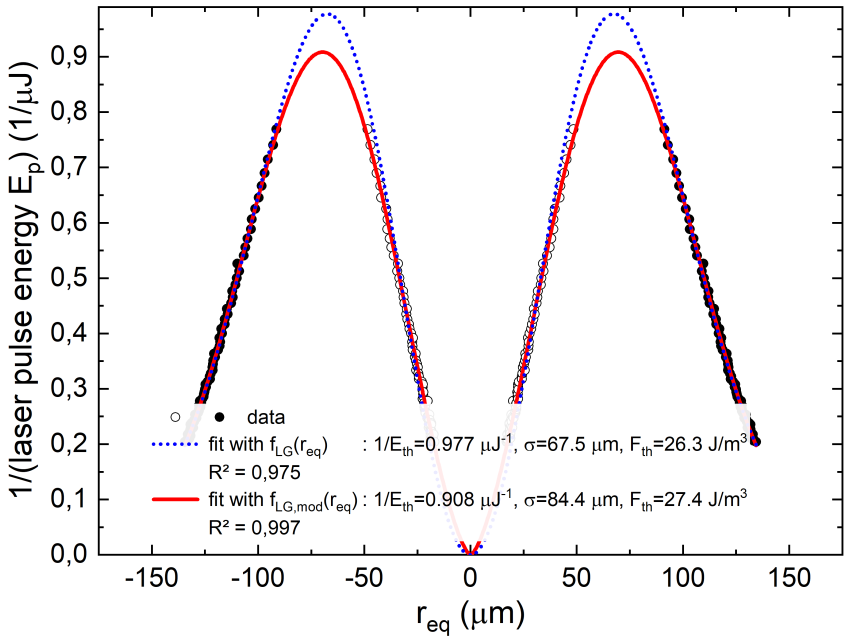

Figure 6.6: $1/E_p$ vs r_{eq} for the Laguerre-Gauss beam induced domains. The dashed blue line corresponds to the best fit to the data using the normalised Laguerre-Gauss fluence distribution. The solid red line corresponds to the best fit to the data using the modified Laguerre-Gauss fluence distribution (equation 6.11). The fit parameters $1/E_{th}$, σ and the derived value F_{th} are given in the legend.

a better fit is obtained as shown in Figure 6.6. The extracted threshold fluence is $F_{th} = 27.4\text{J/m}^2$, representing a 1.5% deviation from the reference threshold calculated for the Gaussian distribution.

6.3.3 Bessel-Gauss beam

Finally, a Bessel-Gauss beam fluence distribution is considered. These beam shapes are self-healing and non-diffracting. These properties make them useful in microscopy applications and as optical tweezers. This beam's fluence distribution can be described by the following axis-symmetric function:

$$F_{BG}(r) = F_0 J_0\left(\frac{r}{\sigma_B}\right) e^{-\left(\frac{r}{\sigma_G}\right)^2} \tag{6.12}$$

With F_0 the peak fluence, J_0 the zero-th order Bessel function, σ_B the Bessel width and σ_G the Gaussian width. Again, this function cannot be inverted, meaning that Liu's technique can not be applied. Equation 6.2 gives:

$$A_{BG} = \pi\sigma_G^2 I_0\left(\frac{\sigma_G^2}{2\sigma_B^2}\right) \tag{6.13}$$

With I_0 the zero-th order modified Bessel function.

To achieve this beam shape, a pair of axicons (Thorlabs, AX2520) was used. They were mounted before the focusing lens with their flat bases facing each other and separated by a 5 mm gap. After aligning the axicons through direct imaging by the camera, the procedure was

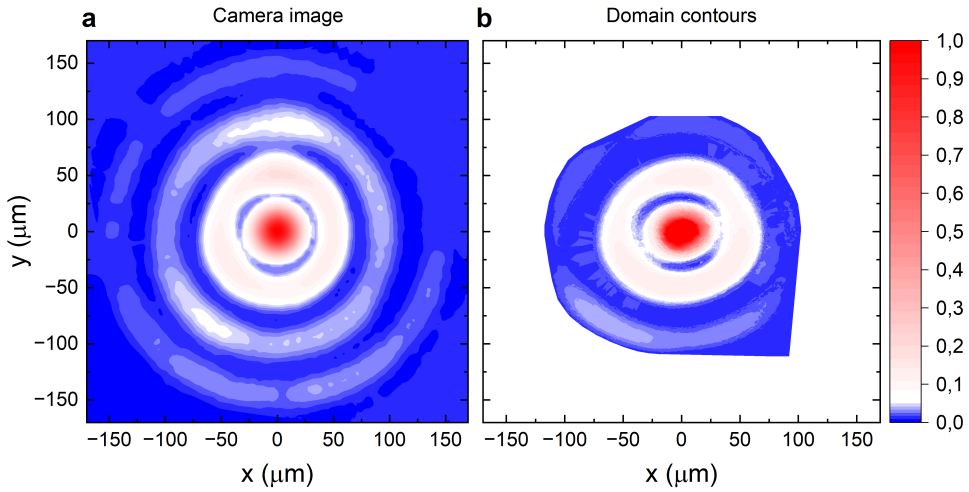

Figure 6.7: Results for the Bessel-Gauss beam. (a) *Ex-situ* intensity distribution obtained through direct imaging by the camera. (b) *In-situ* reconstruction of the fluence distribution. The colour scale values correspond to F_{th}/F_0 for the domains and I/I_{max} for the camera images.

repeated to reconstruct the beam shape. The resulting intensity distribution for both approaches can be seen in Figure 6.7. Both distributions seem to follow Equation 6.12, with a very intense peak in the middle surrounded by multiple rings of lower amplitudes characteristic of the Bessel function. A three-fold symmetric distortion can be observed in both approaches and may be due to some imperfection in the optics.

For high pulse energy, the beam locally modifies the properties or even burns the film in the centre. Due to this, the effective energy range is limited, and the side rings are not always closed. This vastly reduces the number of energy levels for which an equivalent radius for each ring can be calculated.

In that case, the 2D fluence distribution (Equation 6.12) was directly fitted to $1/E_p$ vs the switched contours points with $F_0 = 1/E_{th}$. This allows for a reasonable estimation of $1/E_{th}$ and σ_B but not of σ_G due to the limited spatial extent. To get σ_G, the normalised intensity distribution directly acquired by steering the beam on the camera using the flipper mirrors was fitted with the analytical normalised fluence distribution. From this fit, both σ_B and σ_G can be extracted, and using Equations 6.5 and 6.13, a threshold fluence of $F_{th} = 28.3\mathrm{J/m}^2$ can be calculated. This threshold is close to the reference threshold calculated for the Gaussian distribution. Note, if the threshold fluence is accurately known, for example from another beam shape, then Equations 6.5 and 6.13 would allow the extraction of σ_G without the need of the *ex-situ* measurements.

6.4 Discussion

The Laguerre-Gauss example shows some of the strengths of the technique. First, this *in-situ* approach allows to obtain the actual fluence distribution under experimental conditions, whereas other approaches may lead to differences caused by the measurement method.

Another advantage is the ability to easily extract parameters describing arbitrary fluence distributions and the possibility of extracting the threshold fluence. Threshold fluence extraction was also possible using Liu's technique, but only for a specific fluence distribution. The method presented in this chapter only relies on a model for the fluence distribution to extract this

threshold. The precision of the extracted threshold depends on how well the model represents the actual distribution. This provides some flexibility, as the model can be modified to better fit the data without considering if the function is invertible, unlike Liu's technique.

The Bessel-Gauss example demonstrates one of the drawbacks of this method. In practice, due to the finite usable range of pulse energy, only a fraction of the beam spatial extent can be directly measured. This range is limited by the maximum peak fluence and the threshold fluence. Low fluence features in the distribution may not be resolved or may cause damage in high-fluence regions, as was the case for the Bessel-Gauss distribution. If those features are essential for a good fit, this could lead to a significant discrepancy in the extracted parameters and threshold fluences.

Conclusion

English version

This thesis investigated the origin of all-optical helicity-dependent switching (AO-HDS) in Co/Pt-based magneto-plasmonic structures. Positioned at the intersection of ultrafast magnetism and magneto-plasmonics, this work advances the understanding of both fields.

The control of magnetisation on ultrafast timescales is a relatively recent and highly active research area with strong potential for fast, energy-efficient data storage and processing. While femtosecond laser-induced demagnetisation and all-optical helicity-independent switching have been extensively studied and are now relatively well understood, the origin of AO-HDS remains under debate. Two prominent mechanisms have been put forward by the community to explain the observed behaviour: magnetic circular dichroism (MCD) and the inverse Faraday effect (IFE). Their similar observable consequences make disentangling them particularly challenging. Yet, clarifying their respective roles is essential for optimising AO-HDS and enabling advanced systems that exploit ultrafast angular momentum transfer between light and magnetism.

Plasmonic systems, widely used across photonics, are natural candidates for investigating AO-HDS, as their ability to confine light enhances light–matter interactions. In magneto-plasmonics systems, plasmonic resonances can strongly modify magneto-optical responses, including MCD and IFE. Importantly, magnetisation shifts the plasmon resonance wavelength for opposite circular polarisations, producing a sign change in MCD near resonance, while the IFE is amplified at resonance through near-field confinement. This key difference provides a pathway to separate their contributions—an idea central to this thesis.

To explore this, Co/Pt multilayers were grown and patterned into magneto-plasmonic nanostructures, specifically randomly distributed nanodisks and periodic nanodisk arrays. The first configuration supports localised surface plasmon resonances determined by particle size and shape, while the second exhibits sharper surface lattice resonances arising from interparticle coupling. Structural parameters were characterised by atomic force microscopy and optimised to achieve resonances in the visible to near-infrared range.

Several measurement techniques were developed or improved to study AO-HDS in these systems. The method for measuring optical and magneto-optical spectra was revised, the femtosecond laser setup was automated to produce state diagrams of switching, and new post-processing techniques were introduced to characterise arbitrarily shaped laser spots. Specialised experimental protocols and analysis workflows were also established to properly normalise AO-HDS spectra in plasmonic devices.

Complementary simulations were carried out to interpret and reproduce experimental results. A 4×4 transfer matrix framework was expanded to handle magnetically layered systems and compute magneto-optical spectra, enabling the extraction of effective Voigt constants from experimental data. Finite-element simulations using experimentally determined permittivity tensors further allowed the optimisation of nanostructure geometries and the calculation of MCD and IFE spectra.

Measurements of Co/Pt multilayer films showed no spectral features in their magneto-optical response. Analysis of thickness dependence highlighted the role of reflectivity in MCD, demonstrating that conventional MCD derived from extinction spectra does not accurately represent the true absorption difference relevant for AO-HDS. Experiments on AO-HDS revealed a dependence on pulse duration and the number of Co/Pt repetitions, with thicker films showing reduced switching efficiency. However, no unambiguous spectral fingerprints linking AO-HDS to either MCD or IFE could be identified.

In patterned systems, both random and periodic nanodisk arrays exhibited clear plasmon resonances that were reproduced in simulations. Zero crossings in ellipticity and MCD spectra were observed near resonance. AO-HDS experiments demonstrated partial switching above a fluence threshold. For periodic arrays, no spectral zero crossings were detected in AO-HDS, likely because surface lattice resonances break down after only a few laser pulses. In contrast, randomly distributed nanodisks exhibited a sign reversal in AO-HDS spectra, consistent with an MCD contribution. However, the spectral shift of this zero crossing relative to the measured MCD spectrum suggests an additional IFE contribution. Unexpectedly, a difference in fluence thresholds between linear and circular polarisation was observed, which may be explained by mode-dependent hot-spot formation in the nanodisks.

In summary, this work demonstrates that helicity-dependent magnetisation control can be integrated into simple plasmonic structures, providing valuable insights into the interplay between MCD and IFE. The results highlight the potential of plasmon-enhanced AO-HDS for improving energy efficiency and advancing future opto-magnetic devices. Looking ahead, several directions emerge. Coupling magneto-plasmonic nanodisks with electronic devices—for example by fabricating them on Hall crosses—would enable time-resolved studies of multi-pulse switching dynamics. Another avenue is to exploit plasmon-enhanced MCD in materials exhibiting all-optical helicity-independent switching: a sufficiently large MCD could shift the switching fluence threshold depending on the initial magnetisation, enabling deterministic control with a single circularly polarised pulse.

Version française

Cette thèse a étudié l'origine du retournement tout optique hélicité dépendant de l'aimantation (AO-HDS) dans les structures magnéto-plasmoniques à base de multicouche de Co/Pt. Situé à l'intersection de la spintronique ultra-rapide et de la magnéto-plasmonique, ce travail fait progresser la connaissance dans ces deux domaines de recherche.

Le contrôle de l'aimantation à des échelles de temps ultrarapides est un domaine de recherche relativement récent et actif, qui présente un fort potentiel applicatif pour le stockage et le traitement de données rapides et économes en énergie. Alors que la désaimantation induite par laser femtoseconde et le retournement tout optique hélicité indépendant de l'aimantation ont été amplement étudiées et sont désormais relativement bien compris, l'origine de l'AO-HDS reste sujette à débat. Deux principaux mécanismes ont été proposés par la communauté scientifique pour expliquer le phénomène observé : le dichroïsme circulaire magnétique (MCD) et l'effet Faraday inverse (IFE). Leurs impacts mesurables étants similaires, leur distinction est particulièrement difficile. Pourtant, il est essentiel de clarifier leurs rôles respectifs pour optimiser l'AO-HDS et permettre la mise en place de systèmes avancés exploitant le transfert ultra-rapide de moment angulaire entre la lumière et l'aimantation.

Les systèmes plasmoniques, largement utilisés en photonique, sont des candidats prometteurs pour l'étude de l'AO-HDS due à leur capacité à confiner la lumière et à amplifier les interactions lumière-matière. Les résonances des systèmes magnéto-plasmoniques peuvent fortement modifier leurs réponses magnéto-optiques, notamment le MCD et l'IFE. Il est important de noter que l'aimantation induit un décalage de la longueur d'onde de résonance entre les deux polarisations circulaires opposées de la lumière, produisant un changement de signe du MCD près de la résonance, tandis que l'IFE est amplifié à la résonance grâce au confinement du champ électromagnétique proche. Cette différence fondamentale permet de séparer leurs contributions, une idée centrale de cette thèse.

Pour explorer ce concept, des multicouches de Co/Pt ont été synthétisées et structurées en nanostructures magnéto-plasmoniques, plus précisément en nanodisques répartis de manière aléatoire et en réseaux périodiques de nanodisques. La première configuration favorise les résonances plasmoniques de surface localisées avec une longueur d'onde de résonance déterminée par la taille et la forme des particules, tandis que la seconde présente des résonances de réseaux de surface plus tranchées résultant du couplage entre les particules. Les paramètres structurels ont été caractérisés par microscopie à force atomique et optimisés pour obtenir des résonances dans le domaine du visible au proche infrarouge.

Plusieurs techniques de mesure ont été développées ou améliorées dans le cadre de l'étude de l'AO-HDS dans ces systèmes. La méthode de mesure des spectres optiques et magnéto-optiques a été révisée. Le système de mesure lié au laser femtoseconde a été automatisé pour produire des diagrammes d'état du retournement tout optique de l'aimantation, et de nouvelles techniques de post-traitement ont été introduites pour caractériser des spots laser de forme arbitraire. Des protocoles expérimentaux et des procédures d'analyse spécialisés ont également été mis en place pour convenablement normaliser les spectres AO-HDS des dispositifs plasmoniques.

En complément, des simulations ont été réalisées afin d'interpréter et de reproduire les résultats expérimentaux. Un programme de calcul de la propagation d'ondes électromagnétiques dans

les couches minces basé sur la méthode de matrice de transfert 4×4 a été étendue afin de traiter les systèmes composés de couches magnétiques et afin de calculer les spectres magnéto-optiques. Ceci permet l'extraction des constantes de Voigt effectives à partir des données expérimentales. Des simulations par méthode des éléments finis, utilisant des tenseurs de permittivité déterminés expérimentalement, ont en outre permis l'optimisation des géométries des nanostructures et le calcul des spectres du MCD et de l'IFE.

Les mesures effectuées sur des multicouches de Co/Pt n'ont révélé aucun trait distinctif dans leurs réponses optique et magnéto-optique. L'analyse de la corrélation entre la réponse et l'épaisseur des couches minces a mis en évidence le rôle de la réflectivité dans le MCD, démontrant que le MCD conventionnellement dérivé à partir du spectre d'extinction ne représente pas correctement la différence d'absorption entre les deux polarisations circulaires opposées de la lumière. Cette dernière propriété étant pertinente pour l'étude de l'AO-HDS. Les expériences d'AO-HDS ont révélé une dépendance entre l'efficacité du retournement de l'aimantation et la durée de l'impulsion et le nombre de répétitions de couche de Co/Pt, les films plus épais présentant une efficacité de retournement de l'aimantation réduite. Cependant, aucune corrélation claire reliant l'AO-HDS au MCD ou à l'IFE n'a pu être identifiée.

Les réseaux de nanodisques distribué aléatoirement et périodiquement présentent les résonances plasmoniques attendues et leurs positions ont pu été reproduites avec les simulations. Des changements de signe des spectres de l'ellipticité et du MCD ont été observés près des résonances. Les expériences d'AO-HDS ont démontré un retournement partiel de l'aimantation au-dessus d'un seuil de fluence. Pour les réseaux périodiques, aucun changement de signe n'a été observé dans le spectre d'AO-HDS, probablement dû à la détérioration de l'impact des résonances du réseau de surface sur les effets magneto-optique après la désaimantation induite par les impulsions laser. En revanche, les nanodisques distribués de manière aléatoire ont présenté une inversion de signe dans leur spectre d'AO-HDS, ce qui correspond à une contribution du MCD. Cependant, un décalage spectral de ce passage à zéro par rapport au spectre du MCD mesuré suggère une contribution supplémentaire de l'IFE. De manière inattendue, une différence entre les seuils de fluence de désaimantation induite par les polarisations linéaire et circulaire a été observée. Ceci peut s'expliquer par la formation de points chauds dans les nanodisques qui dépendent sur le mode de propagation de la lumière.

En résumé, ces travaux démontrent que le contrôle de l'aimantation dépendant de l'hélicité peut être intégré dans des structures plasmoniques simples. L'étude de ces systèmes fournit des informations précieuses sur l'interaction entre les effets optique, magnéto-optique, le MCD et l'IFE. Les résultats soulignent le potentiel de l'amplification du AO-HDS dans les systèmes plasmonique. Ceci permet l'amélioration de l'efficacité énergétique des futurs dispositifs opto-magnétiques. Ces travaux peuvent être étendus dans plusieurs directions. Des nanodisques magnéto-plasmoniques peuvent être couplé avec des dispositifs électroniques, par exemple en les fabriquant sur des croix de Hall, pour étudier la dynamique du retournement de l'aimantation induite par multiple impulsion sur une échelle de temps adapter. Une autre piste consiste à exploiter l'amplification du MCD induit par les résonance plasmonique dans des matériaux présentant retournement tout optique hélicité indépendant de l'aimantation : un MCD suffisamment important pourrait séparer les seuils de fluence de retournement entre les directions initial opposé de l'aimantation, permettant ainsi un retournement déterministe avec une seule impulsion laser polarisée circulairement.

Annexe A

AFM measurements

Most fabricated structures were characterised with atomic force microscopy (AFM). This allowed for a systematic study during nano fabrication optimisation. The obtained dimensions were used in simulation to compare with the results, see Section 5.3. The advantages of using AFM over other imaging techniques, such as scanning electron microscopy (SEM), include higher resolutions, easier access to depth information, and a smaller impact of charge effects without sample modification. Indeed, the final structures are usually a metal structure on an insulator substrate. This can be challenging to measure with SEM without the addition of conductive resin to dissipate the accumulation of charges. In that case, there is a risk of contamination of the samples. However, AFM has several disadvantages, including reduced speed, sample drift, and the inability to image through a capping layer. To offset those drawbacks, the samples were loaded and left to settle before starting the measurements. Both forward and backwards traces were saved to reconstitute the final image. Finally, the AFM measurements are performed before any capping is deposited.

The measurements were mostly performed on a Park Systems NX10 at Institut Jean Lamour in contactless mode, but some (sample 1236) were done on a Bruker Dimension Icon at Aalto University by Junyoung Hyun [7]. A given sample would often have multiple arrays or patches of dots with small parameter changes, such as used lithography dose, disk size and packing factor or periodicity (in case of periodic array). Due to the large number of structures to characterise on each sample, a simple automation script was sometimes used to carry out the measurements.

The post process was carried out with the free software Gwyddion [134]. The process steps are carried out as follows:

- The minimum of the forward and backwards images is taken. In some instances, the proportional–integral–derivative (PID) controller that drives the cantilever is not fast enough, and a step down will not be correctly recorded. This leads to the forward and the backwards traces not overlapping at sharp edges. Taking the minimum of both traces can help with sharp features.

- The image can be cropped to a region of interest. Usually, partially imaged structures are excluded to help with the next steps of the analysis, as they can appear as smaller structures.

[7] NanoSpin group, Department of Applied Physics, Aalto University School of Science, Aalto FI-00076, Finland

- The rows are aligned only using the area between the structures considered as flat. To do so, a mask is applied to fully cover the structures. The rows are then aligned using the mean method or using a polynomial of degree 1, excluding the masked area.
- The direction orthogonal to the scan lines is scaled. Even after a long settling time and due to the long measuring time, the sample may still drift over time. The line scan is usually fast enough to neglect drift in that direction. However, an elongation or contraction can be observed in the other direction (noticeable for repeated imaging of the same area starting from the opposite side). By knowing the size of a feature in that direction (for example, by taking a short scan at 90° from the first one), the image can be scaled accordingly, making sure to scale the image and the associated pixel size.
- If the structure is periodic, the measure lattice tool can be used to extract the periodicity. In case of square arrays, the reported period along the scan line is preferred as it is less impacted by the distortion due to sample drift.
- A histogram of the height is plotted. It will feature two prominent peaks. One corresponds to the background level and one to the feature surfaces. By taking the difference of the centre positions, the mean height of the structures can be estimated.
- The structures are detected with grains marking using a threshold. The threshold is taken at the mean of the peak positions measured at the previous step. This corresponds to half of the height of the structures.
- The marked grains are filtered and measured. A filtering based on surface size can remove detected grains that do not correspond to the structures (background noise) or partially imaged structures. All grains above a specific size are kept, and their equivalent disk radius is extracted.
- Finally, the image is exported.

The final extracted feature size and images of structures studied in this thesis have been compiled in the following table and figure:

Sample name	Structure	Periodicity (nm)	Diameter (nm)
945_1c	C2	472	250
1026_2	A2	465	158
1026_2	A3	621	139
1026_2	A4	616	202
1236	P1350	470	172
1236	R1350	n/a	172

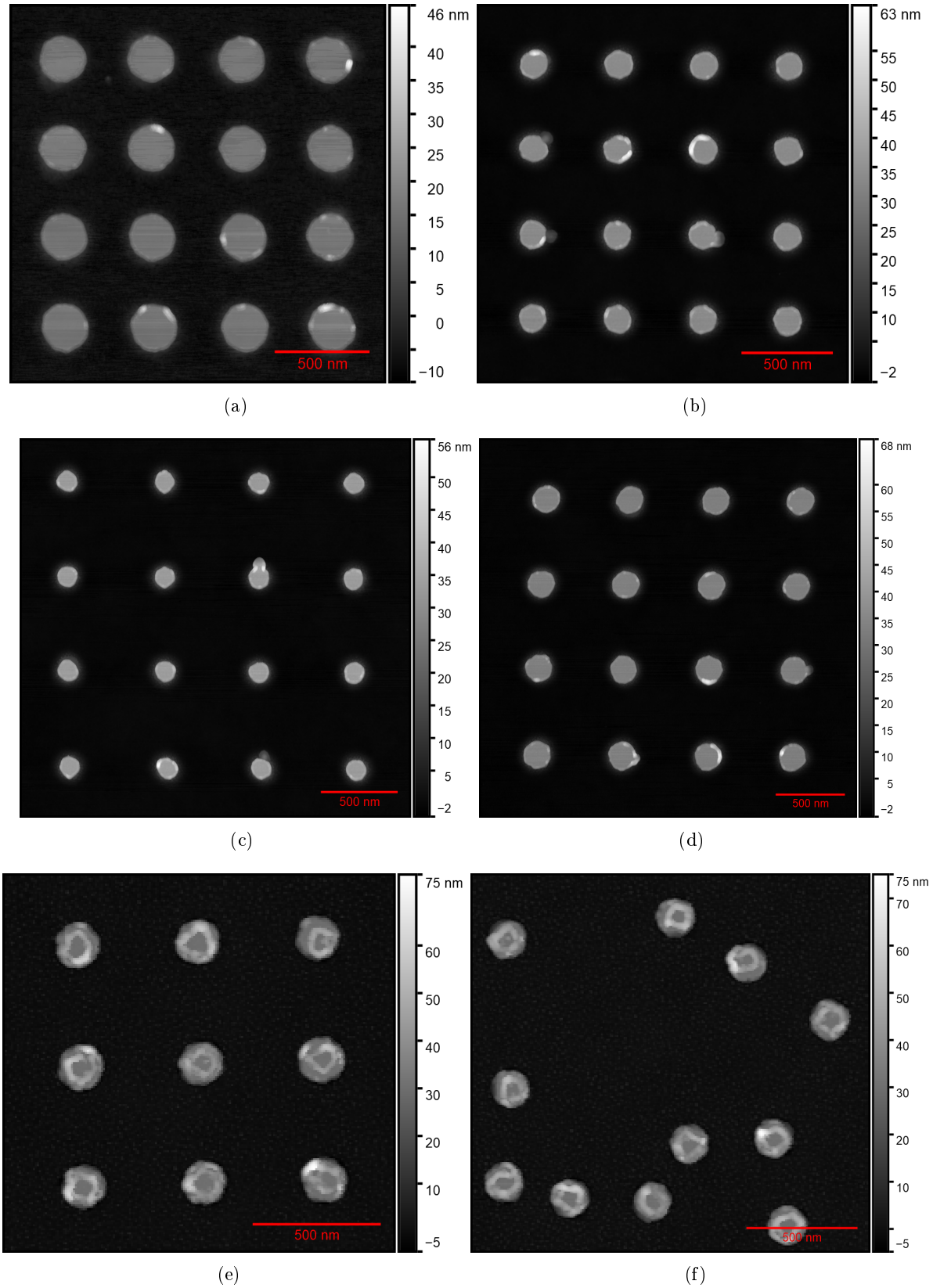

Figure A.1: AFM image of periodic and randomly distributed nano-disks structures. (a) Sample 945_1c ($[Co/Pt]_1$), structure C2. (b)-(d) Sample 1026_2 ($[Co/Pt]_{10}$), structure A2, A3 and A4 respectively. (e)-(f) Sample 1236 ($[Co/Pt]_{10}$), structure P1350 and R1350 respectively. The scale bars in all images are 500 nm.

Annexe B

Magneto-optical calculations

This annexe details the calculation of the measurements of the different magneto-optical responses and provides more background on the description of the elliptical polarisation of the light after its interaction with a magnetic sample.

MCD calculation

Equation 2.35, that describes the ellipticity of light in the circular base, leads to the following definition:

$$E_0 = \frac{|E^+| + |E^-|}{2} \qquad \Delta E = |E^+| - |E^-|$$

Using this notation, Equation 2.35 can be rewritten as:

$$\eta = \tan^{-1}\left(\frac{\Delta E}{2E_0}\right) \qquad \Delta E = 2E_0\tan(\eta)$$

The amplitude of the fields of opposite circularity can thus be written as:

$$|E^{\pm}| = E_0 \pm \frac{\Delta E}{2} = E_0(1 + \tan(\eta))$$

Taking the intensity of the circular modes yields:

$$I^{\pm} = E_0^2(1 \pm \tan(\eta))^2$$

This relation is applicable for both reflection and transmission as expressed in Equation 3.7 and 3.6. The difference of intensity for opposite circularity is then:

$$\Delta I = 4I_0\tan(\eta)$$

With

$$\begin{aligned} I_0 = E_0^2 &= \frac{1}{4}(|E^+|^2 + |E^-|^2 + 2|E^+||E^-|) \\ &= \frac{1}{4}(I^+ + I^-) + \frac{1}{2}E_0^2(1 - \tan^2(\eta)) \end{aligned}$$

For small ellipticity $1 - \tan^2(\eta) \simeq 1$ and the previous equation simplifies to the mean intensity:

$$I_0 = \frac{1}{2}(I^+ + I^-)$$

Finally, Equation 2.38 that expresses MCD from the ellipticities can be recovered by considering that $A = 1 - R - T$:

$$MCD = \frac{\Delta A}{A} = \frac{\Delta(1-R-T)}{A} = -\frac{\Delta R + \Delta T}{A} = -4\frac{R\tan(\eta_K) + T\tan(\eta_F)}{A}$$

Magneto-optical measurements

Using Jones' formalism, the polarisation of the light interacting with an optical component can be described as matrix multiplications. The matrices corresponding to the different optical components used are described below:

Polariser	$\begin{bmatrix} \cos^2(\alpha) & \cos(\alpha)\sin(\alpha) \\ \cos(\alpha)\sin(\alpha) & \sin^2(\alpha) \end{bmatrix}$
PEM	$e^{-\frac{i\rho}{2}} \begin{bmatrix} \cos^2(\beta) + e^{i\rho}\sin^2(\beta) & (1-e^{i\rho})\cos(\beta)\sin(\beta) \\ (1-e^{i\rho})\cos(\beta)\sin(\beta) & \sin^2(\beta) + e^{i\rho}\cos^2(\beta) \end{bmatrix}$
Sample	$\begin{bmatrix} x_{pp} & x_{ps} \\ x_{sp} & x_{ss} \end{bmatrix}$

With α the angle between the polariser axis and the vertical axis, β the angle between the PEM fast axis and the vertical axis, $\rho = \rho_0\sin(\omega t)$ is the PEM modulated retardation with ρ_0 and ω the amplitude and angular frequency of the retardation modulation respectively. $x_{ij} \in \{r, t\}$ denotes the complex Jones components fully characterising the polarisation of the reflected and transmitted light on or through the sample.

Considering the Kerr magnetometer described in Section 3.2.1 and the magneto-optical spectrometer described in Section 3.2.3, both are composed of the same succession of optical elements being a polariser at 0°, the sample (a near normal incidence), the PEM at 0°, an analyser at 45° and finally a photodiode (see Figures 3.2 and 3.4). The final intensity measured by the photodiode can be calculated in the following way:

$$I = \left| \frac{1}{2}\begin{bmatrix} 1 & 1 \\ 1 & 1 \end{bmatrix} e^{-\frac{i\rho}{2}} \begin{bmatrix} 1 & 0 \\ 0 & e^{i\rho} \end{bmatrix} \begin{bmatrix} x_{pp} & x_{ps} \\ x_{sp} & x_{ss} \end{bmatrix} \begin{bmatrix} 1 & 0 \\ 0 & 0 \end{bmatrix} \begin{bmatrix} E_{p,0} \\ E_{s,0} \end{bmatrix} \right|^2$$

$$= \frac{1}{2}\left| \begin{bmatrix} x_{pp}e^{-\frac{i\rho}{2}} + x_{sp}e^{\frac{i\rho}{2}} \\ x_{pp}e^{-\frac{i\rho}{2}} + x_{sp}e^{\frac{i\rho}{2}} \end{bmatrix} \right|^2 I_0$$

With $I_0 = |E_{p,0}|^2$, the incident light intensity aligned with the first polariser. By considering the complex ratio $\Psi_X = \frac{x_{sp}}{x_{pp}}$ this equation can be further developed:

$$\begin{aligned}
\frac{I}{I_0} &= (x_{pp}e^{-\frac{i\rho}{2}} + x_{sp}e^{\frac{i\rho}{2}})(x^*_{pp}e^{\frac{i\rho}{2}} + x^*_{sp}e^{-\frac{i\rho}{2}}) \\
&= |x_{pp}|^2 + |x_{sp}|^2 + x_{pp}x^*_{sp}e^{-i\rho} + x_{sp}x^*_{pp}e^{i\rho} \\
&= |x_{pp}|^2(1 + |\Psi_X|^2 + \frac{x^*_{sp}}{x^*_{pp}}e^{-i\rho} + \frac{x^*_{sp}}{x^*_{pp}}e^{i\rho}) \\
&= |x_{pp}|^2(1 + |\Psi_X|^2 + \Psi^*_X(\cos(\rho) - i\sin(\rho)) + \Psi_X(\cos(\rho) + i\sin(\rho))) \\
&= |x_{pp}|^2(1 + |\Psi_X|^2 + \cos(\rho)(\Psi_X + \Psi^*_X) + i\sin(\rho)(\Psi_X - \Psi^*_X)) \\
&= |x_{pp}|^2(1 + |\Psi_X|^2 + 2\cos(\rho)\Re(\Psi_X) - 2\sin(\rho)\Im(\Psi_X))
\end{aligned}$$

$\cos(\rho)$ and $\sin(\rho)$ can be decomposed into Bessel functions series. Only the first few orders will be considered.

$$\begin{aligned}
\cos(\rho) &= J_0(\rho_0) + 2J_2(\rho_0)\cos(2\omega t) + ... \\
\sin(\rho) &= 2J_1(\rho_0)\sin(\omega t) + ...
\end{aligned}$$

The intensity can then be divided into DC and harmonic components:

$$\begin{aligned}
I_{DC} &= I_0|x_{pp}|^2(1 + |\Psi_X|^2 + 2J_0(\rho_0)\Re(\Psi_X)) \\
I_\omega &= -4I_0|x_{pp}|^2J_1(\rho_0)\Im(\Psi_X) \\
I_{2\omega} &= 4I_0|x_{pp}|^2J_2(\rho_0)\Re(\Psi_X)
\end{aligned}$$

To normalise the signals by I_{DC}, the retardation modulation amplitude is chosen to be $\rho_0 = 2.405$ rad $= 0.383$ wave. For this value, the zero-th order Bessel function is equal to zero $J_0(\rho_0) = 0$ and the previous equations can be simplified into:

$$\begin{aligned}
I_{DC} &= I_0|x_{pp}|^2(1 + |\Psi_X|^2) \\
\frac{I_\omega}{I_{DC}} &= -\frac{4J_1(\rho_0)\Im(\Psi_X)}{1 + |\Psi_X|^2} \\
\frac{I_{2\omega}}{I_{DC}} &= \frac{4J_2(\rho_0)\Re(\Psi_X)}{1 + |\Psi_X|^2}
\end{aligned}$$

Since the incident light shining on the sample is linearly polarised along the p axis then the resulting polarisation is characterised by a arbitrary elliptical polarisation of ellipticity η and of rotation θ defined as the angle between the major axis of the ellipse and the p axis, the electric field components can be written as [96]:

$$\begin{bmatrix} E_p \\ E_s \end{bmatrix} = E_0e^{-\delta} \begin{bmatrix} \cos(\theta)\cos(\eta) - i\sin(\theta)\sin(\eta) \\ \sin(\theta)\cos(\eta) + i\cos(\theta)\sin(\eta) \end{bmatrix}$$

With E_0 the amplitude of the field along the long axis and δ the phase of the polarisation. Then the complex ratio between the components is:

$$\Psi_X = \frac{x_{sp}}{x_{pp}} = \frac{\tan(\theta) + i\tan(\eta)}{1 - i\tan(\theta)\tan(\eta)}$$

From this, the formulas for the rotation and ellipticity (Equations (2.31) and (2.30)) can be retrieved, and the two harmonic components can be rewritten as:

$$\begin{aligned} I_{DC} &= I_0|x_{pp}|^2(1 + |\Psi_X|^2) \\ \frac{I_\omega}{I_{DC}} &= -2J_1(\rho_0)\sin(2\eta_X) \\ \frac{I_{2\omega}}{I_{DC}} &= 2J_2(\rho_0)\sin(2\theta_X)\cos(2\eta_X) \end{aligned}$$

Note that by using the small angle approximation : $\sin(2\eta_X) \simeq 2\eta_X$, $\sin(2\theta_X) \simeq 2\theta_X$ and $\cos(2\eta_X) \simeq 1$ then this simplify into Equations (3.2) and (3.3). The $\sqrt{2}$ in these equations comes from the lock-ins providing RMS values for the harmonic components.

MCD measurements

The configuration for the MCD measurement described in Section 3.2.4 is now considered. This configuration is composed of the following optical elements: a polariser at 0°, a PEM at 45°, the sample (a near normal incidence) and the photodiode (see Figure 3.5). Similarly, the measured intensity can be written as:

$$\begin{aligned} I &= \left| \begin{bmatrix} x_{pp} & x_{ps} \\ x_{sp} & x_{ss} \end{bmatrix} \frac{1}{2} e^{-\frac{i\rho}{2}} \begin{bmatrix} 1 + e^{i\rho} & 1 - e^{i\rho} \\ 1 - e^{i\rho} & 1 + e^{i\rho} \end{bmatrix} \begin{bmatrix} 1 & 0 \\ 0 & 0 \end{bmatrix} \begin{bmatrix} E_{p,0} \\ E_{s,0} \end{bmatrix} \right|^2 \\ &= \left| \begin{bmatrix} x_{pp}\cos(\frac{\rho}{2}) - ix_{ps}\sin(\frac{\rho}{2}) \\ x_{sp}\cos(\frac{\rho}{2}) - ix_{ss}\sin(\frac{\rho}{2}) \end{bmatrix} \right|^2 I_0 \end{aligned}$$

The incoming light is considered to be normal to the sample. This implies that $x_{pp} = x_{ss}$ and $x_{ps} = -x_{sp}$. This allows further simplifications:

$$
\begin{aligned}
\frac{I}{I_0} &= (x_{pp}\cos(\frac{\rho}{2}) + ix_{sp}\sin(\frac{\rho}{2}))(x_{pp}^*\cos(\frac{\rho}{2}) - ix_{sp}^*\sin(\frac{\rho}{2})) \\
&\quad + (x_{sp}\cos(\frac{\rho}{2}) - ix_{pp}\sin(\frac{\rho}{2})))(x_{sp}^*\cos(\frac{\rho}{2}) + ix_{pp}^*\sin(\frac{\rho}{2})) \\
&= |x_{pp}|^2\cos^2(\frac{\rho}{2}) + |x_{sp}|^2\sin^2(\frac{\rho}{2}) - ix_{pp}x_{sp}^*\sin(\frac{\rho}{2})\cos(\frac{\rho}{2}) + ix_{sp}x_{pp}^*\sin(\frac{\rho}{2})\cos(\frac{\rho}{2}) \\
&\quad + |x_{pp}|^2\sin^2(\frac{\rho}{2}) + |x_{sp}|^2\cos^2(\frac{\rho}{2}) - ix_{pp}x_{sp}^*\sin(\frac{\rho}{2})\cos(\frac{\rho}{2}) + ix_{sp}x_{pp}^*\sin(\frac{\rho}{2})\cos(\frac{\rho}{2}) \\
&= |x_{pp}|^2 + |x_{sp}|^2 - 2ix_{pp}x_{sp}^*\sin(\frac{\rho}{2})\cos(\frac{\rho}{2}) + 2ix_{sp}x_{pp}^*\sin(\frac{\rho}{2})\cos(\frac{\rho}{2}) \\
&= |x_{pp}|^2(1 + |\Psi_X|^2 + 2i\sin(\frac{\rho}{2})\cos(\frac{\rho}{2})(\Psi_X - \Psi_X^*)) \\
&= |x_{pp}|^2(1 + |\Psi_X|^2 - 2\sin(\rho)\Im(\Psi_X))
\end{aligned}
$$

Using the previously established decomposition of $\sin(\rho)$, the intensity can be divided into a DC and the fundamental component:

$$
\begin{aligned}
\frac{I_{DC}}{I_0} &= I_0|x_{pp}|^2(1 + |\Psi_X|^2) \\
\frac{I_\omega}{I_0} &= -4I_0|x_{pp}|^2J_1(\rho_0)\Im(\Psi_X)
\end{aligned}
$$

After normalisation by I_{DC}, this can be linked back to the ellipticity:

$$
\frac{I_\omega}{I_{DC}} = -4\frac{J_1(\rho_0)\Im(\Psi_X)}{(1 + |\Psi_X|^2)} = -4J_1(\rho_0)\frac{\tan(\eta_X)}{1 + \tan^2(\eta_X)}
$$

For small angle $1 + \tan^2(\eta) \simeq 1$ and the formula for $\Delta R/R$ and $\Delta T/T$ (Equations (3.6) and (3.7)) can be retrieved. Again, the $\sqrt{2}$ in these equations comes from the lock-ins' RMS values. Furthermore, this demonstrates the equivalence between Equation 3.8 and Equation 2.38, meaning that a measurement of the ellipticity in transmission and reflection is, in theory, sufficient to measure the MCD of a sample.

Annexe C

Transfer matrix method implementation

This Annexe compiles the code used to perform the 4x4 transfer matrix method calculations. This relies on a Python library called *Pyllama* [114]. An interface was developed to allow the study of magneto-optical systems. A first add-on eases the calculation of the full permittivity matrix of a given material from tabulated values (Listing C.1). This can be done for any wavelength in the tabulated range and for arbitrary magnetisation directions. This is accomplished by interpolating the optical and magneto-optical parameters from the tabulated values and by using Equation 2.26. A function to calculate the rotation and ellipticity from the resulting Fresnel matrix of systems has also been implemented (Listing C.2) by using Equations 2.30 and 2.31. Finally, a convenient way to describe layered systems and to loop over a set or range of input parameters was integrated (Listing C.3). The provided example utilises the tabulated optical and magneto-optical parameters extracted by Atkinson et al. [116]. The simulated magneto-optical response can be seen in Figure C.1, and correctly reproduces the Kerr rotation and ellipticity spectra from their paper.

Listing C.1: Material propreties import and permitivity definition

```
import os
import warnings

import pandas as pd
import numpy as np

class Material:
    def __init__(self,filename=None,delimiter=None,rawData=None):
        if filename and delimiter:
            self.data =
                pd.read_csv(os.path.join(os.path.dirname(__file__),filename),delimiter=delimiter)
        elif rawData and np.array(rawData).ndim == 2:
            self.data =
                pd.DataFrame(rawData,columns=["l","n","k","Qr","Qi"][:np.array(rawData).shape[1]])
        else:
            self.data = pd.DataFrame()
            warnings.warn("Empty material")


def complexIndex(self,lda):
    return np.interp(lda, self.data["l"].to_numpy(),
        self.data["n"].to_numpy()+self.data["k"].to_numpy()*1j)

def VoigtConst(self,lda):
    if "Qr" in self.data and "Qi" in self.data:
        return np.interp(lda, self.data["l"].to_numpy(),
            self.data["Qr"].to_numpy()+self.data["Qi"].to_numpy()*1j)
    else:
        return 0

def dielectric(self,lda,Q=None,m=[0,0,0]):
    if Q==None:
            Q = self.VoigtConst(lda)
    epsilon = (self.complexIndex(lda))**2
    tensor = np.array([[1,-1j*m[2]*Q,1j*m[1]*Q],
            [1j*m[2]*Q,1,-1j*m[0]*Q],
            [-1j*m[1]*Q,1j*m[0]*Q,1]])
    return epsilon*tensor


Co = Material('Co_optical_index_Werner_et_al_2009_DFT.csv',delimiter=";")
Cu = Material('Cu_optical_index_McPeak_et_al_2015_exp.csv',delimiter=";")
Pt = Material('Pt_optical_index_Werner_et_al_2009_DFT.csv',delimiter=";")
CoPt = Material('CoPt_optical_index_Atkinson_et_al_1996.csv',delimiter=";")
Ta = Material('Ta_optical_index_Werner_et_al_2009_DFT.csv',delimiter=";")
Glass = Material('GlassMichel.csv',delimiter=";")
```

Listing C.2: Function to calculate the rotation and ellipticity from the Fresnel matrice

```
import numpy as np

def RotEll(FresnelMatrix):
    Xkp = FresnelMatrix[1,0]/FresnelMatrix[0,0]
    Xks = -FresnelMatrix[0,1]/FresnelMatrix[1,1]

    ThetaP = (1/2)*np.arctan(2*Xkp.real/(1-np.abs(Xkp)**2))
    EtaP = (1/2)*np.arcsin(2*Xkp.imag/(1+abs(Xkp)**2))
    ThetaS = (1/2)*np.arctan(2*Xks.real/(1-np.abs(Xks)**2))
    EtaS = (1/2)*np.arcsin(2*Xks.imag/(1+abs(Xks)**2))

    return [ThetaP,EtaP,ThetaS,EtaS]
```

Listing C.3: MO response simulation and ploting reproducing R. Atkinson measurements

```
import os
os.chdir(os.path.dirname(__file__))

import numpy as np
import pandas as pd
import matplotlib.pyplot as plt
from itertools import product, groupby
from collections import namedtuple

import pyllama
from optical_index.optical_index import Co,Cu,Pt,Ta,Glass,CoPt,Material
from MO_TMM_func import RotEll,position_resolved

#%% parameter sweep
flip = False

paramSweep = {"Wavelength" : list(range(320,860,10)),
       "ThetaIn" : [0],
       "CoPtThickness" : [60,79.5,99],
       "mz" : [1]
}

paramNames = list(paramSweep.keys())
Params = namedtuple('Params', paramNames, defaults=[paramSweep[p][0] for p in paramNames])
paramGen = (Params(**dict(zip(paramSweep.keys(), values))) for values in
     product(*paramSweep.values()))

results = {}
for param in paramGen:
    method = "TM"
    n_entry = 1 # Air
    nGlass = Glass.complexIndex(param.Wavelength/1000)
    n_exit = nGlass

    stack = [{"material" : CoPt,      "thickness" : param.CoPtThickness, "m" :
         (0,0, param.mz)}
    ]
```

```
    eps_list = list(map(lambda
        x:x["material"].dielectric(param.Wavelength/1000,m=x["m"]),stack))
    thickness_nm_list = list(map(lambda x:x["thickness"],stack))

    if flip:
        model = pyllama.StackModel(eps_list[::-1], thickness_nm_list[::-1], n_exit, n_entry,
            param.Wavelength, param.ThetaIn)
    else:
        model = pyllama.StackModel(eps_list, thickness_nm_list, n_entry, n_exit,
            param.Wavelength, param.ThetaIn)

    resultDict = {}
    resultDict["Fresnel"] = model.structure.get_fresnel(method=method)
    resultDict["RT"] = model.structure.get_refl_trans(method=method)
    results[param] = resultDict

#%% plot sweep results
groups = ["ThetaIn","mz"]
subgroup = ["ThetaIn","mz","CoPtThickness"]
Xaxis = "Wavelength"

keyfunc = lambda x:[getattr(x, key) for key in groups]
sortedKeys = list(sorted(results.keys(),key=keyfunc))

for k1, g1 in groupby(sortedKeys, keyfunc):
    g1 = list(g1)
    figax = plt.subplots(figsize=(10,7))

    keyfunc2 = lambda x:[getattr(x, key) for key in subgroup]
    sortedKeys2 = list(sorted(g1,key=keyfunc2))
    for k2, g2 in groupby(sortedKeys2, keyfunc2):
        g2 = list(g2)
        data = np.array(list(map(lambda x:[getattr(x,
            Xaxis),*RotEll(results[x]["Fresnel"][0])[:2]], g2)))
        figax[1].plot(data[:,0], data[:,1:]*180/np.pi, label=[r"$\theta_K (t_{CoPt} = $" +
            str(k2[-1]) + " nm)", r"$\epsilon_K(t_{CoPt} = $" + str(k2[-1]) + " nm)"])
    figax[1].set_title('  '.join([str(a)+" = "+str(b) for a,b in zip(groups,k1)]))
    figax[1].legend()
    figax[1].set_xlabel("Wavelength (nm)")
    figax[1].set_ylabel("MO response (deg)")
    plt.show()
```

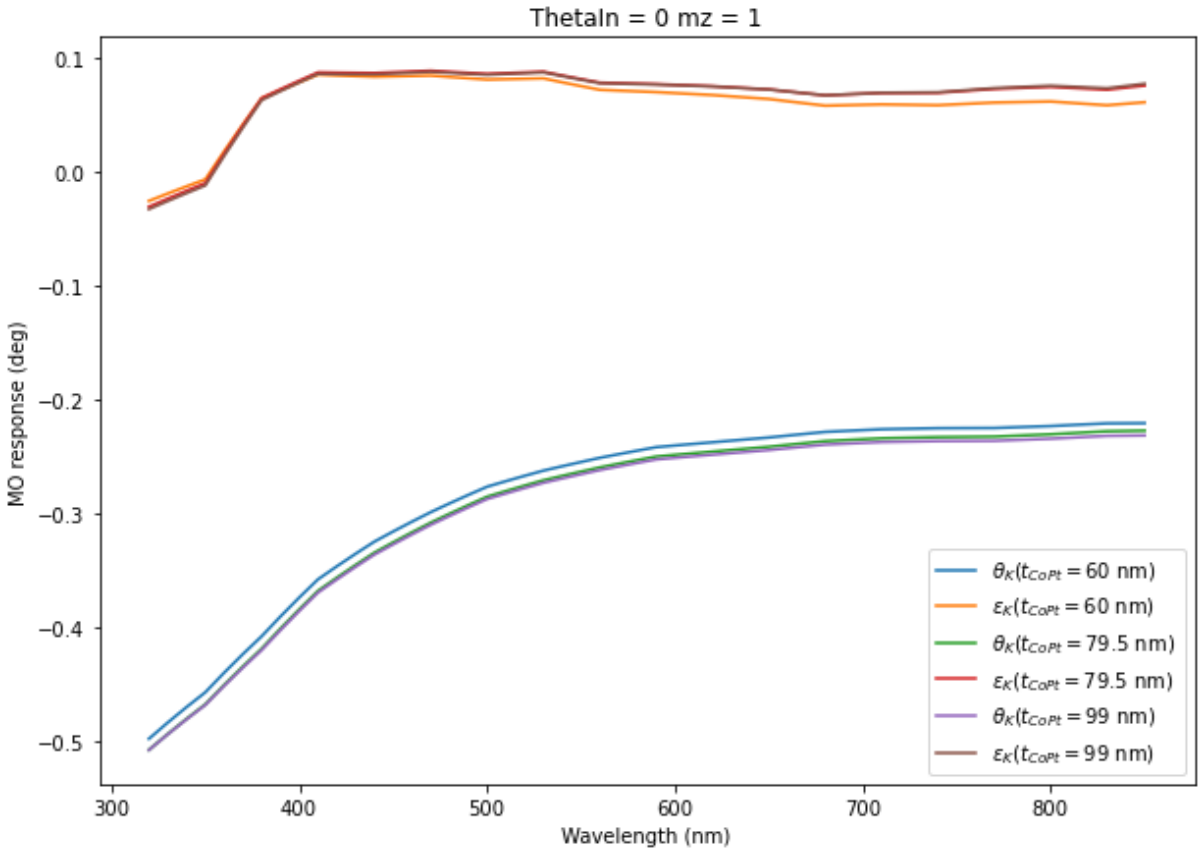

Figure C.1: Reproduction of Atkinson results in Co/Pt multilayers [116] using *PyLlama* implementation of the 4x4 TMM and the previous code snippet.

Annexe D

Magnetic force microscopy measurements

Some magnetic force microscopy was performed on array A2 of sample 1051b, composed of ten repetitions of Co/Pt. This structure and sample should be identical to array A2 on sample 1026_2, but without the capping layer to allow for these measurements. The measurements were done by Daniel Lacour[8] and analysed by Michel Hehn[8]. The sample was initialised by saturating half of the array up and the other half down using heat-assisted magnetisation switching. This consists of applying a field smaller than the coercivity of the sample while sweeping a linearly polarised laser beam to locally heat the sample. Only the region affected by the laser will align with the external field, while the rest remain untouched. The laser polarisation is then controlled using a quarter-wave plate and swept onto the sample to produce four regions with different initial states and exposed to opposite circular polarisations.

A first measurement using a low momentum tip reveals some instability as the magnetisation of certain nano-disks changes between successive scans or even during the same scan, as shown in Figure D.1 (b). Most disks are uniformly magnetised, but some disks show a split domain state as seen in Figure D.1 (c). These split domain states are less stable as they are more prone to disappear after multiple scans.

Using a high momentum tip, the different configuration regions were imaged and are compiled in Figure D.2. Instabilities can still be observed as some disks switch from black to white during the scan under the influence of the magnetic tip. This has the impact of biasing the final measured magnetic states towards the positive direction, taken as white.

To analyse the possible impact of dipolar coupling between disks, the normalised magnetisation and near neighbours correlation has been calculated for every final state. The mean magnetisation ($< m >$) is defined as the difference between the population of white (n_{white}) and black (n_{black}) disks divided by the total number of disks in the image.

$$< m >= \frac{n_{white} - n_{black}}{n_{white} + n_{black}} \tag{D.1}$$

The near-neighbour correlation characterises the tendency for neighbouring disks to end up antiparallel. For every disk in the image, it can be calculated with:

$$nnc_i = \frac{1}{4} \sum m_i m_j \tag{D.2}$$

[8]Spintronics and Nanomagnetism group, Physics of Matter and Material department, Université de Lorraine, CNRS, Institut Jean Lamour, Nancy F-54000, France

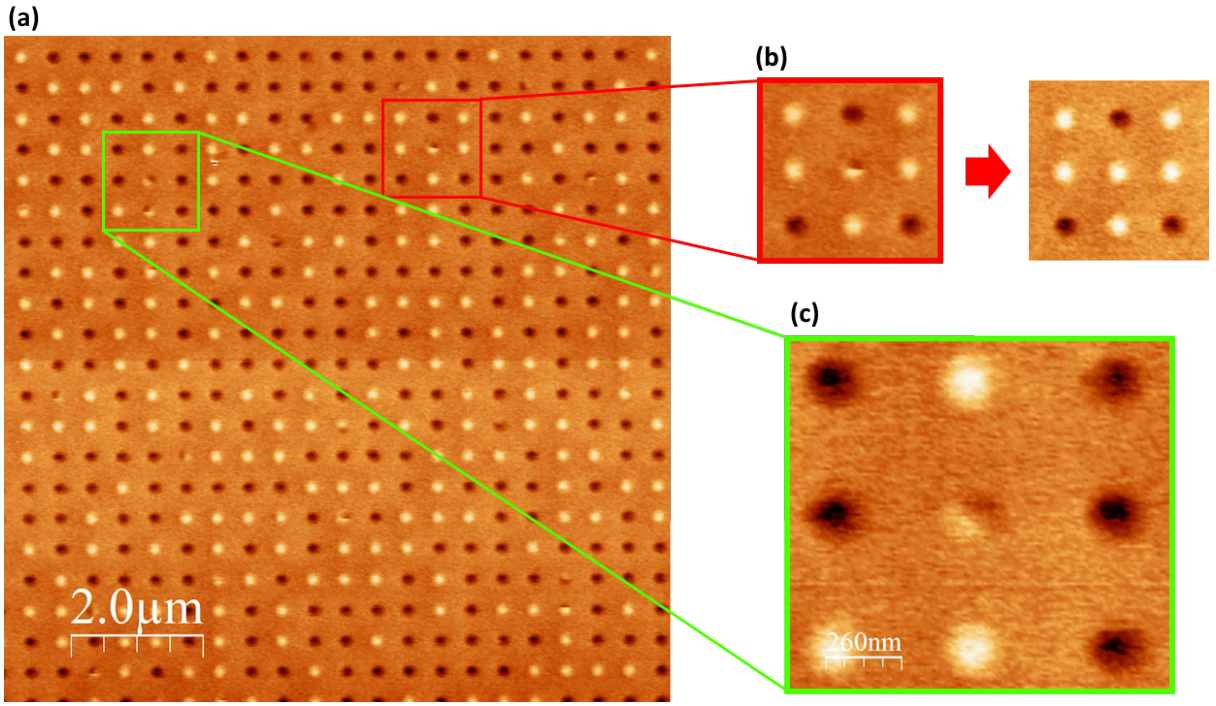

Figure D.1: MFM images of the Co/Pt nano-disk array A2 on sample 1051b. (a) First scan with a low-momentum tip. (b) Zoomed in images of the first and second scans of an area showing instability. (c) Zoomed-in image of a split domain disk.

With m_i and $m_j \in \{-1, 1\}$, the magnetisation direction of the considered disk and its j-th neighbour, respectively. If $nnc_i = 1$, then the disk is fully saturated with its neighbours, while in the case where $nnc_i = -1$, the disk is antiparallel to all its neighbours. The mean of this value over all the disks of the image provides some quantitative characterisation of the coupling strength between the disks with $< nnc_i >= -1$ corresponding to a full dipolar coupling between the disks.

The results of these measurements for these images are compiled in the following table:

	$< m >$	$< nnc >$
$\uparrow \sigma_+$	0.02	-0.040
$\downarrow \sigma_+$	0.77	0.591
$\uparrow \sigma_-$	-0.09	-0.097
$\downarrow \sigma_-$	0.13	-0.003

First, the ($\downarrow \sigma_+$) case stands out as an outlier in respect of both metrics. The origin of this is still unclear. The influence of the tip on the magnetic state makes it difficult to extract any real trend with respect to the mean magnetisation, especially for the small differences expected between the configurations. The near neighbour correlation, being close to zero, indicates that the dipolar coupling between the disks does not significantly impact the final magnetic state.

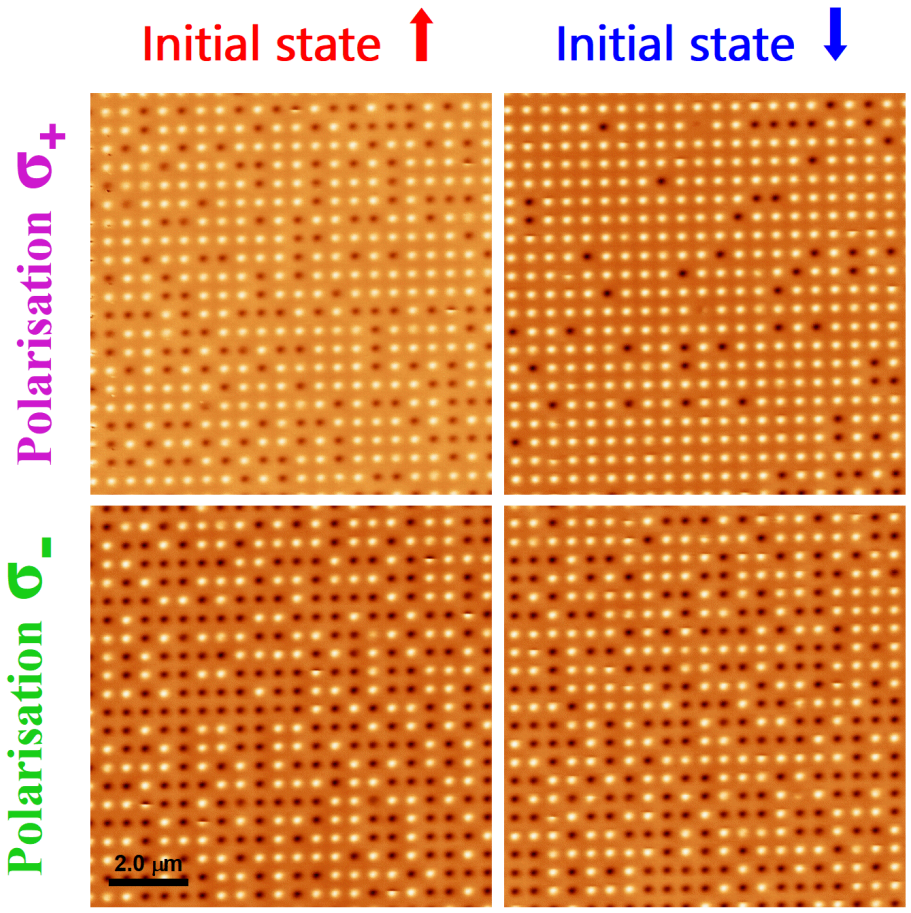

Figure D.2: MFM images of the final magnetic state of the Co/Pt nano-disk array A2 on sample 1051b after being initialised (up or down) and exposed to opposite circular polarisation (σ_+ or σ_-).

Bibliography

[1] G. Hamm, "2024 United States Data Center Energy Usage Report", Lawrence Berkely National Laboratory, 2025. DOI: 10.71468/P1WC7Q.

[2] L. Belkhir and A. Elmeligi, "Assessing ICT global emissions footprint: Trends to 2040 & recommendations", *Journal of Cleaner Production*, vol. 177, pp. 448–463, Mar. 2018, ISSN: 09596526. DOI: 10.1016/j.jclepro.2017.12.239.

[3] M. Kryder et al., "Heat Assisted Magnetic Recording", *Proceedings of the IEEE*, vol. 96, no. 11, pp. 1810–1835, Nov. 2008, ISSN: 0018-9219, 1558-2256. DOI: 10.1109/JPROC.2008.2004315.

[4] M. N. Baibich et al., "Giant Magnetoresistance of (001)Fe/(001)Cr Magnetic Superlattices", *Physical Review Letters*, vol. 61, no. 21, pp. 2472–2475, Nov. 21, 1988, ISSN: 0031-9007. DOI: 10.1103/PhysRevLett.61.2472.

[5] "Spin-transfer Torque MRAM Technology", Everspin Technologies. [Online]. Available: https://www.everspin.com/spin-transfer-torque-mram-technology.

[6] T. V. A. Nguyen et al., "Low write power and Field-free sub-ns write speed SOT-MRAM cell with Design Technology of Canted SOT structure and Magnetic Anisotropy for NVM", in *2025 IEEE International Memory Workshop (IMW)*, Monterey, CA, USA: IEEE, May 18, 2025, pp. 1–4, ISBN: 979-8-3503-6298-5. DOI: 10.1109/IMW61990.2025.11026972.

[7] E. Beaurepaire, J.-C. Merle, A. Daunois, and J.-Y. Bigot, "Ultrafast Spin Dynamics in Ferromagnetic Nickel", *Physical Review Letters*, vol. 76, no. 22, pp. 4250–4253, May 27, 1996, ISSN: 0031-9007, 1079-7114. DOI: 10.1103/physrevlett.76.4250.

[8] I. Radu et al., "Transient ferromagnetic-like state mediating ultrafast reversal of antiferromagnetically coupled spins", *Nature*, vol. 472, no. 7342, pp. 205–208, Apr. 2011, ISSN: 0028-0836, 1476-4687. DOI: 10.1038/nature09901.

[9] C. D. Stanciu et al., "All-Optical Magnetic Recording with Circularly Polarized Light", *Phys. Rev. Lett.*, vol. 99, no. 4, p. 047 601, Jul. 2007. DOI: 10.1103/PhysRevLett.99.047601.

[10] L. Wang, M. Hasanzadeh Kafshgari, and M. Meunier, "Optical Properties and Applications of Plasmonic-Metal Nanoparticles", *Advanced Functional Materials*, vol. 30, no. 51, p. 2 005 400, Dec. 2020, ISSN: 1616-301X, 1616-3028. DOI: 10.1002/adfm.202005400.

[11] M. Vergès et al., "Energy Efficient Single Pulse Switching of $[Co/Gd/Pt]_N$ Nanodisks Using Surface Lattice Resonances", *Advanced Science*, vol. 10, no. 4, p. 2 204 683, Feb. 2023, ISSN: 2198-3844, 2198-3844. DOI: 10.1002/advs.202204683.

[12] T.-M. Liu et al., "Nanoscale Confinement of All-Optical Magnetic Switching in TbFeCo - Competition with Nanoscale Heterogeneity", *Nano Letters*, vol. 15, no. 10, pp. 6862–6868, Oct. 14, 2015, ISSN: 1530-6984, 1530-6992. DOI: 10.1021/acs.nanolett.5b02743.

[13] S. Pourjamal, M. Kataja, N. Maccaferri, P. Vavassori, and S. Van Dijken, "Tunable magnetoplasmonics in lattices of Ni/SiO2/Au dimers", *Scientific Reports*, vol. 9, no. 1, p. 9907, Jul. 9, 2019, ISSN: 2045-2322. DOI: 10.1038/s41598-019-46058-2.

[14] G. Armelles, A. Cebollada, A. García-Martín, and M. U. González, "Magnetoplasmonics: Combining Magnetic and Plasmonic Functionalities", *Advanced Optical Materials*, vol. 1, no. 1, pp. 10–35, Jan. 2013, ISSN: 2195-1071, 2195-1071. DOI: 10.1002/adom.201200011.

[15] J. M. D. Coey, *Magnetism and Magnetic Materials*, 1st ed. Cambridge University Press, Jan. 1, 2001, ISBN: 978-0-521-01676-6 978-0-521-81614-4 978-0-511-84500-0. DOI: 10.1017/cbo9780511845000.

[16] S. Blundell, *Magnetism in Condensed Matter* (Oxford Master Series in Condensed Matter Physics 4), Reprint. Oxford: Oxford Univ. Press, 2014, 238 pp., ISBN: 978-0-19-850591-4.

[17] A. Hubert and R. Schäfer, *Magnetic Domains: The Analysis of Magnetic Microstructures*, Softcover reprint of the hardcover 1st ed. 1998, corrected printing 2000. Berlin Heidelberg: Springer, 2014, 696 pp., ISBN: 978-3-540-85054-0 978-3-662-30956-8.

[18] M. T. Johnson, P. J. H. Bloemen, F. J. A. D. Broeder, and J. J. D. Vries, "Magnetic anisotropy in metallic multilayers", *Reports on Progress in Physics*, vol. 59, no. 11, pp. 1409–1458, Nov. 1, 1996, ISSN: 0034-4885, 1361-6633. DOI: 10.1088/0034-4885/59/11/002.

[19] L. Néel, "L'anisotropie superficielle des substances ferromagnétiques", *Comptes Rendus Hebdomadaires Des Seances De L Academie Des Sciences*, vol. 237, no. 23, pp. 1468–1470, 1953.

[20] U. Gradmann, "Chapter 1 Magnetism in ultrathin transition metal films", in *Handbook of Magnetic Materials*, vol. 7, Elsevier, 1993, pp. 1–96, ISBN: 978-0-444-89853-1. DOI: 10.1016/S1567-2719(05)80042-3.

[21] P. J. Metaxas et al., "Creep and Flow Regimes of Magnetic Domain-Wall Motion in Ultrathin Pt / Co / Pt Films with Perpendicular Anisotropy", *Physical Review Letters*, vol. 99, no. 21, p. 217208, Nov. 21, 2007, ISSN: 0031-9007, 1079-7114. DOI: 10.1103/PhysRevLett.99.217208.

[22] C.-J. Lin et al., "Magnetic and structural properties of Co/Pt multilayers", *Journal of Magnetism and Magnetic Materials*, vol. 93, pp. 194–206, Feb. 1991, ISSN: 03048853. DOI: 10.1016/0304-8853(91)90329-9.

[23] P. Hansen, C. Clausen, G. Much, M. Rosenkranz, and K. Witter, "Magnetic and magneto-optical properties of rare-earth transition-metal alloys containing Gd, Tb, Fe, Co", *Journal of Applied Physics*, vol. 66, no. 2, pp. 756–767, Jul. 15, 1989, ISSN: 0021-8979, 1089-7550. DOI: 10.1063/1.343551.

[24] V. G. Harris, K. D. Aylesworth, B. N. Das, W. T. Elam, and N. C. Koon, "Structural origins of magnetic anisotropy in sputtered amorphous Tb-Fe films", *Physical Review Letters*, vol. 69, no. 13, pp. 1939–1942, Sep. 28, 1992, ISSN: 0031-9007. DOI: 10.1103/PhysRevLett.69.1939.

[25] J.-L. Bello, D. Lacour, S. Migot, J. Ghanbaja, S. Mangin, and M. Hehn, "Impact of interfaces on magnetic properties of Gdx(Fe90Co10)1x alloys", *Applied Physics Letters*, vol. 121, no. 21, Nov. 21, 2022, ISSN: 0003-6951, 1077-3118. DOI: 10.1063/5.0125011.

[26] H. E. Elsayed-Ali, T. B. Norris, M. A. Pessot, and G. A. Mourou, "Time-resolved observation of electron-phonon relaxation in copper", *Physical Review Letters*, vol. 58, no. 12, pp. 1212–1215, Mar. 23, 1987, ISSN: 0031-9007. DOI: 10.1103/physrevlett.58.1212.

[27] W. S. Fann, R. Storz, H. W. K. Tom, and J. Bokor, "Electron thermalization in gold", *Physical Review B*, vol. 46, no. 20, pp. 13 592–13 595, Nov. 15, 1992, ISSN: 0163-1829, 1095-3795. DOI: 10.1103/physrevb.46.13592.

[28] S. D. Brorson, J. G. Fujimoto, and E. P. Ippen, "Femtosecond electronic heat-transport dynamics in thin gold films", *Physical Review Letters*, vol. 59, no. 17, pp. 1962–1965, Oct. 26, 1987, ISSN: 0031-9007. DOI: 10.1103/physrevlett.59.1962.

[29] I. Lifshits, M. Kaganov, and L. Tanatarov, "On the theory of radiation-induced changes in metals", *Journal of Nuclear Energy. Part A. Reactor Science*, vol. 12, no. 1–2, pp. 69–78, May 1960, ISSN: 0368-3265. DOI: 10.1016/0368-3265(60)90010-4.

[30] X. Chen et al., "Ultrafast demagnetization in ferromagnetic materials: Origins and progress", *Physics Reports*, vol. 1102, pp. 1–63, Jan. 2025, ISSN: 0370-1573. DOI: 10.1016/j.physrep.2024.10.008.

[31] C. Davies et al., "Pathways for Single-Shot All-Optical Switching of Magnetization in Ferrimagnets", *Physical Review Applied*, vol. 13, no. 2, Feb. 24, 2020, ISSN: 2331-7019. DOI: 10.1103/physrevapplied.13.024064.

[32] T. Ostler et al., "Ultrafast heating as a sufficient stimulus for magnetization reversal in a ferrimagnet", *Nature Communications*, vol. 3, no. 1, p. 666, Feb. 7, 2012, ISSN: 2041-1723. DOI: 10.1038/ncomms1666.

[33] Y. Yang, R. B. Wilson, J. Gorchon, C.-H. Lambert, S. Salahuddin, and J. Bokor, "Ultrafast magnetization reversal by picosecond electrical pulses", *Science Advances*, vol. 3, no. 11, Nov. 3, 2017, ISSN: 2375-2548. DOI: 10.1126/sciadv.1603117.

[34] J. Wei et al., "All-optical Helicity-Independent Switching State Diagram in Gd - Fe - Co Alloys", *Physical Review Applied*, vol. 15, no. 5, p. 054 065, May 28, 2021, ISSN: 2331-7019. DOI: 10.1103/PhysRevApplied.15.054065.

[35] A. Ceballos et al., "Role of element-specific damping in ultrafast, helicity-independent, all-optical switching dynamics in amorphous (Gd,Tb)Co thin films", *Physical Review B*, vol. 103, no. 2, Jan. 25, 2021, ISSN: 2469-9950, 2469-9969. DOI: 10.1103/physrevb.103.024438.

[36] W. Zhang et al., "Role of spin-lattice coupling in ultrafast demagnetization and all optical helicity-independent single-shot switching in Gd1xyTbyCox alloys", *Physical Review B*, vol. 105, no. 5, Feb. 11, 2022, ISSN: 2469-9950, 2469-9969. DOI: 10.1103/physrevb.105.054410.

[37] Y. Liu et al., "Ultrafast single-pulse switching of Tb-dominant CoTb alloy", *Applied Physics Letters*, vol. 122, no. 2, Jan. 9, 2023, ISSN: 0003-6951, 1077-3118. DOI: 10.1063/5.0131716.

[38] M. L. M. Lalieu, M. J. G. Peeters, S. R. R. Haenen, R. Lavrijsen, and B. Koopmans, "Deterministic all-optical switching of synthetic ferrimagnets using single femtosecond laser pulses", *Physical Review B*, vol. 96, no. 22, Dec. 26, 2017, ISSN: 2469-9950, 2469-9969. DOI: 10.1103/physrevb.96.220411.

[39] L. Avilés-Félix et al., "Single-shot all-optical switching of magnetization in Tb/Co multilayer-based electrodes", *Scientific Reports*, vol. 10, no. 1, Mar. 23, 2020, ISSN: 2045-2322. DOI: 10.1038/s41598-020-62104-w.

[40] M. Verges et al., "Extending the scope and understanding of all-optical magnetization switching in Gd-based alloys by controlling the underlying temperature transients", *Physical Review Applied*, vol. 21, no. 4, Apr. 1, 2024, ISSN: 2331-7019. DOI: 10.1103/physrevapplied.21.044003.

[41] S. Mangin et al., "Engineered materials for all-optical helicity-dependent magnetic switching", *Nature Materials*, vol. 13, no. 3, pp. 286–292, Mar. 1, 2014, ISSN: 1476-4660. DOI: 10.1038/nmat3864.

[42] A. Hassdenteufel et al., "Thermally Assisted All-Optical Helicity Dependent Magnetic Switching in Amorphous $Fe_{100-x}Tb_x$ Alloy Films", *Advanced Materials*, vol. 25, no. 22, pp. 3122–3128, Jun. 11, 2013, ISSN: 0935-9648, 1521-4095. DOI: 10.1002/adma.201300176.

[43] C.-H. Lambert et al., "All-optical control of ferromagnetic thin films and nanostructures", *Science*, vol. 345, no. 6202, pp. 1337–1340, Sep. 12, 2014, ISSN: 0036-8075, 1095-9203. DOI: 10.1126/science.1253493.

[44] Y. K. Takahashi et al., "Accumulative Magnetic Switching of Ultrahigh-Density Recording Media by Circularly Polarized Light", *Physical Review Applied*, vol. 6, no. 5, Nov. 14, 2016, ISSN: 2331-7019. DOI: 10.1103/physrevapplied.6.054004.

[45] G. Kichin, M. Hehn, J. Gorchon, G. Malinowski, J. Hohlfeld, and S. Mangin, "From Multiple- to Single-Pulse All-Optical Helicity-Dependent Switching in Ferromagnetic Co / Pt Multilayers", *Physical Review Applied*, vol. 12, no. 2, p. 024 019, Aug. 9, 2019, ISSN: 2331-7019. DOI: 10.1103/PhysRevApplied.12.024019.

[46] R. Medapalli et al., "Multiscale dynamics of helicity-dependent all-optical magnetization reversal in ferromagnetic Co/Pt multilayers", *Physical Review B*, vol. 96, no. 22, p. 224 421, Dec. 15, 2017, ISSN: 2469-9950, 2469-9969. DOI: 10.1103/PhysRevB.96.224421.

[47] K. T. Yamada et al., "Efficient All-Optical Helicity Dependent Switching of Spins in a Pt/-Co/Pt Film by a Dual-Pulse Excitation", *Frontiers in Nanotechnology*, vol. 4, p. 765 848, Feb. 23, 2022, ISSN: 2673-3013. DOI: 10.3389/fnano.2022.765848.

[48] T. X. Huang, W. Zhang, M. Hehn, G. Malinowski, S. Mangin, and J. Hohlfeld, "Role of domain nucleation and domain wall motion in all-optical helicity-dependent switching", *Physical Review B*, vol. 111, no. 14, Apr. 8, 2025, ISSN: 2469-9950, 2469-9969. DOI: 10.1103/physrevb.111.144408.

[49] J. Gorchon, Y. Yang, and J. Bokor, "Model for multishot all-thermal all-optical switching in ferromagnets", *Physical Review B*, vol. 94, no. 2, Jul. 19, 2016, ISSN: 2469-9950, 2469-9969. DOI: 10.1103/physrevb.94.020409.

[50] M. O. A. Ellis, E. E. Fullerton, and R. W. Chantrell, "All-optical switching in granular ferromagnets caused by magnetic circular dichroism", *Scientific Reports*, vol. 6, no. 1, Jul. 28, 2016, ISSN: 2045-2322. DOI: 10.1038/srep30522.

[51] L. Néel, "Théorie du traînage magnétique des ferromagnétiques en grains fins avec application aux terres cuites", *Annales de géophysique*, vol. 5, pp. 99–136, 1949.

[52] W. F. Brown, "Thermal Fluctuations of a Single-Domain Particle", *Physical Review*, vol. 130, no. 5, pp. 1677–1686, Jun. 1, 1963, ISSN: 0031-899X. DOI: 10.1103/PhysRev.130.1677.

[53] M. Stiehl et al., "All-optical switching in Cr - and Mn -doped L 1 0 Fe Pt thin films", *Physical Review Applied*, vol. 21, no. 5, p. 054 064, May 30, 2024, ISSN: 2331-7019. DOI: 10.1103/PhysRevApplied.21.054064.

[54] L. P. Pitaevskii, "Electric forces in a transparent dispersive medium", *Sov. Phys. JETP*, vol. 12, no. 5, pp. 1008–1013, 1961, ISSN: 0038-5646.

[55] J. P. van der Ziel, P. S. Pershan, and L. D. Malmstrom, "Optically-Induced Magnetization Resulting from the Inverse Faraday Effect", *Phys. Rev. Lett.*, vol. 15, no. 5, pp. 190–193, Aug. 1965. DOI: 10.1103/PhysRevLett.15.190.

[56] P. S. Pershan, J. P. Van Der Ziel, and L. D. Malmstrom, "Theoretical Discussion of the Inverse Faraday Effect, Raman Scattering, and Related Phenomena", *Physical Review*, vol. 143, no. 2, pp. 574–583, Mar. 11, 1966, ISSN: 0031-899X. DOI: 10.1103/physrev.143.574.

[57] A. V. Kimel, A. Kirilyuk, P. A. Usachev, R. V. Pisarev, A. M. Balbashov, and Th. Rasing, "Ultrafast non-thermal control of magnetization by instantaneous photomagnetic pulses", *Nature*, vol. 435, no. 7042, pp. 655–657, Jun. 2005, ISSN: 0028-0836, 1476-4687. DOI: 10.1038/nature03564.

[58] R. Hertel, "Theory of the inverse Faraday effect in metals", *Journal of Magnetism and Magnetic Materials*, vol. 303, no. 1, pp. L1–L4, Aug. 2006, ISSN: 03048853. DOI: 10.1016/j.jmmm.2005.10.225.

[59] R. Hertel and M. Fähnle, "Macroscopic drift current in the inverse Faraday effect", *Physical Review B*, vol. 91, no. 2, p. 020 411, Jan. 29, 2015, ISSN: 1098-0121, 1550-235X. DOI: 10.1103/PhysRevB.91.020411.

[60] M. Battiato, G. Barbalinardo, and P. M. Oppeneer, "Quantum theory of the inverse Faraday effect", *Physical Review B*, vol. 89, no. 1, p. 014 413, Jan. 14, 2014, ISSN: 1098-0121, 1550-235X. DOI: 10.1103/PhysRevB.89.014413.

[61] M. Berritta, R. Mondal, K. Carva, and P. M. Oppeneer, "*Ab Initio* Theory of Coherent Laser-Induced Magnetization in Metals", *Physical Review Letters*, vol. 117, no. 13, p. 137 203, Sep. 21, 2016, ISSN: 0031-9007, 1079-7114. DOI: 10.1103/PhysRevLett.117.137203.

[62] B. Koopmans et al., "Explaining the paradoxical diversity of ultrafast laser-induced demagnetization", *Nature Materials*, vol. 9, no. 3, pp. 259–265, Mar. 2010, ISSN: 1476-1122, 1476-4660. DOI: 10.1038/nmat2593.

[63] T. D. Cornelissen, R. Córdoba, and B. Koopmans, "Microscopic model for all optical switching in ferromagnets", *Applied Physics Letters*, vol. 108, no. 14, p. 142 405, Apr. 6, 2016, ISSN: 0003-6951. DOI: 10.1063/1.4945660.

[64] D. Hinzke and U. Nowak, "Domain Wall Motion by the Magnonic Spin Seebeck Effect", *Physical Review Letters*, vol. 107, no. 2, Jul. 8, 2011, ISSN: 0031-9007, 1079-7114. DOI: 10.1103/physrevlett.107.027205.

[65] K. Uchida et al., "Observation of the spin Seebeck effect", *Nature*, vol. 455, no. 7214, pp. 778–781, Oct. 2008, ISSN: 0028-0836, 1476-4687. DOI: 10.1038/nature07321.

[66] M. S. El Hadri et al., "Domain size criterion for the observation of all-optical helicity-dependent switching in magnetic thin films", *Physical Review B*, vol. 94, no. 6, Aug. 15, 2016, ISSN: 2469-9950, 2469-9969. DOI: 10.1103/physrevb.94.064419.

[67] U. Parlak, R. Adam, D. E. Bürgler, S. Gang, and C. M. Schneider, "Optically induced magnetization reversal in [Co/Pt]N multilayers: Role of domain wall dynamics", *Physical Review B*, vol. 98, no. 21, Dec. 27, 2018, ISSN: 2469-9950, 2469-9969. DOI: 10.1103/physrevb.98.214443.

[68] G.-Q. Li et al., "Timescales and contribution of heating and helicity effect in helicity-dependent all-optical switching", *Rare Metals*, vol. 42, no. 1, pp. 234–243, Jan. 2023, ISSN: 1001-0521, 1867-7185. DOI: 10.1007/s12598-022-02117-8.

[69] Y. Quessab, M. Deb, J. Gorchon, M. Hehn, G. Malinowski, and S. Mangin, "Resolving the role of magnetic circular dichroism in multishot helicity-dependent all-optical switching", *Physical Review B*, vol. 100, no. 2, Jul. 23, 2019, ISSN: 2469-9950, 2469-9969. DOI: 10.1103/physrevb.100.024425.

[70] P. Scheid, G. Malinowski, S. Mangin, and S. Lebègue, "*Ab Initio* theory of magnetization induced by light absorption in ferromagnets", *Physical Review B*, vol. 100, no. 21, Dec. 2, 2019, ISSN: 2469-9950, 2469-9969. DOI: 10.1103/physrevb.100.214402.

[71] K. T. Yamada et al., "Magnetization reversal of a ferromagnetic Pt/Co/Pt film by helicity dependent absorption of visible to near-infrared laser pulses", *Physical Review B*, vol. 111, no. 2, Jan. 15, 2025, ISSN: 2469-9950, 2469-9969. DOI: 10.1103/physrevb.111.l020406.

[72] J. Peatross and M. Ware, *Physics of Light and Optics*, 2015 edition. Provo, Utah: Brigham Young University, Department of Physics, 2022, ISBN: 978-1-312-92927-2.

[73] W. S. Weiglhofer and A. Lakhtakia, Eds., *Introduction to Complex Mediums for Optics and Electromagnetics*. Bellingham, Wash: SPIE Optical Engineering Press, 2003, 757 pp., ISBN: 978-0-8194-4947-4.

[74] S. A. Maier, *Plasmonics: Fundamentals and Applications*. New York, NY: Springer US, 2007, ISBN: 978-0-387-33150-8 978-0-387-37825-1. DOI: 10.1007/0-387-37825-1.

[75] Y. Li, *Plasmonic Optics: Theory and Applications*. SPIE, Feb. 17, 2017, ISBN: 978-1-5106-0756-9. DOI: 10.1117/3.2263757.

[76] A. A. Maradudin, R. Sambles, and W. L. Barnes, Eds., *Modern Plasmonics*. Amsterdam: Elsevier, 2016, ISBN: 978-0-444-63813-7.

[77] C. F. Bohren and D. R. Huffman, *Absorption and Scattering of Light by Small Particles*, 1st ed. Wiley, Apr. 23, 1998, ISBN: 978-0-471-29340-8 978-3-527-61815-6. DOI: 10.1002/9783527618156.

[78] M. L. Brongersma and P. G. Kik, Eds., *Surface Plasmon Nanophotonics* (Springer Series in Optical Sciences). Dordrecht: Springer Netherlands, 2007, vol. 131, ISBN: 978-1-4020-4349-9 978-1-4020-4333-8. DOI: 10.1007/978-1-4020-4333-8.

[79] S. Asano and G. Yamamoto, "Light Scattering by a Spheroidal Particle", *Applied Optics*, vol. 14, no. 1, p. 29, Jan. 1, 1975, ISSN: 0003-6935, 1539-4522. DOI: 10.1364/ao.14.000029.

[80] H. Kuwata, H. Tamaru, K. Esumi, and K. Miyano, "Resonant light scattering from metal nanoparticles: Practical analysis beyond Rayleigh approximation", *Applied Physics Letters*, vol. 83, no. 22, pp. 4625–4627, Dec. 1, 2003, ISSN: 0003-6951, 1077-3118. DOI: 10.1063/1.1630351.

[81] V. G. Kravets, A. V. Kabashin, W. L. Barnes, and A. N. Grigorenko, "Plasmonic Surface Lattice Resonances: A Review of Properties and Applications", *Chemical Reviews*, vol. 118, no. 12, pp. 5912–5951, Jun. 27, 2018, ISSN: 0009-2665, 1520-6890. DOI: 10.1021/acs.chemrev.8b00243.

[82] F. Wang and Y. R. Shen, "General Properties of Local Plasmons in Metal Nanostructures", *Physical Review Letters*, vol. 97, no. 20, Nov. 17, 2006, ISSN: 0031-9007, 1079-7114. DOI: 10.1103/physrevlett.97.206806.

[83] M. G. Blaber, M. D. Arnold, and M. J. Ford, "A review of the optical properties of alloys and intermetallics for plasmonics", *Journal of Physics: Condensed Matter*, vol. 22, no. 14, p. 143 201, Apr. 14, 2010, ISSN: 0953-8984, 1361-648X. DOI: 10.1088/0953-8984/22/14/143201.

[84] K. T. Carron, H. W. Lehmann, W. Fluhr, M. Meier, and A. Wokaun, "Resonances of two-dimensional particle gratings in surface-enhanced Raman scattering", *Journal of the Optical Society of America B*, vol. 3, no. 3, p. 430, Mar. 1, 1986, ISSN: 0740-3224, 1520-8540. DOI: 10.1364/josab.3.000430.

[85] S. Zou, N. Janel, and G. C. Schatz, "Silver nanoparticle array structures that produce remarkably narrow plasmon lineshapes", *The Journal of Chemical Physics*, vol. 120, no. 23, pp. 10 871–10 875, Jun. 15, 2004, ISSN: 0021-9606, 1089-7690. DOI: 10.1063/1.1760740.

[86] A. D. Humphrey and W. L. Barnes, "Plasmonic surface lattice resonances on arrays of different lattice symmetry", *Physical Review B*, vol. 90, no. 7, p. 075 404, Aug. 7, 2014, ISSN: 1098-0121, 1550-235X. DOI: 10.1103/PhysRevB.90.075404.

[87] S. Zou and G. C. Schatz, "Narrow plasmonic/photonic extinction and scattering line shapes for one and two dimensional silver nanoparticle arrays", *The Journal of Chemical Physics*, vol. 121, no. 24, pp. 12 606–12 612, Dec. 22, 2004, ISSN: 0021-9606, 1089-7690. DOI: 10.1063/1.1826036.

[88] B. Auguié and W. L. Barnes, "Collective Resonances in Gold Nanoparticle Arrays", *Physical Review Letters*, vol. 101, no. 14, Sep. 30, 2008, ISSN: 0031-9007, 1079-7114. DOI: 10.1103/physrevlett.101.143902.

[89] B. Auguié, X. M. Bendaña, W. L. Barnes, and F. J. García De Abajo, "Diffractive arrays of gold nanoparticles near an interface: Critical role of the substrate", *Physical Review B*, vol. 82, no. 15, Oct. 27, 2010, ISSN: 1098-0121, 1550-235X. DOI: 10.1103/physrevb.82.155447.

[90] R. C. Jones, "A New Calculus for the Treatment of Optical Systems I : Description and Discussion of the Calculus", *Journal of the Optical Society of America*, vol. 31, no. 7, p. 488, Jul. 1, 1941, ISSN: 0030-3941. DOI: 10.1364/JOSA.31.000488.

[91] B. E. A. Saleh and M. C. Teich, *Fundamentals of Photonics* (Wiley Series in Pure and Applied Optics), J. W. Goodman, red. New York, USA: John Wiley & Sons, Inc., Aug. 14, 1991, ISBN: 978-0-471-83965-1 978-0-471-21374-1. DOI: 10.1002/0471213748.

[92] M. I. C. H. A. E. L. FARADAY, *FARADAYS DIARY Vol IV: Being the Various Philosophical Notes of Experimental Investigation.* 1839–1847, vol. IV.

[93] J. Kerr, "XLIII. *On rotation of the plane of polarization by reflection from the pole of a magnet*", *The London, Edinburgh, and Dublin Philosophical Magazine and Journal of Science*, vol. 3, no. 19, pp. 321–343, May 1877, ISSN: 1941-5982, 1941-5990. DOI: 10.1080/14786447708639245.

[94] J. Kerr, "XXIV. *On reflection of polarized light from the equatorial surface of a magnet*", *The London, Edinburgh, and Dublin Philosophical Magazine and Journal of Science*, vol. 5, no. 30, pp. 161–177, Mar. 1878, ISSN: 1941-5982, 1941-5990. DOI: 10.1080/14786447808639407.

[95] R. Atkinson and P. H. Lissberger, "Sign conventions in magneto-optical calculations and measurements", *Applied Optics*, vol. 31, no. 28, p. 6076, Oct. 1, 1992, ISSN: 0003-6935, 1539-4522. DOI: 10.1364/AO.31.006076.

[96] R. M. A. Azzam and N. M. Bashara, *Ellipsometry and Polarized Ligth* (North-Holland Personal Library). Amsterdam London New York [etc.]: North-Holland, 1992, ISBN: 978-0-444-87016-2.

[97] J. Chen et al., "Plasmonic Nickel Nanoantennas", *Small*, vol. 7, no. 16, pp. 2341–2347, Aug. 22, 2011, ISSN: 1613-6810, 1613-6829. DOI: 10.1002/smll.201100640.

[98] G. Weick and D. Weinmann, "Lifetime of the surface magnetoplasmons in metallic nanoparticles", *Physical Review B*, vol. 83, no. 12, Mar. 14, 2011, ISSN: 1098-0121, 1550-235X. DOI: 10.1103/physrevb.83.125405.

[99] N. Maccaferri et al., "Polarizability and magnetoplasmonic properties of magnetic general nanoellipsoids", *Optics Express*, vol. 21, no. 8, p. 9875, Apr. 22, 2013, ISSN: 1094-4087. DOI: 10.1364/oe.21.009875.

[100] N. Maccaferri et al., "Tuning the Magneto-Optical Response of Nanosize Ferromagnetic Ni Disks Using the Phase of Localized Plasmons", *Physical Review Letters*, vol. 111, no. 16, Oct. 14, 2013, ISSN: 0031-9007, 1079-7114. DOI: 10.1103/physrevlett.111.167401.

[101] M. Kataja, T. K. Hakala, A. Julku, M. J. Huttunen, S. van Dijken, and P. Törmä, "Surface lattice resonances and magneto-optical response in magnetic nanoparticle arrays", *Nature Communications*, vol. 6, no. 1, p. 7072, May 7, 2015, ISSN: 2041-1723. DOI: 10.1038/ncomms8072.

[102] F. Freire-Fernández, R. Mansell, and S. van Dijken, "Magnetoplasmonic properties of perpendicularly magnetized [Co / Pt] N nanodots", *Physical Review B*, vol. 101, no. 5, p. 054416, Feb. 11, 2020, ISSN: 2469-9950, 2469-9969. DOI: 10.1103/PhysRevB.101.054416.

[103] M. Kataja, S. Pourjamal, and S. van Dijken, "Magnetic circular dichroism of non-local surface lattice resonances in magnetic nanoparticle arrays", *Optics Express*, vol. 24, no. 4, pp. 3562–3571, Feb. 22, 2016. DOI: 10.1364/OE.24.003562.

[104] J. B. González-Díaz et al., "Plasmonic Au/Co/Au Nanosandwiches with Enhanced Magneto-optical Activity", *Small*, vol. 4, no. 2, pp. 202–205, Feb. 2008, ISSN: 1613-6810, 1613-6829. DOI: 10.1002/smll.200700594.

[105] J. B. González-Díaz, B. Sepúlveda, A. García-Martín, and G. Armelles, "Cobalt dependence of the magneto-optical response in magnetoplasmonic nanodisks", *Applied Physics Letters*, vol. 97, no. 4, Jul. 26, 2010, ISSN: 0003-6951, 1077-3118. DOI: 10.1063/1.3474617.

[106] F. Cheng et al., "All-Optical Manipulation of Magnetization in Ferromagnetic Thin Films Enhanced by Plasmonic Resonances", *Nano Letters*, vol. 20, no. 9, pp. 6437–6443, Sep. 9, 2020, ISSN: 1530-6984, 1530-6992. DOI: 10.1021/acs.nanolett.0c02089.

[107] M. Vergès, "Thermal control of all-optical switching in magnetic heterostructures and magnetoplasmonic metasurfaces", Université de Lorraine, Mar. 2023.

[108] H. Pezeshki et al., "Integrated Hybrid Plasmonic-Photonic Device for All-Optical Switching and Reading of Spintronic Memory", *Physical Review Applied*, vol. 19, no. 5, May 10, 2023, ISSN: 2331-7019. DOI: 10.1103/physrevapplied.19.054036.

[109] D. O. Ignatyeva et al., "Plasmonic layer-selective all-optical switching of magnetization with nanometer resolution", *Nature Communications*, vol. 10, no. 1, p. 4786, Dec. 2019, ISSN: 2041-1723. DOI: 10.1038/s41467-019-12699-0.

[110] J. Hurst, P. M. Oppeneer, G. Manfredi, and P.-A. Hervieux, "Magnetic moment generation in small gold nanoparticles via the plasmonic inverse Faraday effect", *Physical Review B*, vol. 98, no. 13, Oct. 23, 2018, ISSN: 2469-9950, 2469-9969. DOI: 10.1103/physrevb.98.134439.

[111] F. Cheng, C. Wang, Y. Xu, W. Ma, and Y. Liu, "Multiphysics Modeling of Plasmon-Enhanced All-Optical Helicity-Dependent Switching", *ACS Photonics*, vol. 10, no. 5, pp. 1259–1267, May 17, 2023, ISSN: 2330-4022, 2330-4022. DOI: 10.1021/acsphotonics.2c01815.

[112] M. Kataja, F. Freire-Fernández, J. P. Witteveen, T. K. Hakala, P. Törmä, and S. Van Dijken, "Plasmon-induced demagnetization and magnetic switching in nickel nanoparticle arrays", *Applied Physics Letters*, vol. 112, no. 7, Feb. 12, 2018, ISSN: 0003-6951, 1077-3118. DOI: 10.1063/1.5012857.

[113] T. C. Oakberg, "Technology for Polarization Measurement : Magneto-optic Kerr Effect", Hinds Instruments, Inc, APPLICATION NOTE, 2019.

[114] M. M. Bay, S. Vignolini, and K. Vynck, "PyLlama: A stable and versatile Python toolkit for the electromagnetic modelling of multilayered anisotropic media", *Computer Physics Communications*, vol. 273, p. 108 256, Apr. 2022, ISSN: 00104655. DOI: 10.1016/j.cpc.2021.108256.

[115] J. Zak, E. R. Moog, C. Liu, and S. D. Bader, "Magneto-optics of multilayers with arbitrary magnetization directions", *Physical Review B*, vol. 43, no. 8, pp. 6423–6429, Mar. 15, 1991, ISSN: 0163-1829, 1095-3795. DOI: 10.1103/PhysRevB.43.6423.

[116] R. Atkinson et al., "Fundamental optical and magneto-optical constants of Co/Pt and CoNi/Pt multilayered films", *Journal of Magnetism and Magnetic Materials*, vol. 162, no. 1, pp. 131–138, Sep. 1996, ISSN: 03048853. DOI: 10.1016/0304-8853(96)00335-6.

[117] *COMSOL Multiphysics®*, version v6.1. Stockholm, Sweden: COMSOL AB, 2022.

[118] *Wave Optics Module User's Guide*, Manual, Stockholm, Sweden: COMSOL AB, 2022.

[119] "Optical Scattering off a Gold Nanosphere", COMSOL AB, Stockholm, Sweden, Application example, 2022.

[120] S. S. Acimovic. "Srdjan COMSOL", Srdjan COMSOL. [Online]. Available: https://srdjancomsol.weebly.com/.

[121] *COMSOL Multiphysics Reference Manual*, Manual, Stockholm, Sweden: COMSOL AB, 2022.

[122] J. M. Liu, "Simple technique for measurements of pulsed Gaussian-beam spot sizes", *Optics Letters*, vol. 7, no. 5, p. 196, May 1, 1982, ISSN: 0146-9592, 1539-4794. DOI: 10.1364/OL.7.000196.

[123] W. B. Zeper, H. W. Van Kesteren, B. A. J. Jacobs, J. H. M. Spruit, and P. F. Carcia, "Hysteresis, microstructure, and magneto-optical recording in Co/Pt and Co/Pd multilayers", *Journal of Applied Physics*, vol. 70, no. 4, pp. 2264–2271, Aug. 15, 1991, ISSN: 0021-8979, 1089-7550. DOI: 10.1063/1.349419.

[124] S. Hashimoto and Y. Ochiai, "Co/Pt and Co/Pd multilayers as magneto-optical recording materials", *Journal of Magnetism and Magnetic Materials*, vol. 88, no. 1–2, pp. 211–226, Jul. 1990, ISSN: 03048853. DOI: 10.1016/S0304-8853(97)90031-7.

[125] J. X. Shen, R. D. Kirby, K. Wierman, Z. .-. Shan, D. J. Sellmyer, and T. Suzuki, "Magnetization reversal and defects in Co/Pt multilayers", *Journal of Applied Physics*, vol. 73, no. 10, pp. 6418–6420, May 15, 1993, ISSN: 0021-8979, 1089-7550. DOI: 10.1063/1.352618.

[126] D. M. Donnet, V. G. Lewis, J. N. Chapman, K. O'Grady, and H. W. V. Kesteren, "Microstructure and hysteresis in Co/Pt multilayers", *Journal of Physics D: Applied Physics*, vol. 26, no. 10, pp. 1741–1745, Oct. 14, 1993, ISSN: 0022-3727, 1361-6463. DOI: 10.1088/0022-3727/26/10/030.

[127] O. Hellwig, G. Denbeaux, J. Kortright, and E. E. Fullerton, "X-ray studies of aligned magnetic stripe domains in perpendicular multilayers", *Physica B: Condensed Matter*, vol. 336, no. 1–2, pp. 136–144, Aug. 2003, ISSN: 09214526. DOI: 10.1016/S0921-4526(03)00282-5.

[128] J. E. Davies, O. Hellwig, E. E. Fullerton, G. Denbeaux, J. B. Kortright, and K. Liu, "Magnetization reversal of Co Pt multilayers: Microscopic origin of high-field magnetic irreversibility", *Physical Review B*, vol. 70, no. 22, p. 224 434, Dec. 29, 2004, ISSN: 1098-0121, 1550-235X. DOI: 10.1103/PhysRevB.70.224434.

[129] J.A. Woollam Co., *CompleteEASE Software Manual*, Manual, p. 442.

[130] C. Swindells et al., "Proximity-induced magnetism and the enhancement of damping in ferromagnetic/heavy metal systems", *Applied Physics Letters*, vol. 119, no. 15, p. 152 401, Oct. 11, 2021, ISSN: 0003-6951, 1077-3118. DOI: 10.1063/5.0064336.

[131] R. M. Rowan-Robinson et al., "The interfacial nature of proximity-induced magnetism and the Dzyaloshinskii-Moriya interaction at the Pt/Co interface", *Scientific Reports*, vol. 7, no. 1, p. 16 835, Dec. 4, 2017, ISSN: 2045-2322. DOI: 10.1038/s41598-017-17137-z.

[132] M. Grimsditch and P. Vavassori, "The diffracted magneto-optic Kerr effect: what does it tell you?", *Journal of Physics: Condensed Matter*, vol. 16, no. 9, R275–R294, Mar. 10, 2004, ISSN: 0953-8984, 1361-648X. DOI: 10.1088/0953-8984/16/9/R01.

[133] T. Schmitte, K. Westerholt, and H. Zabel, "Magneto-optical Kerr effect in the diffracted light of Fe gratings", *Journal of Applied Physics*, vol. 92, no. 8, pp. 4524–4530, Oct. 15, 2002, ISSN: 0021-8979, 1089-7550. DOI: 10.1063/1.1506190.

[134] D. Nečas and P. Klapetek, "Gwyddion: an open-source software for SPM data analysis", *Open Physics*, vol. 10, no. 1, pp. 181–188, Feb. 1, 2012, ISSN: 2391-5471. DOI: 10.2478/s11534-011-0096-2.

Résumé de la thèse

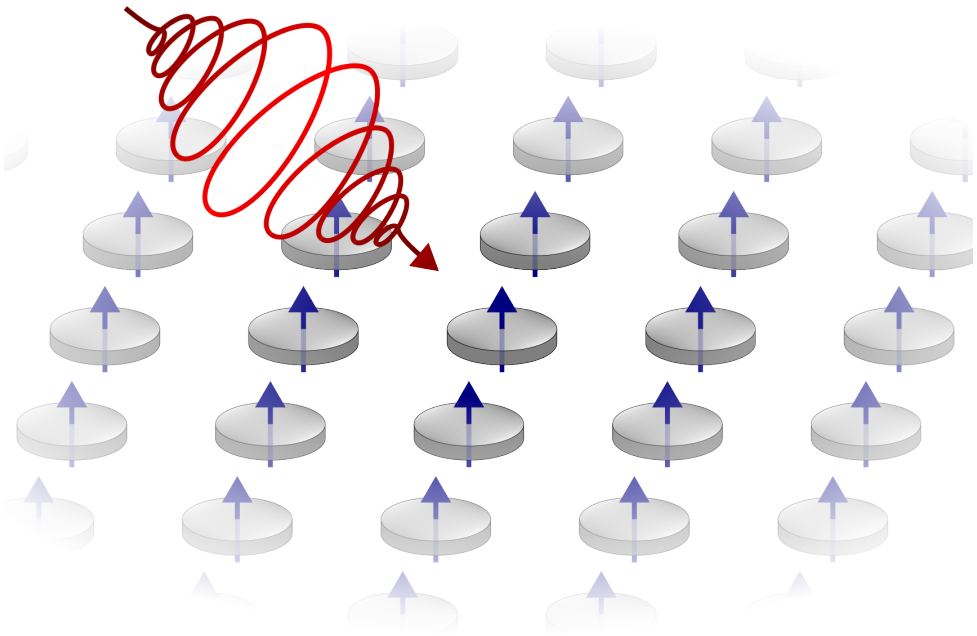

Représentation simplifié du type de système étudié dans cette thèse.

Le stockage et le traitement de données sont devenus un enjeu international. La demande en stockage haute performance a connu une croissance exponentielle au cours des dernières décennies, en particulier avec le récent et rapide développement de l'intelligence artificielle. Tout ce stockage et traitement de données s'accompagnent d'un coût énergétique très élevé. La consommation d'énergie des centres de données aux États-Unis devrait atteindre jusqu'à 12 % de la production d'électricité américaine d'ici 2028 [1]. L'impact environnemental ne peut aussi pas être négligé. Les technologies liées à information et de la communication représentent près de 3 % des émissions totales de gaz à effet de serre en 2018 et devrait atteindre jusqu'à 14 % en 2040. Près de la moitié de ces émissions étant associées aux centres de données[2].

Les dispositifs spintroniques, qui utilisent le spin des électrons plutôt que leur charge pour stocker et transférer des informations, offrent des avantages intéressants pour résoudre en partie ce problème. En s'appuyant sur l'aimantation pour stocker des informations de manière non-volatile, ils ne nécessitent aucune énergie pour rafraîchir et conserver les données stockées,

contrairement aux mémoires RAM basées sur la technologie CMOS. Cette approche n'est pas nouvelle, les supports de stockage magnétiques ont été développés dès le début du XXe siècle et sont encore couramment utilisés à ce jour sous la forme de disque dur. Les disques durs continuent d'être développés avec l'intégration récente de l'enregistrement magnétique assisté par chaleur [3], qui permet la fabrication de solutions de stockage de masse bon marché et de haute densité. Le principal problème de ces anciens dispositifs est leur vitesse d'écriture et de lecture, qui est incompatible avec leur intégration avec des systèmes de traitement de données de plus en plus rapide. La découverte de la magnétorésistance géante en 1988 [4], suivie de la magnétorésistance à effet tunnel, a conduit au développement de la mémoire RAM magnétorésistive ou MRAM, qui intègre étroitement le stockage magnétique au système informatique traditionnel basé sur la charge d'électrons. Néanmoins, en raison de la nature résistive du mécanisme sous-jacent, les opérations de lecture et d'écriture nécessitent encore une quantité d'énergie non-négligeable et les opérations d'écriture sont limitées, en pratique, à des vitesses de l'ordre de quelques dizaines de nanosecondes [5]. De nombreuses recherches sont menées pour remédier à ces problèmes, notamment avec le développement de la mémoire MRAM à couplage spin-orbite ou SOT-MRAM, qui atteint des vitesses plus élevées et une efficacité énergétique d'écriture record [6].

L'observation de la démagnétisation ultra-rapide du nickel induite par impulsion laser par Beaurepaire et al. en 1996 [7] a marqué le début du domaine de recherche consacré au contrôle ultra-rapide de l'aimantation. L'utilisation d'impulsions laser femtosecondes pour localement manipuler l'aimantation a fait l'objet d'études plus approfondies et a conduit à l'observation de deux phénomènes : le retournement tout optique hélicité indépendant de l'aimantation (AO-HIS) [8] et le retournement tout optique hélicité dépendant de l'aimantation (AO-HDS) [9]. Le premier effet est désormais considéré comme étant d'origine thermique, tandis que le second, qui semble provenir d'une interaction plus complexe entre la lumière et l'aimantation, n'est pas encore entièrement compris. Deux mécanismes ont été mis en avant pour expliquer cet effet de retournement : le dichroïsme circulaire magnétique (MCD) et l'effet Faraday inverse (IFE). Ces deux effets ont des impacts mesurables similaires et, par conséquent, il est difficile de distinguer leur contribution respective au retournement de l'aimantation. Combinées aux effets magnéto-optiques pour la lecture de l'état magnétique, ces méthodes de contrôle de l'aimantation pourraient permettre le développement de dispositifs de stockage de données entièrement optiques ultra-rapides exploitant le transfert ultra-rapide de moment angulaire entre la lumière et l'aimantation. Les bases de l'aimantation, la description des matériaux considéré ainsi qu'un état de l'art sur les différents type de retournement tout optique de l'aimantation sont détaillés dans le premier chapitre de cette thèse.

La plasmonique, qui étudie le couplage des oscillations électroniques à la surface des métaux avec les champs électromagnétiques, a fait l'objet de recherches intensives au cours du siècle dernier en raison de la capacité des système plasmonique à confiner la lumière à des échelles inférieures à la longueur d'onde et à amplifier les interactions entre la lumière et la matière. Les systèmes plasmoniques, constitués de nanoparticules métalliques, peuvent être ajustés en modifiant leur taille, leur forme et leur agencement afin de présenter des résonances à des longueurs d'onde spécifiques. Ces propriétés intéressantes ont conduit à l'intégration de dispositifs plasmoniques dans des applications de détection et d'amplification de l'absorption et de l'émission de la lumière [10].

Les systèmes plasmoniques sont des candidats prometteurs pour l'étude de l'AO-HDS et son intégration. Les résonances des systèmes magnéto-plasmoniques peuvent fortement modifier

leurs réponses magnéto-optiques, notamment le MCD et l'IFE. Il est important de noter que l'aimantation induit un décalage de la longueur d'onde de résonance entre les deux polarisations circulaires opposées de la lumière, produisant un changement de signe du MCD près de la résonance, tandis que l'IFE est amplifié à la résonance grâce au confinement du champ électromagnétique proche. Cette différence fondamentale permet de séparer leurs contributions, une idée centrale de cette thèse.

L'intégration du retournement tout optique de l'aimantation dans des systèmes plasmoniques ouvre une voie prometteuse pour leur intégration dans de nouveaux dispositifs de stockage de données. L'utilisation de systèmes magnéto-plasmoniques pour améliorer l'efficacité du retournement tout optique hélicité indépendant de l'aimantation a été démontrée [11] [12]. En revanche, le retournement tout optique hélicité dépendant de l'aimantation dans les systèmes magnéto-plasmoniques reste très peu exploré. Une meilleure compréhension de ce phénomène est nécessaire afin de concevoir et d'optimiser des structures magnéto-plasmoniques fonctionnelles, tout en améliorant leur efficacité énergétique. Par ailleurs, l'impact des effets plasmoniques sur les réponses magnéto-optiques a déjà été démontré et permet une amplification considérable de la sensibilité de lecture de l'état magnétique [11] [13] [14]. Les origines des effets plasmoniques et magnéto-optique ainsi que l'état de l'art sur l'impact des systèmes plasmoniques sur les réponses magnéto-optiques peuvent être retrouvés dans le deuxième chapitre de cette thèse.

Cette thèse étudie l'origine du retournement tout optique hélicité dépendant de l'aimantation dans les structures magnéto-plasmoniques à base de multicouche de Co/Pt. Situé à l'intersection de la spintronique ultra-rapide et de la magnéto-plasmonique, ce travail fait progresser la connaissance dans ces deux domaines de recherche. Pour explorer ce concept, des multicouches de Co/Pt ont été synthétisées par pulvérisation cathodique magnétron et structurées en nanostructures magnéto-plasmoniques par lithographie électronique. Les multicouches de Co/Pt on été choisi comme matériau de base, car il présente du AO-HDS et possède des propriétés intéressantes pour des future applications[22][123][124]. Ces films ont été structurés en deux types de configurations : des nanodisques répartis de manière aléatoire et des réseaux périodiques de nanodisques. La première configuration favorise les résonances plasmoniques de surface localisées avec une longueur d'onde de résonance déterminée par la taille et la forme des particules, tandis que la seconde présente des résonances de réseaux de surface plus prononcées résultant du couplage entre les particules. Les paramètres structurels ont été caractérisés par microscopie à force atomique et optimisés pour obtenir des résonances dans le domaine du visible au proche infrarouge.

Plusieurs techniques de mesure ont été développées ou améliorées dans le cadre de l'étude de l'AO-HDS dans ces systèmes. La méthode de mesure des spectres optiques et magnéto-optiques a été révisée. En particulier, une méthode pour extraire le MCD à partir de mesure magnéto-optique en transmission et réflexion été mise au point. Le système de mesure lié au laser femtoseconde a été automatisé pour produire des diagrammes d'état du retournement tout optique de l'aimantation, et de nouvelles techniques de post-traitement ont été introduites. Notamment, une technique pour caractériser *in-situ* des spots laser de forme arbitraire a été élaboré et est détailler dans le sixième chapitre de ce manuscrit. Des protocoles expérimentaux et des procédures d'analyse spécialisés ont également été mis en place pour convenablement normaliser les spectres AO-HDS des dispositifs plasmoniques étudiés.

En complément, des simulations ont été réalisées afin d'interpréter et de reproduire les résultats expérimentaux. Un programme de calcul de la propagation d'ondes électromagnétiques

dans les couches minces basé sur la méthode de matrice de transfert 4×4 a été étendue afin de traiter les systèmes composés de couches magnétiques. Cela permet le calculer les spectres magnéto-optiques et l'extraction des constantes de Voigt effectives à partir des données expérimentales. Des simulations par méthode des éléments finis (COMSOL Multiphysics®), utilisant des tenseurs de permittivité déterminée expérimentalement, ont en outre permis l'optimisation des géométries des nanostructures et le calcul des spectres du MCD et de l'IFE. La description des méthodes expérimentales et simulations utilisées durant ce projet peut être trouvée dans le troisième chapitre de cette thèse.

Les mesures effectuées sur des multicouches de Co/Pt n'ont révélé aucun trait distinctif dans leurs réponses optique et magnéto-optique. L'analyse de la corrélation entre la réponse et l'épaisseur des couches minces a mis en évidence le rôle de la réflectivité dans la mesure du MCD, démontrant que le MCD conventionnellement dérivé à partir du spectre d'extinction ne représente pas correctement la différence d'absorption entre les deux polarisations circulaires opposées de la lumière. Cette dernière propriété étant pertinente pour l'étude de l'AO-HDS. Les expériences d'AO-HDS ont révélé une dépendance entre l'efficacité du retournement de l'aimantation et la durée de l'impulsion ainsi que le nombre de répétitions de couche de Co/Pt, les films plus épais présentant une efficacité de retournement de l'aimantation réduite. Des diagrammes d'état illustrant la dépendance en fluence et en durée de pulse du AO-HDS ainsi que la formation de multidomain ont été produit pour les différentes couches minces étudiées. Une étude en fonction de la longueur d'onde a été réalisée, cependant aucune corrélation spectrale claire reliant l'AO-HDS au MCD ou à l'IFE n'a pu être identifiée. Les caractérisations et résultats complets sur les films minces de Co/Pt sont trouvables dans le quatrième chapitre de cette thèse.

Les réseaux de nanodisques distribué aléatoirement et périodiquement présentent les résonances plasmoniques attendues et leurs positions ont pu été reproduites avec les simulations. Des changements de signe dans les spectres de l'ellipticité et du MCD ont été observés près des résonances plasmonique. Les mesures et simulations des spectres magnéto-optique on mis en avant les différents liens entre les valeurs et observable d'intérêt. En particulier, le lien entre les MCD et l'ellipticité transmise et réfléchie a été confirmé, de plus les différences de comportement spectral proche des résonance entre l'IFE et la rotation induite par effet Faraday ont été illustré. Les expériences d'AO-HDS ont démontré un retournement partiel de l'aimantation au-dessus d'un seuil de fluence. Pour les réseaux périodiques, aucun changement de signe n'a été observé dans le spectre d'AO-HDS, probablement dû à la détérioration de l'impact des résonances de réseau de surface sur les effets magneto-optique après la désaimantation partiel induite par les premières impulsions laser. En revanche, les nanodisques distribués de manière aléatoire ont présentés une inversion de signe dans leur spectre d'AO-HDS, ce qui correspondrait à une contribution dominante du MCD. Cependant, un décalage spectral de ce passage à zéro par rapport au spectre du MCD mesuré suggère une contribution supplémentaire de l'IFE. Les contributions relative du MCD et de l'IFE peuvent être évaluées en prenant une combinaison linaire des spectres mesurés du MCD et de l'absorption comme illustré dans la figure ci-dessous.

Le retournement partiel de l'aimantation semble indiqué le rôle important des mouvements de paroi de domaine magnétique pour obtenir un retournement complet. De manière inattendue, une différence entre les seuils de fluence de désaimantation induite par les polarisations linéaire et circulaire a été observée. Ceci peut s'expliquer par la formation de points chauds dans les nanodisques qui dépendent sur le mode de propagation de la lumière. Les résultats en lien avec les structure magnéto-plasmoniques sont détaillés dans le cinquième chapitre de ce manuscrit.

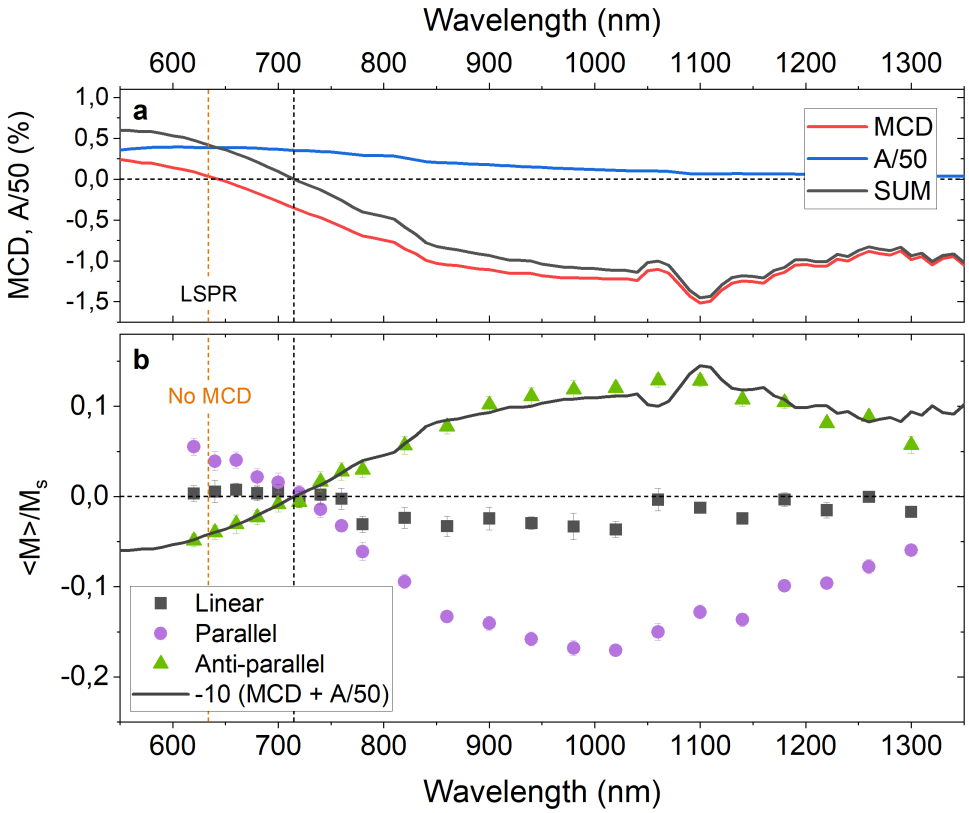

Compilation de résultats pour des nanodisques de 10 répétitions de Co/Pt ($[Co/Pt]_{10}$) et de diamètre $D = 170$ nm distribués aléatoirement. (a) Mesure des spectre du MCD et de l'absorption. (b) Spectre du retournement tout optique hélicité dépendant de l'aimantation. Les courbes gris foncé dans (a) et (b) correspond à une combinaison linéaire des spectres de MCD et d'absorption (IFE). La ligne verticale pointillé orange correspond à la longueur d'onde où le MCD change de signe. La ligne verticale pointillé noir correspond à la longueur d'onde où la combinaison linéaire des spectres de MCD et d'absorption change de signe.

En résumé, ces travaux démontrent que le contrôle de l'aimantation dépendant de l'hélicité peut être intégré dans des structures plasmoniques simples. L'étude de ces systèmes fournit des informations précieuses sur l'interaction entre les effets optique, magnéto-optique, le MCD et l'IFE. Les résultats soulignent le potentiel de l'amplification du AO-HDS dans les systèmes plasmonique. Ceci permet l'amélioration de l'efficacité énergétique des futurs dispositifs opto-magnétiques. Ces travaux peuvent être étendus dans plusieurs directions. Des nanodisques magnéto-plasmoniques peuvent être couplé avec des dispositifs électroniques, par exemple en les fabriquant sur des croix de Hall, pour étudier la dynamique du retournement de l'aimantation induite par multiple impulsion sur une échelle de temps adapter. Une autre piste consiste à exploiter l'amplification du MCD induit par les résonance plasmonique dans des matériaux présentant du retournement tout optique hélicité indépendant de l'aimantation : un MCD suffisamment important pourrait séparer les seuils de fluence de retournement entre les directions initial opposé de l'aimantation, permettant ainsi un retournement déterministe avec une seule impulsion laser polarisée circulairement.